Doctoral Dissertation

博士論文

Crystallization and evaporation experiments of type B CAI melt:
Estimate for disk gas pressure in the early Solar System

（隕石中難揮発性包有物の蒸発・結晶化実験による初期太陽系円盤
圧力の推定）

A Dissertation Submitted for the Degree of Doctor of Philosophy

December 2021

令和３年１２月博士（理学）申請

Department of Earth and Planetary Science, Graduate School of Science,

The University of Tokyo

東京大学大学院理学系研究科地球惑星科学専攻

Michiru Kamibayashi

上林　海ちる

Contents

Abstract

Protoplanetary disks formed around young stars are the places where planet formation occurs. The protoplanetary disks form as a natural consequence of star formation, and their properties such as size, mass, density distribution, thermal structure, dynamics, lifetime, and chemistry affect the characteristics of planets formed in the disks. Recent astronomical observations have demonstrated that protoplanetary disks have a wide variety of physical and chemical characteristics. The important properties of the disk include disk mass and density distributions, but they have not been observationally well constrained.

Solar System planets also formed in the Sun's protoplanetary disk (the protosolar disk) 4.6 billion years ago. The characteristics of protosolar disk should have reflected initial conditions of the Solar System and affected planets formed later within the disk. The evolution of the protosolar disk is recorded in primitive extraterrestrial materials such as chondrites and returned asteroidal and cometary samples, but the gas pressure of the protosolar disk that is related to the disk density distribution has not yet been constrained.

This thesis focused on the formation condition of calcium-aluminum-rich inclusions (CAIs), which are the oldest materials in the Solar System, to constrain the hydrogen gas pressure of the protosolar disk. CAIs consist of refractory minerals that are stable at higher temperatures than major minerals such as magnesium silicates and metallic iron. Their refractory nature suggests that CAIs formed in the high temperature region of the protosolar disk, i.e., the inner region of the disk. The isotopic evidence of CAIs (^{10}Be and oxygen isotopes) also suggests CAI formation in the innermost region of the gas disk. Therefore, CAIs should record the gaseous environment during their formation. Among various types of CAIs, type B CAIs are mostly igneous and

experienced melting and subsequent crystallization in the disk. There are two textural types of type B CAIs; one is type B1 CAIs with melilite mantle, and the other is type B2 CAIs without melilite mantle.

It has been suggested that evaporation of Mg and Si, less refractory than Ca and Al, from the melt would have played a significant role in the variation of chemical, mineralogical, and petrologic characteristics of the igneous CAIs. Evaporation rates of elements depend on hydrogen pressure (P_{H2}) and are enhanced at higher P_{H2}. When evaporation rates are high, elemental diffusion within the melt may not be able to homogenize the melt because of continuous escape of Mg and Si from the melt surface, and Al-rich melilite may crystallize from the surface enriched in Ca and Al. On the other hand, at lower P_{H2}, evaporative elemental fractionation at the surface may be homogenized within the melt owing to slow evaporation relative to diffusion, which may result in production of type B2-like texture. Therefore, the variation of igneous texture of CAIs may record the hydrogen pressure during the CAI formation.

In this study, in order to test the above hypothesis and to obtain a quantitative constraint on P_{H2} for the CAI formation, open-system crystallization experiments of CAI analog melt under disk-like low-pressure hydrogen (P_{H2}) conditions of 10^{-6}, 10^{-5}, and 10^{-4} bar with different cooling conditions appropriate for igneous CAI formation (5, 20, and 50°C h^{-1}) were conducted. The results demonstrated that at $P_{H2} = 10^{-4}$ bar, the samples were mantled by melilite crystals ($Ca_2Al_2SiO_7$-$Ca_2MgSi_2O_7$), which is similar to the texture observed in type B1 CAIs. On the other hand, the samples heated at $P_{H2} = 10^{-6}$ bar exhibited random distribution of melilite, as in type B2 CAIs. At the intermediate P_{H2} of 10^{-5} bar, type B1-like texture formed when the cooling rate was 5°C h^{-1}, whereas the formation of type B2-like texture required a cooling rate faster than 20°C h^{-1}. In the samples with melilite mantle, the compositional distribution of melilite is Mg-poor at the sample rim and becomes Mg-rich toward the inside, suggesting that these melilites crystallized inward from the melt droplet surface, as inferred from

petrological studies of type B1 CAIs. Such Mg-poor melilite at the rim has melilite composition as low as $\sim\text{Åk}_{10}$ (10 mol% of $Ca_2MgSi_2O_7$), which is more depleted in Mg than that expected for the melt of starting composition to crystallize. Such Mg-poor melilite can only crystallize from a melt which has lower Mg and Si concentrations. The compositional zoning within the melt was also confirmed in the sample heated at $P_{H2} = 10^{-4}$ bar and 1420°C for a short duration (1 h), where MgO composition decreased towards the melt surface, which is in line with the formation of melilite mantle. The three-dimensional diffusion modeling with surface evaporation for the obtained compositional zoning provided the evaporation and diffusion rates of MgO, which are consistent with those obtained in the present study and in previous studies. The results also determined that samples with a well-developed melilite mantle show elevated $\delta^{25}Mg$ values at the sample rim compared to the interior. This can also be attributed to diffusion-limited evaporation of Mg from the melt surface, where preferential evaporation of a lighter isotope (^{24}Mg) results in enrichment of a heavier isotope (^{25}Mg).

This study demonstrated that the hydrogen pressure during type B CAI formation would have been in the range of 10^{-4}–10^{-6} bar. CAI precursors might have existed in the high temperature region of the protosolar disk (>1300 K), where magnesium silicates and metallic iron were not present. The presence of ^{10}Be and mineralogically controlled O isotope composition suggest the CAI formation close to the Sun (~0.1 au). If this was the case, the disk with low mass accretion rate ($\sim10^{-8}$ $M_\odot$ yr^{-1}) or the disk evolved for >1 Myr satisfies the T-P_{H2} condition for CAI formation. If CAIs formed at ~1 au, which was recently proposed based on new interpretation of V isotopes in CAIs, the 1 au region of the disk with higher mass accretion rate ($\sim10^{-6}$–10^{-7} $M_\odot$ yr^{-1}) or the young disk (<1 Myr from the core collapse) satisfies the T-P_{H2} condition for CAI formation. While further constraints on the CAI forming location from natural samples are required, the present study puts a new quantitative constraint on the hydrogen gas pressure of the inner protosolar disk.

1. Introduction

1.1 Formation of the Solar System

Solar system planets are considered to be assembled in a disk of gas and solid particles that rotates around young Sun, analogous to what we observe today for the extrasolar planetary systems. A protoplanetary disk is a natural consequence of collapsing molecular cloud materials, consisted primarily of molecular hydrogen and helium (~99% by mass), that have excess angular momentum to fall directly onto the young star. Planets form in protoplanetary disks, and the understanding of formation and evolution of protoplanetary disks is important to elucidate the initial conditions of formation of a variety of exoplanetary systems (e.g., Armitage and Kley, 2019).

Astronomical observation of protoplanetary disks has been conducted to characterize protoplanetary disks around various young stars, and has shown wide varieties in disk properties such as mass, size, dynamics, lifetime, and molecular chemistry (e.g., Wyatt, 2008; Pascucci and Tachibana, 2010; Sakai et al., 2013; Henning and Semenov, 2013; Andrews 2020) (Fig. 1.1). It is therefore difficult to decide which would be most analogous to, if any, the Sun's protoplanetary disk (protosolar disk). Physicochemical properties and evolution of the disk determine where planets form, how they grow, and what they are made of, but they have not yet tightly constrained for the protosolar disk. Among such key factors in determining how Solar System evolved are the mass and density distribution of the gas disk, mainly consisting of molecular hydrogen, because they control disk dynamics, evolutional stage, and planetary formation. There have been astronomical observations attempting to determine the mass and density of the disk gas through observations of HD and CO (e.g., Bergin et al., 2013), and the observations have shown that there are variations of disk mass around young stars although there are many ambiguities in mass determination (Andrews, 2020).
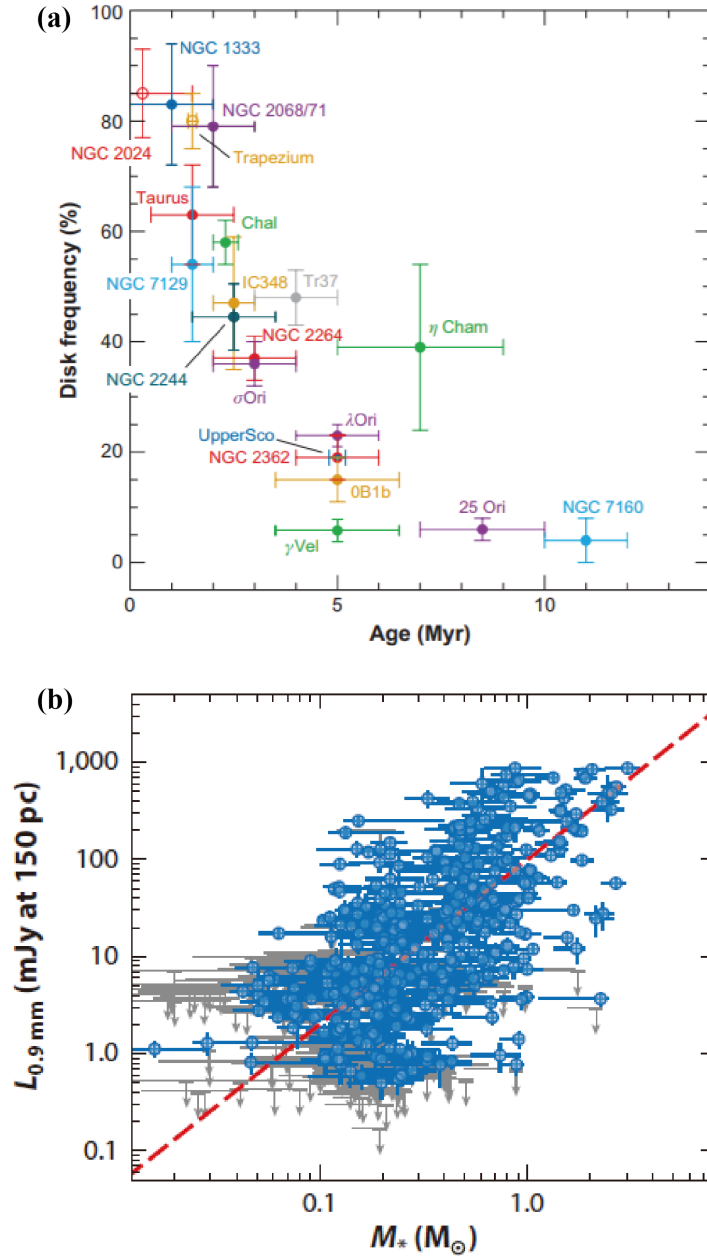
Fig. 1.1. (a) Evolution of dust disk frequency around sun-like young stars in clusters (Wyatt, 2008). The presence of disks was recognized from near-infrared excess. Protoplanetary disk has a range of lifetimes. (b) The 0.9 mm continuum emission (corrected as the emission at 150 pc) from protoplanetary dust disk young stellar objects (Andrews, 2020). There is a rough correlation between the dust emission and the stellar mass, but roughly two or more orders of variation in the disk mass is also seen for a certain mass of star. For instance, for 1 solar mass stars, three orders of magnitude variation is seen in the dust emission (i.e., dust mass).

There is no way to observe the protosolar disk, but primitive extraterrestrial materials such as meteorites and returned asteroidal and cometary samples provide information on the evolution of the early Solar System. Such information from Solar System materials, combined with studies of the evolution of protoplanetary disks developed through astronomical observations, will help us to understand the formation of planets.

Amongst constituents of primitive extraterrestrial materials, Ca-, Al-rich inclusions and chondrules, which are the components of primitive meteorites, are especially valuable for understanding high-temperature events occurred in the early Solar System such as condensation and evaporation, because they preserve chemical, isotopic, and textural evidences of these processes. The presence of these materials requires achievement of very high temperature in the solar nebula. Such high temperatures may have been achieved in the inner part of the disk with infall and/or accretion, owing to the release of gravitational potential energy from the molecular cloud and viscous heating within the turbulent disk (e.g., Boss 1998, Yang and Ciesla 2012). Solid particles that formed in the inner part of the disk can be carried outward by the radial expansion and random motions associated with disk evolution (e.g., Ciesla, 2007; Yang and Ciesla, 2012; Pignatale et al., 2018). This transport would be most rapid and efficient in the earliest epoch of the disk evolution (the first few hundred thousand years) (Nittler and Ciesla, 2016). Alternatively, local heating events such as lightning or a nebular shock may have been responsible (e.g., Richter et al., 2006). In either case, CAIs and chondrules were formed by high temperature events in the inner region of the protosolar disk at the very early stage of the Solar System evolution, and were incorporated into parent planetesimals of primitive extraterrestrial materials.

The thermal histories of CAI and chondrule forming events have been well constrained through laboratory studies to reproduce their igneous textures (e.g., Stolper, 1982; Stolper and Paque, 1986; Jones et al., 2018 and references therein). Because

chemical and isotopic characteristics of CAIs and chondrules indicate their formation in the presence of disk gas (Pascucci and Tachibana, 2010), these high temperature components should record the gaseous environment of the inner protosolar disk. However, contrary to the well constrained thermal history, the gas pressure conditions in the inner disk during the epoch of such high temperature events, have not yet been understood. It is essentially important to constrain the disk gas pressure in the early Solar System, which may lead to further constraints on physical properties of the protosolar disk, timing and location of CAI formation in the protosolar disk, and planetary formation occurring in the disk after CAI formation. In this thesis work, I focus on CAIs, which will be described in detail below, to constrain the inner disk gas pressure in the very early evolutional stage of the Solar System.

1.2 Calcium-aluminum-rich inclusions

Ca-Al-rich inclusions (CAIs) are the assemblage of high temperature minerals which hold information on the origin and evolution of the Solar System. They consist of minerals that are predicted to be the first phases to condense out of a cooling gas of solar composition (e.g., Grossman, 1972; Fig. 1.2). The CAIs that formed as direct condensates are called fine-grained CAIs, while coarse-grained CAIs are considered to have thermally reprocessed. Based on mineralogical features, coarse-grained CAIs have been classified into three main types; type A composed mainly of melilite, type B containing melilite, spinel, pyroxenxe, and anorthite, and anorthite-rich type C (e.g., MacPherson, 2014 and references therein). Some of these, especially type B CAIs, went through reheating processes after their condensation from gas, presenting igneous textures that are indicative of crystallization from a melt (MacPherson and Grossman, 1981; Stolper, 1982; Stolper and Paque, 1986).

Radiometric dating provides absolute and relative ages of CAIs, indicating that they are the oldest materials in the Solar System (4567.30 ± 0.16 Ma) (Amelin et al. 2010; Connelly et al., 2012). Al-Mg dating of the CAIs suggests that the thermal processing of igneous CAIs is considered to have begun shortly after the first condensation of the solid materials. Al-Mg dating indicate that condensation and reprocessing of the CAIs continued over at least 0.4 Myrs at the very beginning of the Solar System (MacPherson, 2014 and references therein; Kawasaki et al., 2020). Although CAIs have been used to define the age of the Solar System because of their oldest age among the Solar System materials, it is not clear which evolutional stage the protosolar disk was in when CAIs formed (Fig. 1.3).
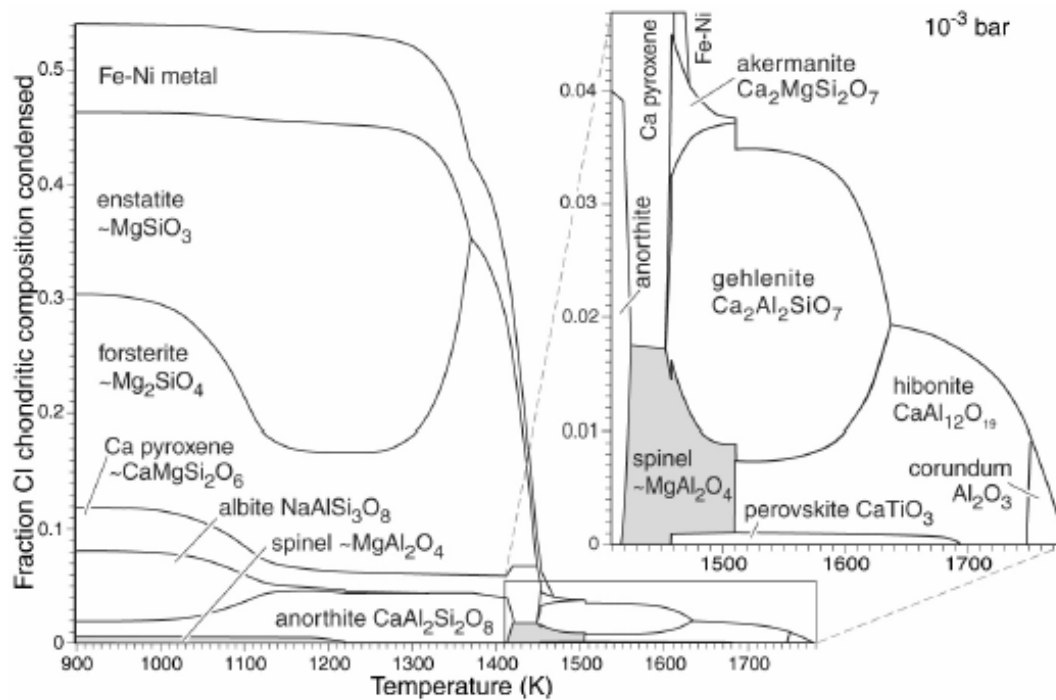
Fig. 1.2. Equilibrium diagram illustrating the minerals that are stable above 900 K in a nebula of solar composition at 10^{-3} bar. CAI constituent minerals matches the first 5% of the condensed phases. The figure taken from Scott and Krot (2005).
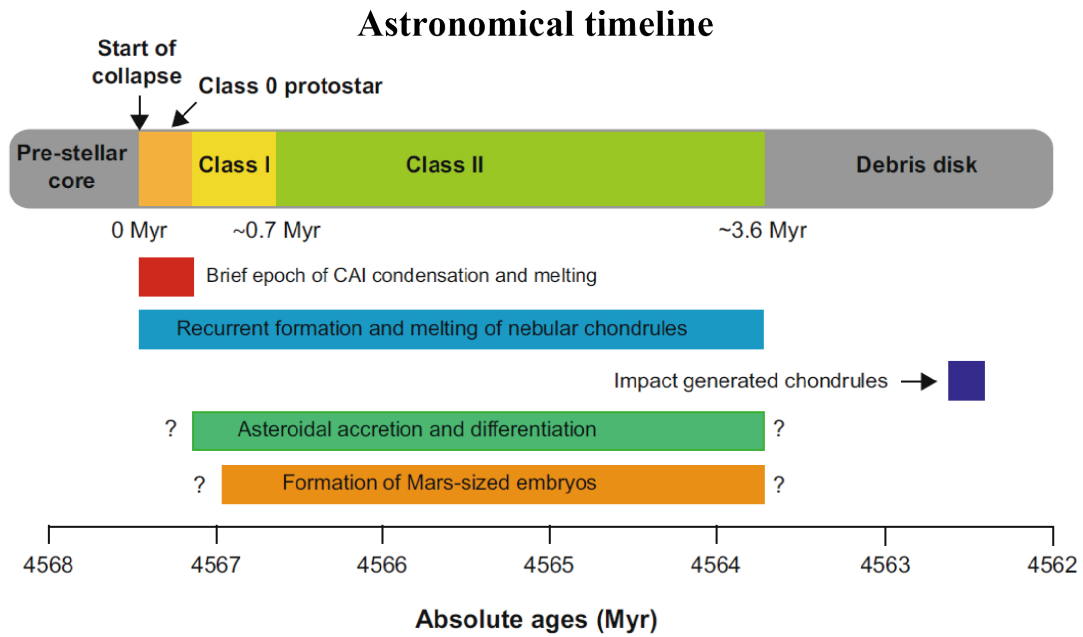
Fig. 1.3. The comparison between the timelines which are define by the evolutional stage of the protosolar disk (astronomical timeline), and by the formation age of Solar System materials (extraterrestrial sample timeline). In this figure, t = 0 is not necessarily the same in both timelines and the relationship between these timelines remains unclear. The figure taken from Bizzarro et al. (2017).

The presence of short-lived nuclide, [10]Be, provides information on the location where the CAIs formed. McKeegan et al. (2000) and MacPherson et al. (2003) argued that [10]Be was produced though energetic solar cosmic rays near the protosun (~0.1 au). The CAI formation near the inner edge of the protosolar disk has also been suggested to explain mineralogically controlled O isotope variations within igneous CAIs (Itoh and Yurimoto, 2003; Yurimoto et al, 2008; Kawasaki et al., 2018). Recently, this idea was challenged by Bekaert et al. (2021) who claimed that vanadium isotope composition of CAIs, which have been proposed as the evidence of particle irradiation, can be explained by kinetic isotopic fractionation owing to evaporation. Bekaert et al. (2021) concluded that CAIs could have formed at greater heliocentric distances than previously

considered, up to ~1 au (Bekaert et al., 2021).

The formation condition of CAIs has been discussed intensively for igneous type B CAIs. Type B CAIs are typically millimeter- to centimeter-sized, coarse-grained inclusions, mostly found in CV chondrites. The thermal history of type B CAIs was constrained from experimental studies. Stolper (1982) and Stolper and Paque (1986) conducted equilibrium and dynamic crystallization experiments of melt with average type B CAI composition and concluded that the precursor materials were rapidly reheated to ~1400°C (slightly above the liquidus temperature of melilite) and then cooled at rates of 0.5–50°C h^{-1} to produce the chemical and textural characteristics of coarse-grained igneous textures. To maintain observed minor-element abundances in spinels, the heating duration at the maximum temperature should have been less than a few tens of hours (Connolly and Burnett, 2003). The suggested crystallization sequence from the type B CAI melts is spinel followed by melilite (~1400°C), then anorthite or pyroxene (<1250°C). Melilite is a binary solid solution of gehlenite (Ca$_2$Al$_2$SiO$_7$) and åkermanite (Ca$_2$MgSi$_2$O$_7$) and ranges in composition from ~ Åk$_{10}$ to Åk$_{72}$ in type B CAIs (MacPherson, 2014 and references therein). The composition of melilite crystallizing from a melt is a strong function of temperature, and in the range of melilite in type B CAIs, the first-formed melilite at the highest temperature is relatively Al-rich and becomes progressively Mg-rich with decreasing temperatures.

Type B CAIs are texturally subdivided into type B1s and type B2s (Wark and Lovering, 1982). Type B1s have continuous outer layer of melilite enclosing interior part consisting of random distribution of the constituent minerals (Fig.1.4). Such mantle melilite is absent from type B2s and the entire inclusion resembles the interior part of type B1s. Wark and Lovering (1982) suggested that the inward crystallization of melilite from the CAI surface yielded continuous melilite mantle in type B1s. Simon and Grossman (2006) attributed the difference in texture of type B1 and B2 to their precursor compositions which result in different amount of melilite crystallized.

However, it is not clear whether types B1 and B2 have different bulk compositions. Mendybaev et al. (2006) conducted crystallization experiment of CAI analog melt at 1 atm of hydrogen dominant gas and showed that the presence or absence of melilite mantle is determined by the relative rate of evaporation from the melt surface and diffusion in the melt. This proposed mechanism, which will be discussed in section 1.4, has not yet tested in realistic low-pressure conditions.
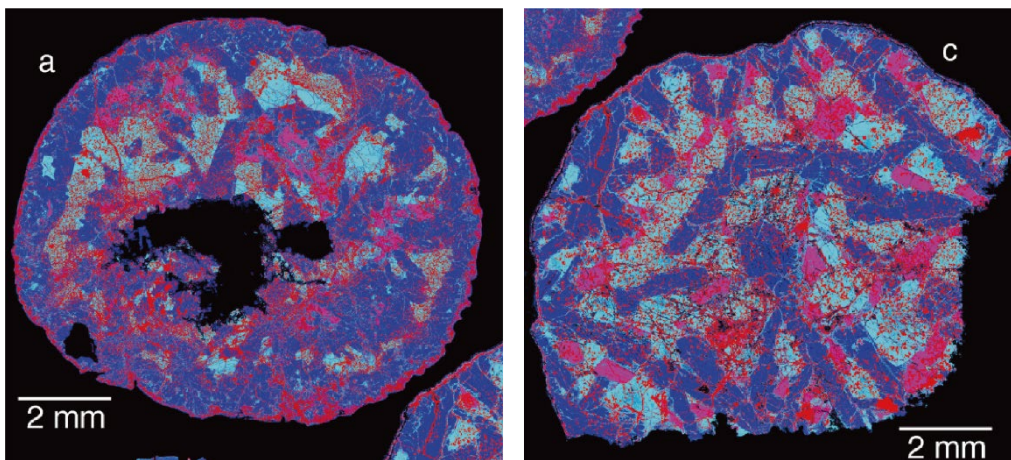
Fig. 1.4. Combined X-ray elemental maps of Allende type B1 CAI TS23 (left) and Allende type B2 CAI TS33 (right). The major phases are melilite (dark blue), fassaite (light blue), anorthite (pink), and spinel (red). Type B1 CAI demonstrates a well-developed mantle of melilite crystals, while type B2 displays a relatively random distribution of melilite. Figure modified from Richter et al. (2006).

1.3 Effect of evaporation on igneous CAIs

There is a good chemical and isotopic evidence supporting the idea that coarse-grained type B CAIs are residues that experienced evaporation from the molten state in the gaseous protosolar disk. Type B CAIs are often found to have correlated enrichments in the heavy isotopes of Mg and Si, which are volatile relative to Ca and Al (Fig. 1.5) (Clayton et al., 1988). Such isotopic fractionations are experimentally confirmed in melt evaporation under vacuum or in hydrogen gas (e.g., Davis et al., 1990; Richter et al., 2002; Richter et al., 2007; Mendybaev et al., 2021). Grossman et al. (2000) demonstrated that these isotopic fractionations are in good agreement with the amount of chemical fractionation of Mg and Si produced by non-equilibrium evaporation of equilibrium condensates.
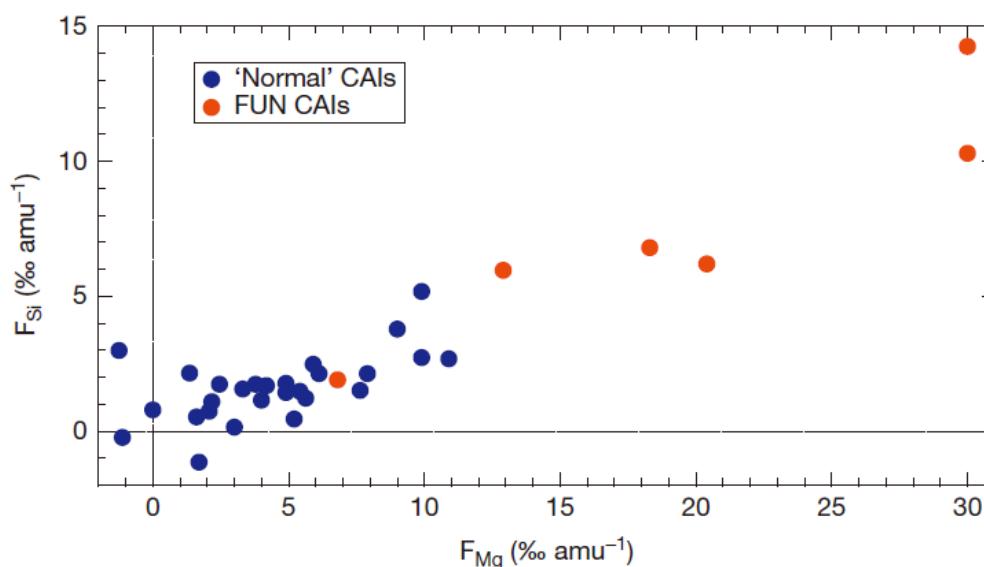
Fig. 1.5. Isotopic mass fractionation of Mg and Si observed in CAIs relative to Solar System composition. Figure taken from Davis and Richter (2014).

Evaporation of minerals and silicate melts in vacuum and in low-pressure hydrogen gas has been investigated experimentally to determine evaporation rates and their dependence on hydrogen pressure and to understand the mechanism of kinetic evaporation and/or isotopic fractionation owing to evaporation (Hashimoto, 1983, 1990;

Davis et al., 1990; Nagahara and Ozawa, 1996; Tsuchiyama et al., 1998; Tachibana and Tsuchiyama, 1998; Wang et al., 2001; Richter et al., 2002; Tachibana et al., 2002, 2011, Kuroda and Hashimoto, 2002, Yamada et al., 2006; Takigawa et al., 2009, 2015; Mendybaev et al., 2021). These previous works showed that evaporation of silicate minerals and melts depends on hydrogen gas pressure (P_{H2}) and are enhanced in the presence of hydrogen gas because it works as a reducing agent for silicates and oxides.

In the case of silicates melts, including CAI melts, evaporation of Mg and Si in hydrogen-rich gas is expected to occur via reactions:

$$MgO~(l) + H_2~(g) \rightarrow Mg~(g) + H_2O~(g) \qquad (Eq.~1.1a)$$

$$SiO_2~(l) + H_2~(g) \rightarrow SiO~(g) + H_2O~(g) \qquad (Eq.~1.1b)$$
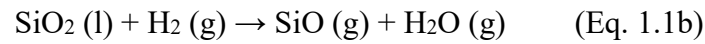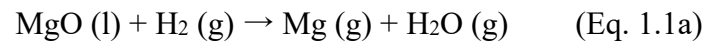
Equilibrium thermodynamic calculations (Grossman et al., 2000; Ebel and Grossman, 2000) and Knudsen effusion mass spectrometry (e.g., Shornikov and Yakovlev, 2015) have shown that the dominant gas species for evaporation of Mg and Si are Mg and SiO, respectively. It is confirmed that evaporation of Mg and Si from CAI analog melt is promoted in the presence of hydrogen gas, the most abundant gas in the protosolar disk (e.g., Richter et al., 2002). I have also confirmed this enhancement by conducting evaporation experiments of CAI-analog melt at 1600°C under disk-like low pressure-hydrogen (Mendybaev et al., 2021) (Fig. 1.6).
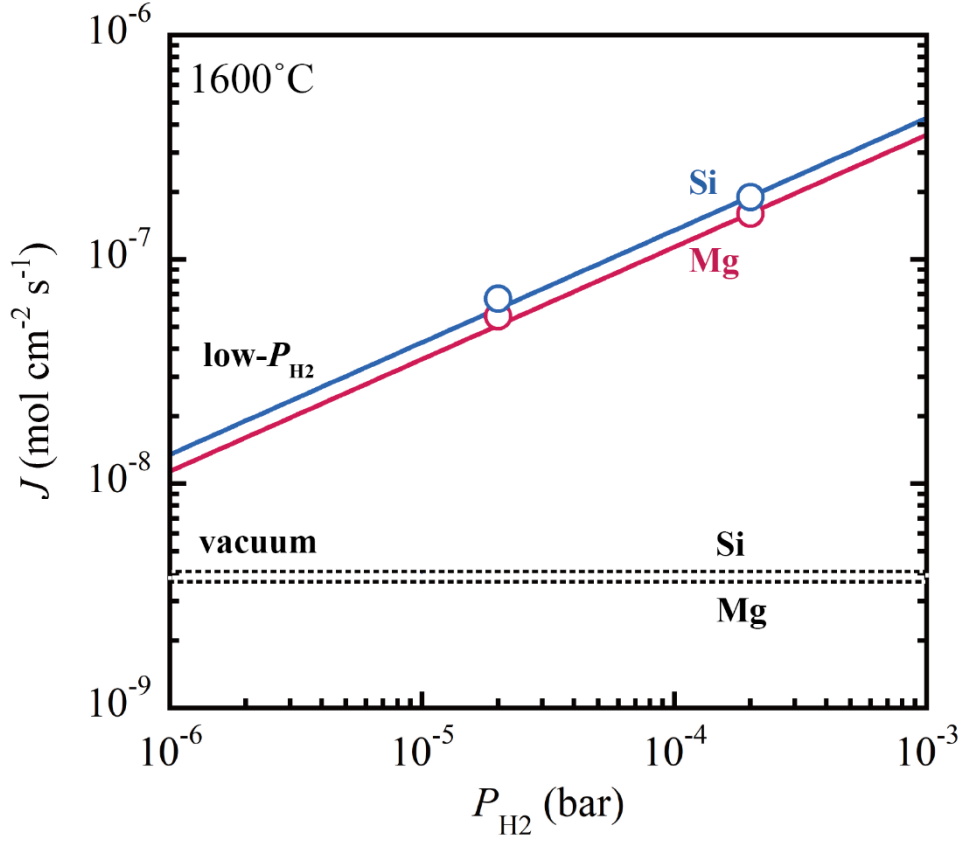
Fig. 1.6. Average evaporation rates of Mg and Si from CAI analog melts in vacuum (dotted lines) and low-P_{H2} (solid lines) at 1600°C. Evaporation rates of Mg and Si at $P_{H2} = 2 \times 10^{-4}$ bar and 2×10^{-5} bar are ~45 and ~19 times faster than those in vacuum at this temperature. Evaporation rates at $P_{H2} = 2 \times 10^{-4}$ and 2×10^{-5} bar are explained by the P_{H2} dependence of $\sqrt{P_{H2}}$. Data are from Mendybaev et al. (2021).

The kinetics of evaporation from a molten surface into a surrounding gas is given by the Hertz-Knudsen equation (e.g., Hirth and Pound, 1963):

$$J_i = \frac{\gamma_i P_{i,sat}}{\sqrt{2\pi m_i RT}}$$

where J_i is the flux of i, γ_i is the evaporation coefficient, $P_{i,\,sat}$ is the saturation vapor pressure of i, m_i is the molecular weight of i, R is the gas constant, and T is the absolute temperature. This representation originates in the kinetic theory of ideal gases where $P_i / \sqrt{2\pi m_i RT}$ is the rate of collision with the surface of the species containing i. Except for γ_i, the various quantities on the right-hand side of equation can be calculated given a suitable thermodynamic model for the condensed phases and for the composition and speciation in the surrounding gas. For each of the reaction expressed in Eq. 1.1.a and 1.1.b, an equilibrium constant K_i can be calculated using thermodynamic database. The activity of each oxide can be calculated by thermodynamic model of Berman (1983) for a CaO-MgO-Al_2O_3-SiO_2 liquid of any composition. Then, saturation vapor pressure of evaporating species can be calculated as a function of P_{H2}, and is proportional to the square root of P_{H2}. Thus the evaporation rates of Si and Mg are proportional to the saturation vapor pressure of SiO and Mg respectively, which increases linearly with the square root of P_{H2}. Such a hydrogen pressure dependence of evaporation rate was confirmed by Takigawa et al. (2009) for crystalline forsterite.

I note here that the saturation vapor pressure of Al and Ca gas species are lower than those of Mg and Si more than five orders of magnitude, thus aluminum and calcium do not evaporate to any significant degree under conditions of the present experiments.

1.4 Concepts and aims of the thesis

Since the evaporation rates of Mg and Si as a function of equilibrium vapor pressure of Mg and SiO is expected to change linearly with a square root of P_{H2}, if igneous type B CAIs had experienced evaporation during their formation, they may have recorded the gaseous environment of the protosolar disk.

In this thesis I focus on constraining the hydrogen pressure of the CAI forming region by considering competition of evaporation from CAI melts and elemental diffusion and crystallization within the melts (Fig. 1.7). While evaporation depends on P_{H2}, elemental diffusion and crystallization within the melt are not dependent on the ambient P_{H2}. The compositional homogeneity/heterogeneity within the melt is controlled by the relative dominance of elemental diffusion and evaporation from the surface (Fig. 1.7). Mendybaev et al. (2006) suggested that if the evaporation of Mg and Si dominates their diffusion within the melt, which would occur in a relatively high P_{H2} condition, the preferential crystallization of melilite would arise at the melt surface enriched with Ca and Al. On the other hand, if the diffusion dominates over evaporation, melilite crystallization occurs randomly within the melt, resulting in type B2-like texture. In this sense, textural characteristic of type B CAI would be an indicator of the hydrogen partial pressure of the protosolar disk (Fig. 1.7). However, this prediction has not yet been tested experimentally under low hydrogen pressure conditions. Because kinetics and relevant elementary processes may change at different conditions, it is necessary to confirm the prediction based on experiments at 1 atm under low-pressure hydrogen conditions close to the protosolar disk for quantitative discussion/constraints of P_{H2} for the type B CAI formation.

low-P_H

high-P_{H2}
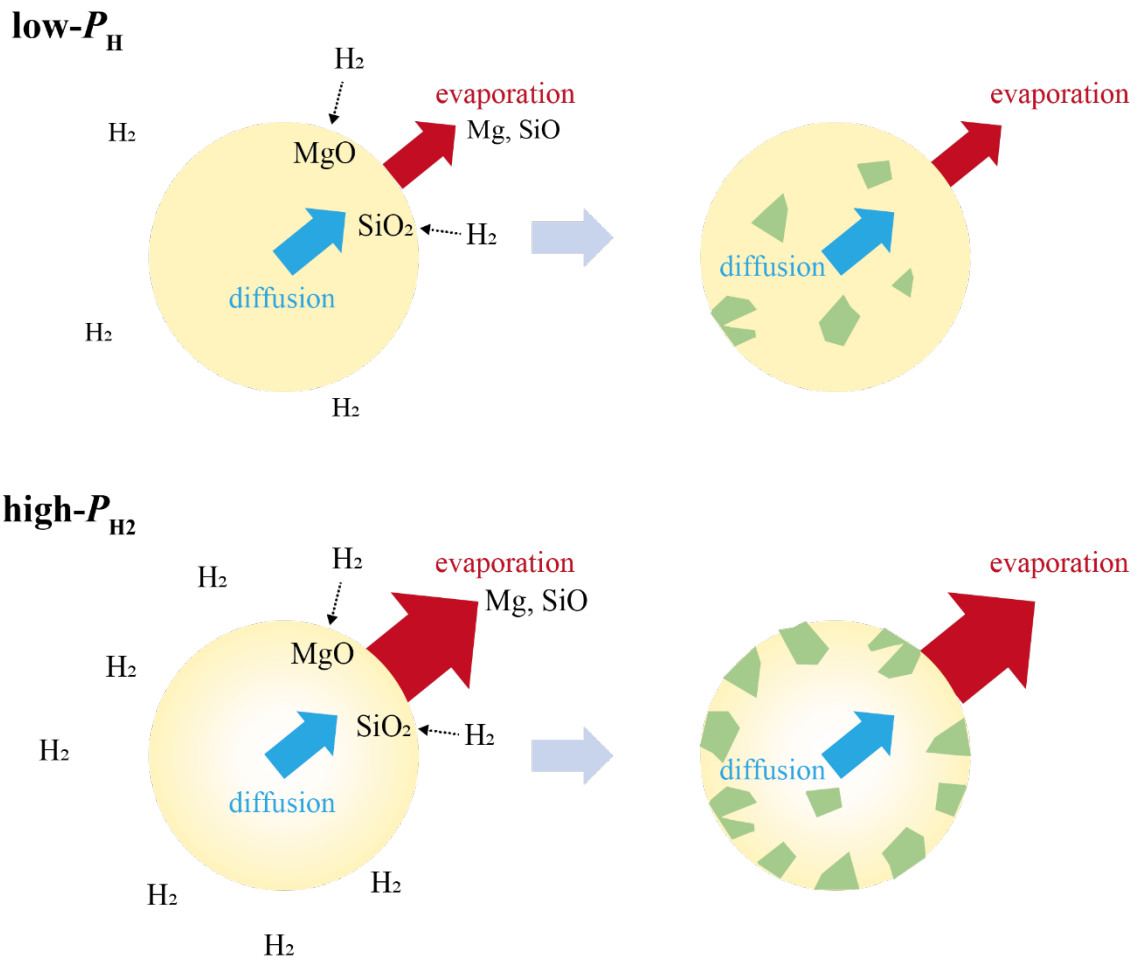
Fig. 1.7. Conceptual images of the formation of different melilite texture in different P_{H2} conditions.

Igneous type B CAIs experienced melting of precursor materials and may thus have been less primitive than fine-grained or fluffy type A CAIs that are most likely to be condensates from high temperature disk gas. However, it has been known that the formation of CAIs, including the formation of type Bs that went through melting, took place in a brief epoch of the earliest Solar System (~0.4 Myr; e.g., MacPherson, 2014 and references therein; Kawasaki et al., 2020). Therefore it is reasonable to consider the hydrogen pressure at the formation of type B CAIs to constrain the disk gas pressure in the early Solar System. I also emphasize here that the hydrogen pressure can be constrained only through evaluation of competing reactions with different P_{H2}

dependence (evaporation, diffusion, and crystallization) that formed type B CAIs. It is difficult to estimate P_{H2} quantitatively, based on our current understanding, from unmelted CAIs that could be condensates because it would be indistinguishable between rapid condensation from high P_{H2} gas and slow condensation from low P_{H2} gas.

Quantitative constraint on the hydrogen pressure of the protosolar disk at the formation of CAIs is important as it is directly related to the density of the disk gas in the very early stage of Solar System evolution. The gas density can be combined with a theoretical disk model to give critical parameters in considering more realistic evolution model of protosolar disk (e.g., mass accretion rate and angular momentum transport coefficient). Because the formation ages of CAIs are relatively limited to the brief interval compared to that of other extraterrestrial samples (e.g., MacPherson, 2014 and references therein; Kawasaki et al., 2020), such important constraints in turn would enable us to link the astronomical timeline and the extraterrestrial sample timeline (Fig. 1.3).

In this thesis, I aim at constraining the disk gas pressure in the high temperature inner region of the protosolar disk, where the oldest Solar System objects formed. I focus on the effect of evaporation during crystallization of type B CAIs on chemical and textural variations, which are governed by competition of evaporation, dependent on P_{H2}, and diffusion and crystallization, independent on P_{H2}. Because of the complex nature of reactions within the melt, a series of crystallization experiments with CAI analog melt in an open system in the presence of protosolar disk-like low-pressure hydrogen gas was conducted. The results will be discussed to put a constrain on the physicochemical condition, especially a poorly constrained parameter P_{H2}, at the formation region of type B CAIs.

2. Experimental methods

2.1 Preparation of starting materials

The starting materials used in the experiments are compositions close to the composition χ and δ (hereafter referred as CAIχ and CAIδ; Table 2.1) plotted along the trajectory of equilibrium condensation from a gas of solar composition at the total pressure of 10^{-5} bar (Grossman et al., 2002) (Fig. 2.1). Appropriate amount of evaporation of Mg and Si (< 30% for Mg and < 20 % for Si; Grossman et al., 2002) from these compositions result in the compositions that fall in the field of the bulk composition of most type B CAIs, and thus CAIχ and CAIδ are their possible precursor compositions (Grossman et al., 2002). CAIχ and CAIδ have different liquidus temperatures of melilite, $1402.5 \pm 2.5°C$ and $1312.5 \pm 2.5°C$, respectively (see section 3.1.1) and their effect on crystallization in an open system will be discussed later. The starting materials were prepared by mixing SiO_2, TiO_2, Al_2O_3, MgO, and $CaCO_3$ reagent powders aiming at each composition. These powders were ground under ethanol in an alumina mortar for ~1 h, dried at room temperature, and slowly heated to 1000°C for 10 h in a muffle furnace in a platinum crucible to drive off CO_2 from $CaCO_3$. The platinum crucible was then heated in a 1 atm Keramax vertical tube furnace (Nikkato Corporation TS-4B06) to 1525°C for 24 h and quenched in air. Resulting glass + spinel assemblage was then ground into powder in an alumina mortar and used as starting material for experiments in air and under low-pressure hydrogen.

Table 2.1. Chemical composition of the starting materials used in the experiments

	Composition (Wt. %)				
	SiO_2	TiO_2	Al_2O_3	MgO	CaO
CAIχ	25.71	1.11	33.23	13.64	26.23
CAIδ	29.45	1.12	30.44	14.90	24.10
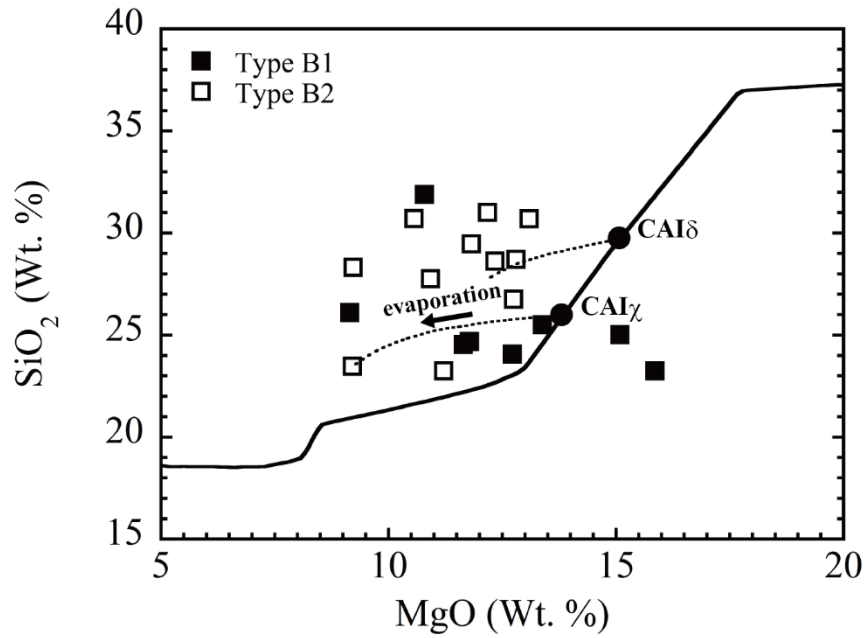
Fig. 2.1. Bulk chemical compositions of type B inclusions compared with the calculated composition path of equilibrium high-temperature condensates from a solar gas at $P_{tot.} = 10^{-5}$ bar (solid curve) (Grossman, 2002). Compositions of condensate assemblages selected as starting materials listed in Table 2.1 are indicated. Dotted curves are the evolutionary paths of bulk chemical compositions during evaporation of Mg and Si from the melt calculated by Grossman et al. (2002).
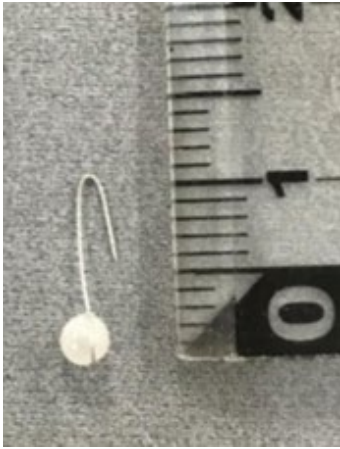
2.2 Experiments in air

Isothermal crystallization experiments were conducted in air to determine liquidus temperature of melilite for melts with initial compositions of CAIχ or CAIδ. Experimental details of isothermal crystallization experiments in air are the same as those described in Yamamoto et al. (2021). An aliquot of 0.3 g of CAIχ or CAIδ was pressed into a cylindrical pellet (3 mm in outer diameter, 3 mm thickness, and a 1 mm diameter of the inner hole) and hung above the 2.5 mm-diameter platinum wire loop through the inner hole of the pellet. Isothermal crystallization experiments were conducted at 1420–1300°C with heating duration of 5–24 h (Tables 2.2, 2.3), using the Keramax vertical tube furnace. The temperature at the hot spot of the furnace was measured and controlled by a type R (Pt-Pt13Rh) thermocouple, and calibrated using the melting points of gold (1064.4°C) and palladium (1555°C) (Yamamoto et al., 2021).

A dynamic crystallization experiment was also conducted in air for the CAIχ composition to compare the chemical and textural characteristics with those of the samples in isothermal experiments in air and dynamic crystallization experiments under low-pressure hydrogen.

2.3 Experiments under low-pressure hydrogen

Samples for experiments under low-pressure hydrogen were prepared by fixing the mixture of 20–40 mg of the starting material and polyvinyl alcohol as a binder onto 2.5 mm diameter iridium wire loop (Fig 2.2). Iridium was chosen for its high refractory nature under reducing condition (i.e., hydrogen-rich environment) (Mendybaev et al., 2006). After drying in air at room temperature, the samples were premelted with either of the following procedures: (a) heated at 1520°C for 2 h in air using the Keramax furnace or (b) heated in vacuum (<~10^{-4} bar) at 1600°C for 10 min and then 1450°C for 10 h using a high-temperature vacuum furnace described in detail below. These procedures were adopted to get rid of the voids inside the melt droplet. Conditions for premelting procedure in each experiment is shown in Tables 2.2, 2.3 along with experimental conditions. The premelted samples were 2–3 mm in size (Fig. 2.3), which are within the size range of natural type B CAIs (on the order of millimeters to centimeters in diameter) (MacPherson and Grossman, 1981; MacPherson and Davis, 1993; MacPherson, 1982; El Goresy et al., 1985; Paque et al., 2007; Shahar and Young, 2007; Simon et al., 2005; Sugiura et al., 2004; Sylvester et al., 1992; Sylvester et al., 1993; Podosek et al., 1991; Simon and Grossman, 2006; Bullock et al., 2013; Kawasaki et al., 2018).

Fig. 2.2. Starting material on a 2.5 mm diameter iridium wire loop used for low-pressure hydrogen experiments.
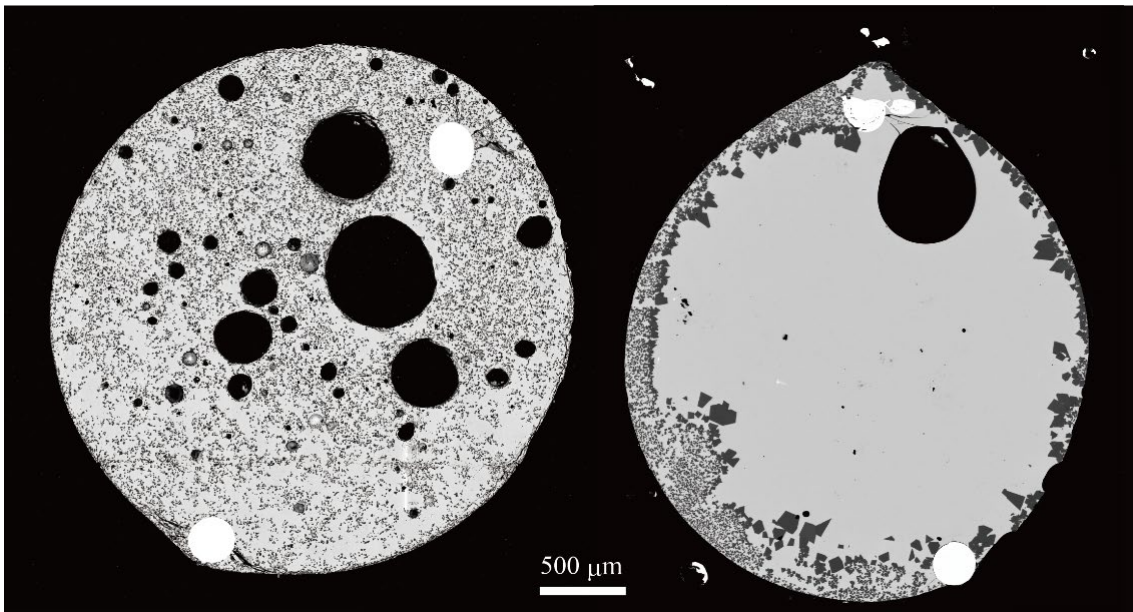
Fig. 2.3. Backscattered electron (BSE) images of the starting materials prepared by heating at 1520°C for 2 h in air (left) and at 1600°C for 10 min then 1450°C for 10 h in vacuum (right). Phases in light and dark gray are glass and spinel, respectively.

Isothermal and dynamic crystallization experiments in low-pressure hydrogen conditions were conducted at systematically-varied P_{H2} (10^{-6}, 10^{-5}, and 10^{-4} bar) at a maximum temperature of 1420°C using a high-temperature vacuum furnace. The peak

temperature experienced by type B CAIs during remelting should not be considerably higher than that in this study because it would result in crystallization of dendritic melilite even at the cooling rate as slow as 2°C h^{-1} (Stolper and Paque, 1986). Such dendritic melilite is not observed in natural CAIs. Moreover, oxygen isotopic compositions of minerals in type B CAIs show that spinel is a relict phase (Kawasaki et al., 2018; Yamamoto et al., 2021) and did not experience a large degree of melting and recrystallization. At temperatures higher than 1400°C, remelting and subsequent crystallization of spinel are expected (Stolper, 1982). The peak temperature should not be much lower than ~1400°C because of several reasons. Because oxygen isotope compositions of melilite in natural CAIs suggest that melilite crystallized through cooling from temperatures higher than its liquidus (Kawasaki et al., 2018; Yamamoto et al., 2021), precursors with the starting composition like CAIχ (melilite liquidus of 1402.5 ± 2.5°C) should be heated above ~1400°C. In the case of CAIδ (melilite liquidus of 1312.5 ± 2.5°C), the closed system crystallization results in formation of Mg-rich melilite that are not common in type B CAIs irrespective of heating temperature above melilite liquidus because of its Mg-rich bulk composition. As discussed later, the open system crystallization with evaporation of Mg and Si forms Al-rich (Mg-poor) melilite from CAIδ, and the degree of Al-enrichment in melilite depends on the evaporation temperature (section 4.1). I will show later that the peak temperature of ~1400°C is required to form Al-rich melilite for the open-system crystallization.

The cooling rates of 50, 20, 5°C h^{-1} were chosen for the dynamic crystallization experiments because type B CAIs were expected to be cooled at a rate of 0.1–50°C h^{-1} based on crystallization experiments and chemical and oxygen isotopic evidences of constituent minerals (MacPherson and Grossman, 1981; Stolper,1982; Stolper and Paque, 1986; Kawasaki et al., 2018; Yamamoto et al., 2021). The furnace used in the experiments is similar to that used for evaporation experiments of forsterite in Takigawa et al. (2009) and consist of stainless-steel vacuum chamber, a thermal

shield, a tungsten mesh heater, a molybdenum sample holder, a pumping system (a turbo-molecular pump and a rotary pump/dry pump), and gas flow system (Fig. 2.4) (Kamibayashi et al., 2021). Hydrogen gas was supplied from a hydrogen gas cylinder (99.99%) through the alumina tube and exhausted from the bottom of the vacuum chamber by the pumping system. The flow rate of hydrogen gas was adjusted by a variable leak valve or a mass flow controller (Kofloc 3660) to keep P_{H2} at 10^{-6}, 10^{-5}, 10^{-4} bar with the fluctuation of P_{H2} at typically less than ~20%. The flow rate was 8.2, 63.5, and 217 cm^3 min^{-1} at 10^{-6}, 10^{-5}, and 10^{-4} bar, respectively. Pressure inside the furnace was measured with a Pirani and an ionization gauge (ULVAC M-13). A proper pressure conversion factor for H_2 was used (the actual hydrogen pressure was converted as twice the indicated pressure) when hydrogen gas was introduced into the furnace. Temperature was monitored and controlled with a type C ($W_{95}Re_5$-$W_{74}Re_{26}$) thermocouple placed 22.5 mm above the sample location. The temperature of the thermocouple was calibrated against the melting point of Au (1064.4°C) and Ni (1455°C) by placing the metals at the sample location. The premelted sample was hung on the sample holder and evacuated to better than 5×10^{-4} bar, and preheated at 500°C for ~1 h to evacuate absorbed gas in the vacuum chamber. After the pressure in the chamber decreased below 5×10^{-4} bar, the sample was heated to the experimental temperatures at a rate of ~20°C min^{-1}. Hydrogen gas was introduced into the furnace as soon as it gets to the maximum temperature. After heating for a pre-determined period of time, the sample was cooled by turning off the heater (the temperature dropped down to the sample solidus temperature of ~1100°C (Stolper and Paque, 1986) at the rate of ~500°C min^{-1}).
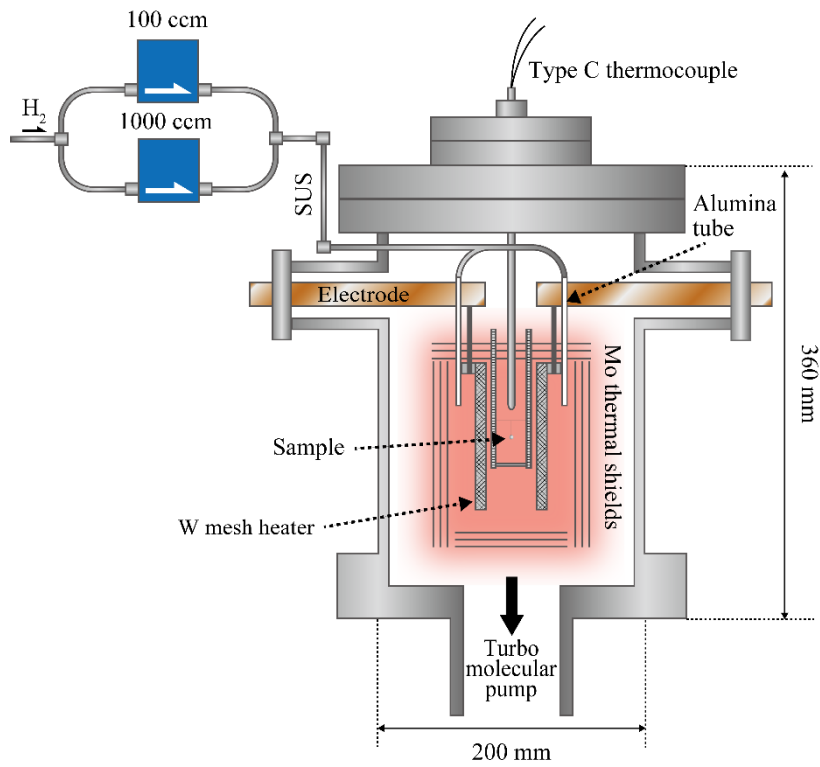
Fig. 2.4. Schematic illustration of the configuration of the high temperature vacuum furnace equipped with gas flow system.

2.4 Analytical Procedure

The weights of the samples were measured before and after experiments at low-pressure hydrogen with electric ultra-microbalances (Mettler Toledo XP2U and AND BM-20) with a precision of < 2.5 μg scale to estimate the amount of evaporation from the melt. All weight loss was attributed to sample evaporation, based on a blank experiment in which negligible amount of weight loss of iridium wire was observed (less than 0.2% of the initial sample mass). Experimental conditions and weight losses are summarized in Tables 2.2, 2.3.

The starting material and run products were mounted into epoxy, and then polished along the orthogonal plane to the wire loop by alumina polishing films and diamond paste down to the roughness of 0.5–1 μm. Textural observations and quantitative elemental analyses were conducted using scanning electron microscopes (SEM; JEOL JSM-7000F at Hokkaido University; Hitachi SU-6600 at ISAS/JAXA) equipped with an energy dispersive X-ray spectrometer (Oxford X-Max150) operated at an acceleration voltage of 15 kV. Details of the elemental analysis by JEOL JSM-7000F is described in Kawasaki et al. (2018; 2019). Bulk compositions of some samples were also evaluated by averaging the results of elemental analyses of 10–20 raster areas (~650 μm×~500 μm) covering the whole area of sample cross sections, as conducted for natural CAIs to obtain their bulk compositions (e.g., Wada et al., 2020). The built-in standardization database at 15 kV in the Oxford AZtec software was used for elemental analysis with Hitachi SU-6600. Quantitative elemental maps of Mg, Si, and Al were converted to quantitative compositional maps of melilite using the ImageJ software.

Quantitative analysis of glass was obtained using a JEOL JXA-8900L electron probe microanalyzer, operating at 15 kV and 12 nA with a beam size of ~5 μm. The profiles of the glass composition were obtained in lines passing through the center of the spherical sample at an interval of 50 μm. The radius of each spherical sample was calculated from the diameter along the compositional profile.

The Mg isotopic compositions and ^{27}Al/^{24}Mg ratios of the minerals were measured with a secondary ion mass spectrometry (SIMS; Cameca ims-1280HR) at Hokkaido University, following the procedures by Kawasaki et al. (2019). An ^{16}O$^-$ primary beam accelerated to 23 keV was employed. The Mg isotopes (^{24}Mg$^+$, ^{25}Mg$^+$, and ^{26}Mg$^+$) and ^{27}Al$^+$ were measured simultaneously in multicollection mode with four Faraday cups. The primary beam current was set to 5 nA with an elliptical shape of 10 × 15 μm for measurements of melilite, and 13 nA with an elliptical shape of 15 × 20 μm for fassaite measurements. Synthetic glasses of which chemical compositions are close to melilite and fassaite in experimental products, were used to correct the instrumental mass fractionation of Mg isotopes and relative sensitivity factors of Al and Mg (Kawasaki et al., 2021). After the SIMS analysis, the samples were observed using the SEM to check the analytical location in the samples and to measure the distances from the analytical points from the sample surface.

Table 2.2

Experimental conditions and results for isothermal and dynamic crystallization experiments in air and low-pressure hydrogen with CAIχ composition

Run	T_{max}	T_{quench}	Duration at T_{max}	Gas comp.	Cooling rate	Wt. loss		Phases identified[a]	Melilite comp.	Texture[d]	Premelting[e]
	(°C)	(°C)	(h)	(pressure in bar)	(°C h^{-1})	(%)	(mg cm^{-2})		(Åk%)		
Isothermal experiments in air											
97	1420	1420	12	air	/	/	/	gl + sp	/	/	/
106	1410	1410	12	air	/	/	/	gl + sp	/	/	/
351	1405	1405	12	air	/	/	/	gl + sp + mel	21 ± 2[b]	/	/
104	1400	1400	12	air	/	/	/	gl + sp + mel	22 ± 2[b]	/	/
81	1380	1380	12	air	/	/	/	gl + sp + mel	26 ± 2[b]	/	/
94	1360	1360	12	air	/	/	/	gl + sp + mel	32 ± 2[b]	/	/
Dynamic crystallization experiments in air											
UT-9	1420	1120	1	air	50	/	/	gl + sp + mel + px	43–62 [d]	B2-like	(b)
Dynamic crystallization experiments in low-pressure hydrogen											
191	1420	1120	1	H$_2$ (10^{-6})	50	2.1	2.9	gl + sp + mel + px	31 – 72[c]	B2-like	(a)
UT-16	1420	1120	1	H$_2$ (10^{-6})	50	0.7	0.8	gl + sp + mel + px	38 – 63[c]	B2-like	(b)
198	1420	1120	1	H$_2$ (10^{-6})	20	4.9	6.5	gl + sp + mel + px	27 – 66[c]	B2-like	(a)
UT-18	1420	1120	1	H$_2$ (10^{-6})	20	3.0	3.8	gl + sp + mel + px	38 – 72[c]	B2-like	(b)
274	1420	1120	1	H$_2$ (10^{-6})	5	10.7	14.7	gl + sp + mel + px	18 – 32[c]	B2-like	(a)
UT-115	1420	1100	1	H$_2$ (10^{-6})	5	10.5	13.5	gl + sp + mel + px + an	12 – 24[c]	B2-like	(b)
329	1420	1120	1	H$_2$ (10^{-5})	50	5.2	5.6	gl + sp + mel + px	19 – 52[c]	incomplete mel rim	(b)
UT-14	1420	1120	1	H$_2$ (10^{-5})	50	3.8	4.4	gl + sp + mel + px	21 – 57[c]	incomplete mel rim	(b)
332	1420	1120	1	H$_2$ (10^{-5})	20	8.8	9.8	gl + sp + mel + px	16 – 54[c]	incomplete mel rim	(b)

UT-3	1420	1100	1	H_2 (10^{-5})	5	17.1	20.4	gl + sp + mel + px + an	7 – 62[c]	B1-like	(b)
UT-37	1420	1100	1	H_2 (10^{-5})	5	9.9	12.1	gl + sp + mel+ px + an (+ gros + Mg-poor sp)	9 – 38[c]	B1-like	(b)
UT-125	1420	1100	1	H_2 (10^{-5})	5	10.5	14.4	gl + sp + mel+ px + an	7 – 49	B1-like	(b)
353	1420	1120	1	H_2 (10^{-4})	50	6.8	8.2	gl + sp + mel + px	12 – 58[c]	B1-like	(b)
UT-21	1420	1120	1	H_2 (10^{-4})	50	10.0	12.0	gl + sp + mel + px	10 – 52[c]	B1-like	(b)
UT-30	1420	1100	1	H_2 (10^{-4})	20	7.8	9.6	gl + sp + mel+ px + an	13 – 60[c]	B1-like	(b)
UT-131	1420	1343	1	H_2 (10^{-4})	5	11.0	13.8	gl + sp + mel	12 – 42[c]	B1-like	(b)
UT-27	1420	1300	1	H_2 (10^{-4})	5	12.5	14.7	gl + sp + mel	10 – 19[c]	B1-like	(b)
356	1420	1235	1	H_2 (10^{-4})	5	14.1	15.9	gl + sp + mel	11 – 21[c]	B1-like	(b)
UT-23	1420	1100	1	H_2 (10^{-4})	5	10.4	13.9	gl + sp + mel + px + an (+ gros + Mg-poor sp)	9 – 65[c]	B1-like	(b)
Isothermal experiments in low-pressure hydrogen											
UT-12	1420		1	H_2 (10^{-5})	/	3.0	/	gl + sp + mel	33 – 39[c]	dendritic	(b)
UT-43	1420		5	H_2 (10^{-5})	/	10.7	/	gl + sp + mel (+ krot + gros)	8 – 31[c]	mel rim / dendritic	(b)
UT-35	1420		15	H_2 (10^{-5})	/	9.7	/	gl + sp + mel (+ gros + Mg-poor sp)	7 – 34[c]	mel rim / dendritic	(b)
UT-41	1420		45	H_2 (10^{-5})	/	20.6	/	gl + sp + mel (+ gros + hib)	7 – 24[c]	mel rim / dendritic	(b)
UT-33	1420		1	H_2 (10^{-4})	/	5.6	/	gl + sp + mel	12 – 32[c]	mel rim / dendritic	(b)

[a]Abbreviations: gl = glass; sp = spinel; mel = melilite; px = pyroxene; an = anorthite; krot = krotite; gros = grossite; hib = hibonite. Phases in the parentheses are minor components identified at the extreme edge of the samples.

[b]Average melilite compositions obtained from the central parts of the grains. Errors are 1 SD of the means.

[c]Melilite compositional ranges randomly obtained in the melilite crystals.

[d]B2-like: randomly distributed melilite crystals through the sample. B1-like: the sample surface continuously surrounded by melilite crystals, similar to type B1 CAIs.

[e]Premelting procedure to make the starting materials. (a) 1520°C for 2 h in air, (b) 1600°C for 10 min and then 1450°C for 10 h in vacuum.

Table 2.3

Experimental conditions and results for isothermal and dynamic crystallization experiments in air and low-pressure hydrogen with CAIδ composition

Run	T_{max}	T_{quench}	Duration at T_{max}	Gas comp.	Cooling rate	Wt. loss		Phases identified[a]	Melilite comp.	Texture[d]	Premelting[c]
	(°C)	(°C)	(h)	(pressure in Pa)	(°C h^{-1})	(%)	(mg cm^{-2})		(Åk%)		
Isothermal experiments in air											
UT-72	1340	1340	5	air	/	/	/	gl + sp	/	/	
UT-77	1325	1325	16.8	air	/	/	/	gl + sp	/	/	
UT-108	1320	1320	23.5	air	/	/	/	gl + sp	/	/	
UT-113	1315	1315	18	air	/	/	/	gl + sp	/	/	
UT-71	1310	1310	6	air	/	/	/	gl + sp + mel	44±3	/	
UT-110	1300	1300	8.7	air	/	/	/	gl + sp + mel	45±5	/	
Dynamic crystallization experiments in low-pressure hydrogen											
UT-80	1420	1100	1	H$_2$ (10^{-6})	50	1.1	1.3	gl + sp + mel	52–66	B2-like	(b)
UT-82	1420	1100	1	H$_2$ (10^{-6})	5	10.3	12.6	gl + sp + mel + px	21–39	B2-like	(b)
UT-87	1420	1100	1	H$_2$ (10^{-5})	50	4.3	5.9	gl + sp + mel + px	40 – 68	incomplete mel rim	(b)
UT-118	1420	1100	1	H$_2$ (10^{-5})	50	5.1	6.1	gl + sp + mel + px	27 – 56	incomplete mel rim	(b)
UT-84	1420	1100	1	H$_2$ (10^{-5})	5	15.8	18.6	gl + sp + mel + px + an	11 – 34	incomplete mel rim	(b)
UT-96	1420	1100	1	H$_2$ (10^{-4})	50	11.0	13.9	gl + sp + mel + px	13 – 50	B1-like	(b)
UT-98	1420	1100	1	H$_2$ (10^{-4})	5	18.6	23.1	gl + sp + mel + px + an	9 – 28	B1-like	(b)
Isothermal experiments in low-pressure hydrogen											
UT-100	1420	1420	1	H$_2$ (10)	/	6.2	/	gl + sp + mel		dendritic	
UT-104	1420	1420	0.5	H$_2$ (10)	/	3.2	/	gl + sp + mel		dendritic	
UT-135	1420	1420	0.5	H$_2$ (10)	/	2.9	/	gl + sp + mel		dendritic	

[a]Abbreviations: gl = glass; sp = spinel; mel = melilite; px = pyroxene; an = anorthite.

[b]Average melilite compositions obtained from the central parts of the grains. Errors are 1 SD of the means.

[c]Melilite compositional ranges randomly obtained in the melilite crystals.

[d]B2-like: randomly distributed melilite crystals through the sample. Mel rim: the sample surface continuously surrounded by melilite crystals, as like type B1 CAIs.

3. Results

3.1. Crystallization experiments in air

3.1.1. Isothermal crystallization experiments in air with CAIχ and CAIδ compositions

The crystallization temperature of melilite was first confirmed for melts with CAIχ and CAIδ compositions by isothermal experiments in air prior to crystallization experiments in low-pressure hydrogen. Because evaporative loss of Mg and Si is negligibly small in air (Mendybaev et al., 2006), melt composition would not change before the onset of melilite crystallization. Melilite is a solid solution between gehlenite ($Ca_2Al_2SiO_7$) and åkermanite ($Ca_2MgSi_2O_7$) and its composition is expressed as a mole fraction of åkermanite content in melilite (hereafter expressed as Åk%). Melilite started to crystallize at 1402.5 ± 2.5°C for CAIχ composition and 1312.5 ± 2.5°C for CAIδ composition as heterogeneously-distributed grains (Fig. 3.1; See also Tables 2.2 and 2.3). The chemical composition of the central part of first-crystallizing melilite crystals in CAIχ melt was ~$Åk_{21}$ and in CAIδ melt it was ~$Åk_{44}$ through the entire sample. Such differences in the liquidus temperature and the composition of first-crystallizing melilite can be expected from their difference in melt composition (Mendybaev et al., 2006), as from more Mg and Si rich melt, more åkermanitic melilite crystallizes at lower temperature. Melilite becomes more Mg-rich (i.e., higher Åk%) with decreasing temperature (Table 2.2).
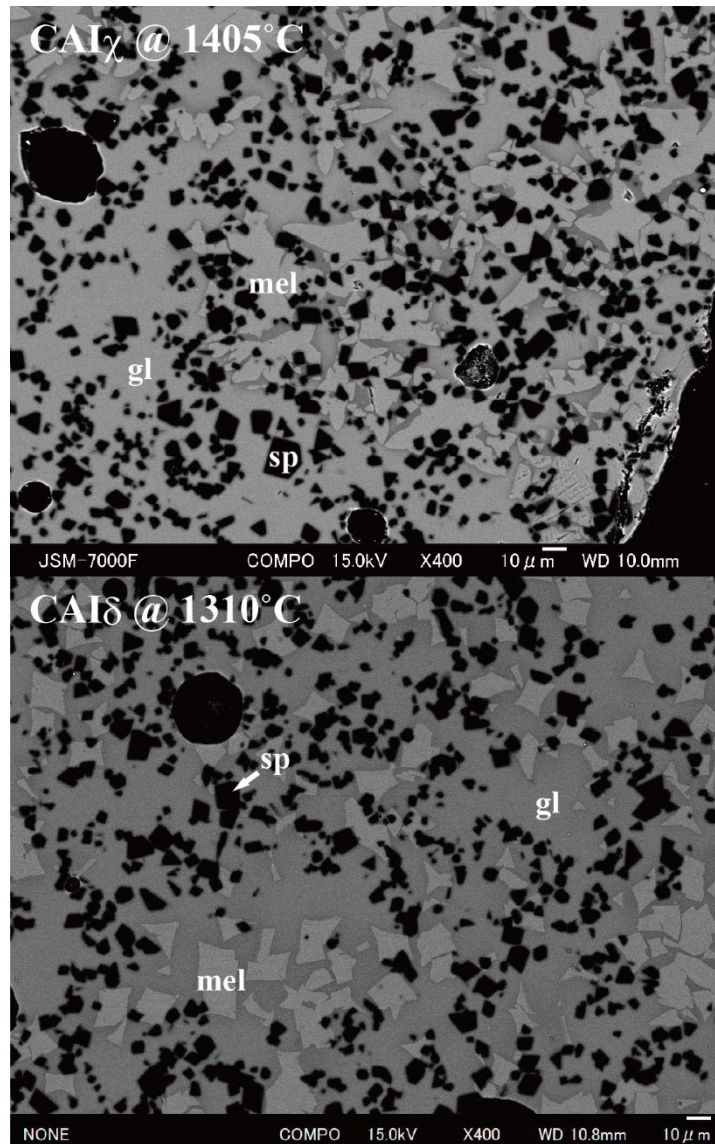
Fig. 3.1. BSE images of isothermal crystallization experiments with CAIχ composition at 1405°C (top) and with CAIδ composition at 1310°C (bottom). Black grains are spinel, light gray grains are melilite, and dark gray parts are glass.

3.1.2. Dynamic crystallization experiment in air with CAIχ composition

A crystallization experiment in air with a cooling rate of 50°C h^{-1} exhibited crystallization of more åkermanitic melilite (Åk$_{43-62}$) compared to that in the isothermal crystallization experiment at 1405°C in air (~Åk$_{21}$) (Table 2.2). This is owing to the effect of undercooling at the point which melilite starts to crystallize (Stolper and Paque, 1986). I also observed that melilite existed randomly through the sample (Fig. 3.2) and the chemical composition of melilite does not correlate with distance from the sample surface.
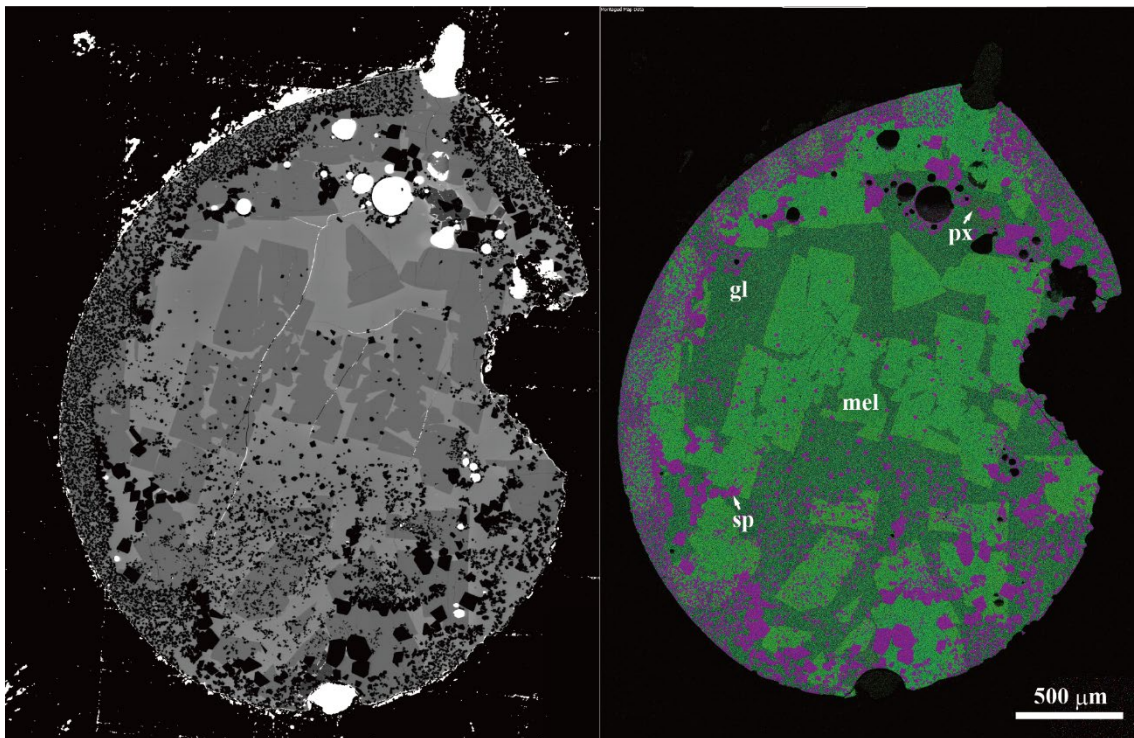
Fig.3.2. BSE images and combined X-ray elemental maps with Mg (red), Ca (green), and Al (blue) of samples heated in air with a cooling rate of 50°C h^{-1} of CAIχ initial composition.

*3.2. Crystallization experiments under low-pressure hydrogen*

3.2.1 Dynamic crystallization experiments in low-pressure hydrogen

Figures 3.3–3.8 show backscattered electron (BSE) images and combined X-ray elemental maps of run products in dynamic crystallization experiments heated at different P_{H2} with controlled cooling rates. The samples in low-P_{H2} experiments contain spinel, melilite, ± pyroxene and ± anorthite depending mainly on quench temperatures of run products (Tables 2.2, 2.3). Pyroxene was present in samples quenched at temperatures lower than 1235°C (Tables 2.2, 2.3), which can be explained by the crystallization temperature of pyroxene for the melt with average type B CAI composition (called as CAIB hereafter) (~1230°C; Stolper, 1982; Stolper and Paque, 1986). Pyroxene crystallization preceded that of anorthite for all the experiments conducted at the cooling rates of 5–50°C h^{-1} at P_{H2} of 10^{-6}–10^{-4} bar. This is consistent with the results from dynamic crystallization experiments of CAIB melt in air conducted at cooling rates of 0.5–1000 °C h^{-1} (Stolper and Paque, 1986). Bulk compositions of some samples in cooling experiments with the CAIχ composition are plotted as MgO and SiO$_2$ concentrations in Fig. 3.9. Their compositions are different from the starting composition (CAIχ), suggesting that evaporative fractionation of elements from the melts. I also found that the bulk compositions of the run products fall within the field of bulk composition of type B CAIs (Grossman et al., 2002).

The samples heated at higher P_{H2} and/or slower cooling rates (UT-23, UT-37) show the presence of grossite (CaAl$_4$O$_7$) at their outermost part (Fig. 3.10, See also Table 2.2), which was also found in the products from laboratory crystallization experiments at 1 atm of hydrogen-dominant gas in Mendybaev et al. (2006). This phase was also observed at the outermost part of natural type B CAIs (Han et al., 2020) and would be formed though incongruent evaporation of pre-existing melilite mantle under hydrogen gas. Mg-depleted spinel grains (down to 22 wt. % MgO) compared to

39

stoichiometric spinel (28.3 wt. % MgO) were found at the rim of those samples (Table 2.2), which were also found in the run products of Mendybaev et al. (2006).
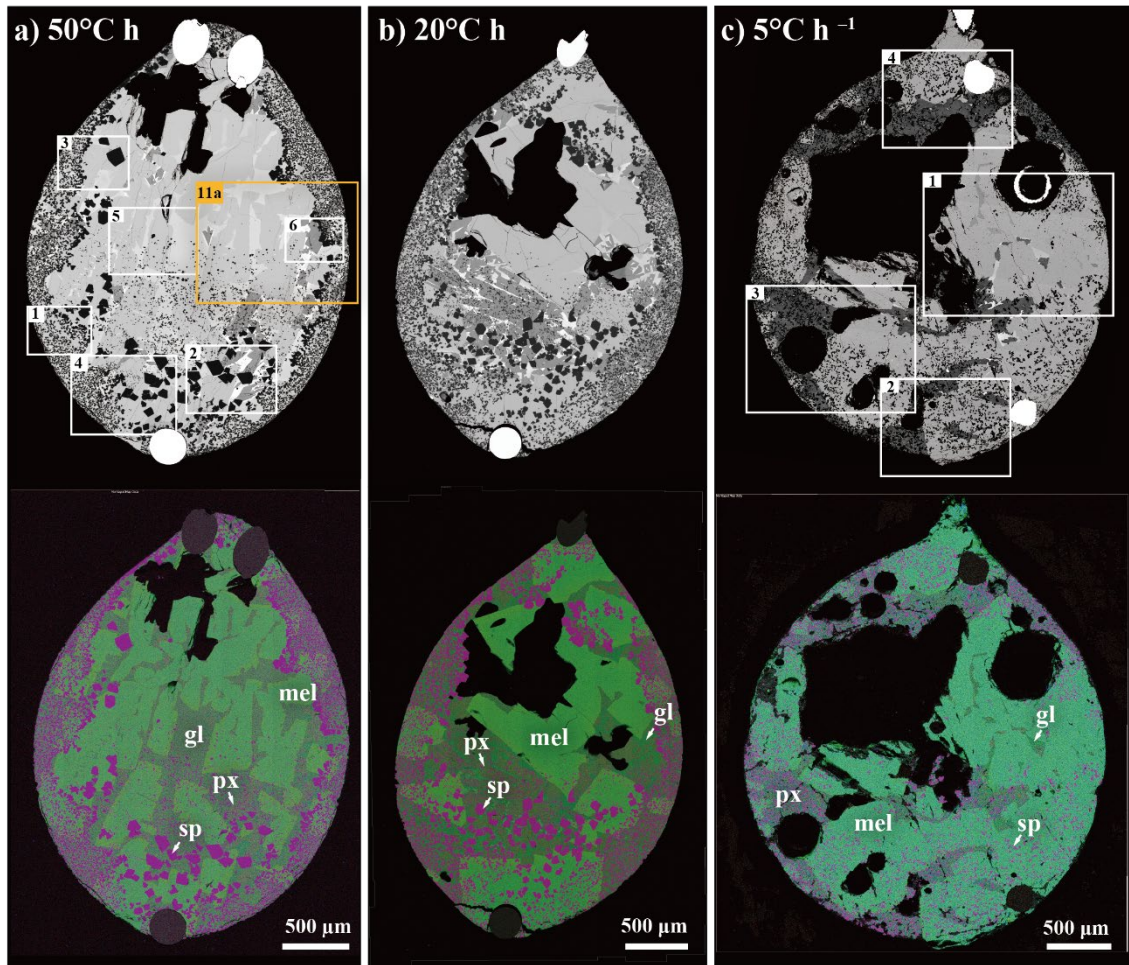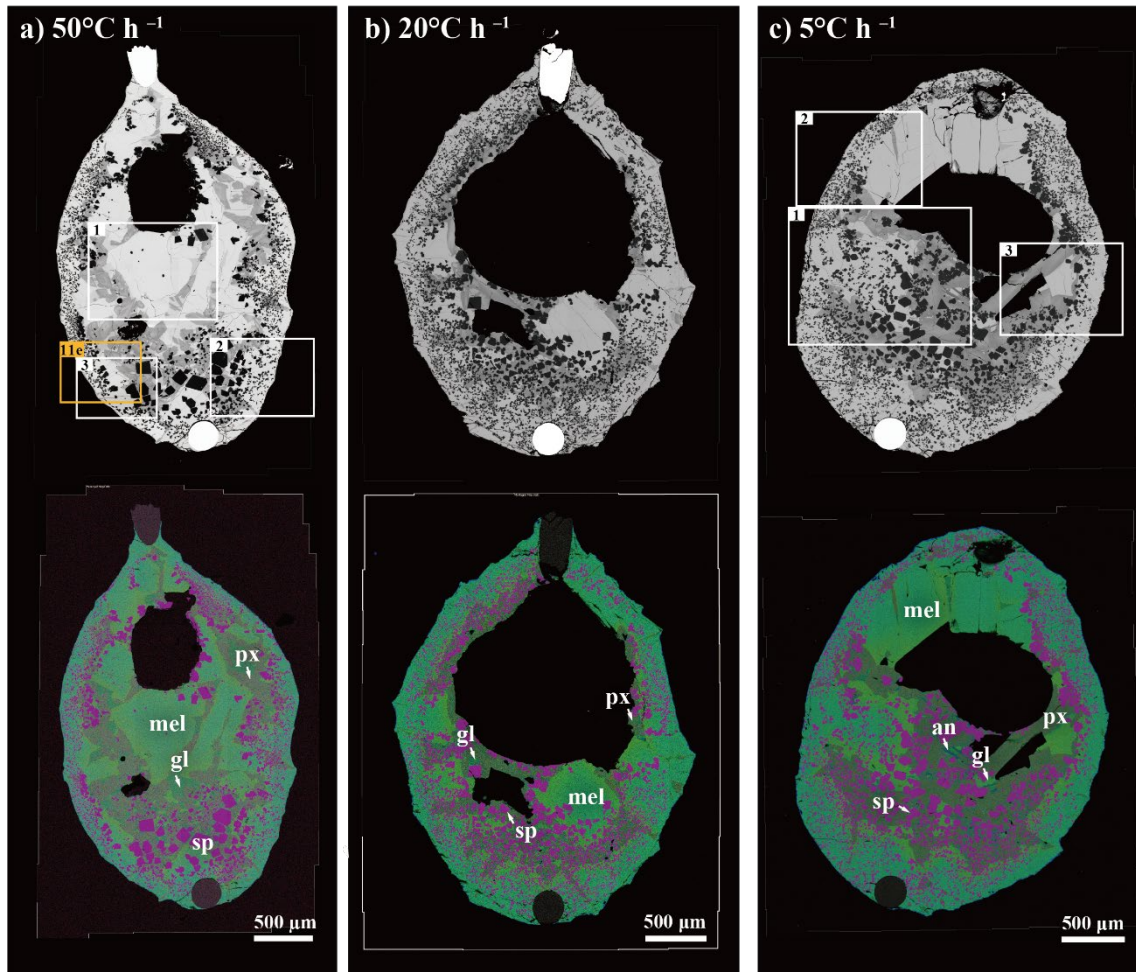
Fig. 3.3 BSE images and combined X-ray elemental maps with Mg (red), Ca (green), and Al (blue) of samples heated at $P_{H2} = 10^{-6}$ bar with CAIχ initial composition. The samples were cooled at different cooling rates. (a) 50°C h^{-1} (UT-16; Table 2.2). (b) 20°C h^{-1} (UT-18; Table 2.2). (c) 5°C h^{-1} (274; Table 2.2). A yellow box numbered 11a corresponds to the area for quantitative mapping of melilite composition as shown in Fig. 3.11.a., and white boxes numbered 1–5 in (a) and 1–4 in (c) are the areas for Mg isotopic analysis shown in Figs. 3.15 and 3.16. gl = glass; sp = spinel; mel = melilite; px = pyroxene.
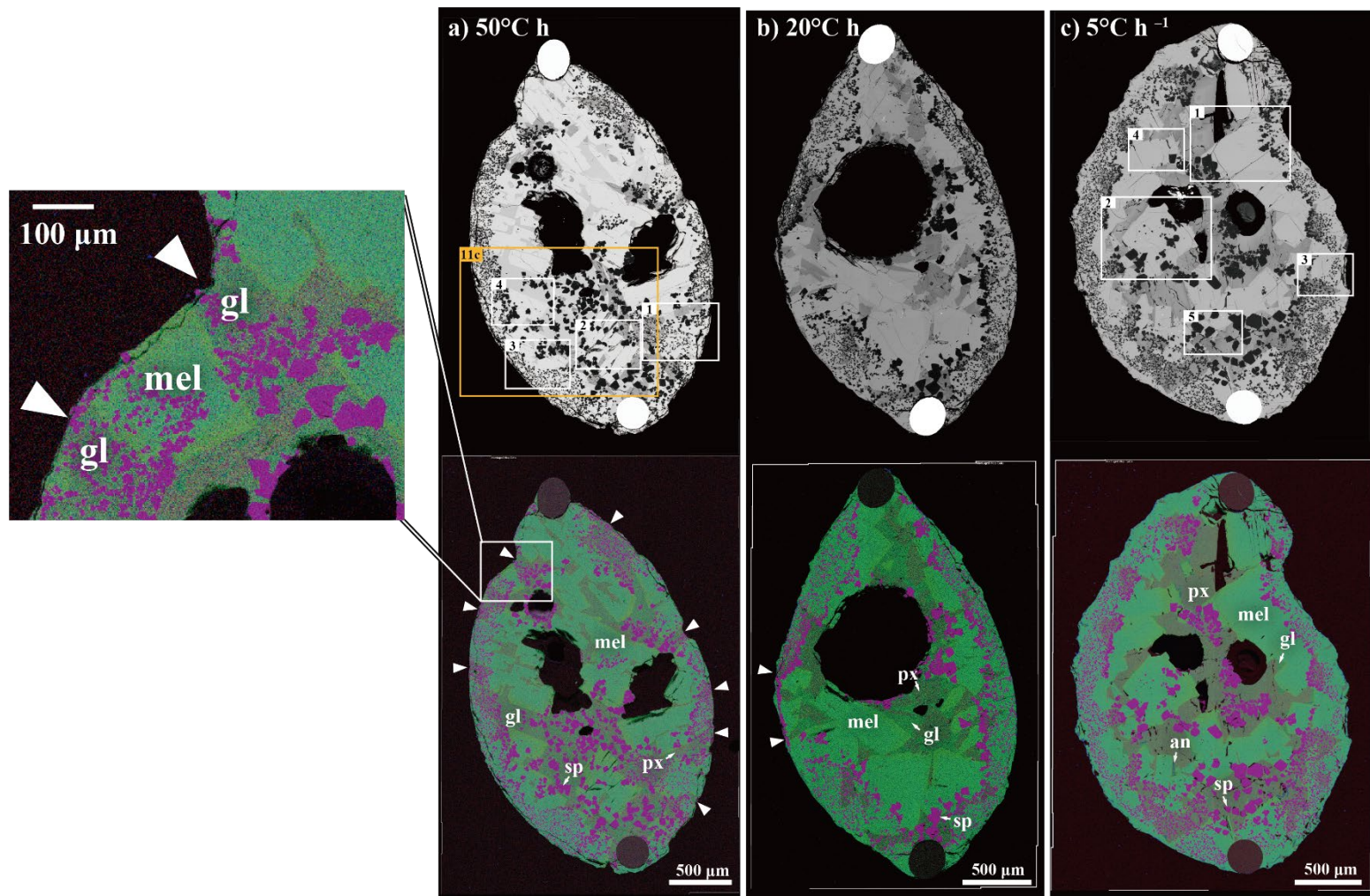
Fig. 3.4 BSE images and combined X-ray elemental maps with Mg (red), Ca (green), and Al (blue) of samples heated at $P_{\mathrm{H2}} = 10^{-5}$ bar with CAIχ
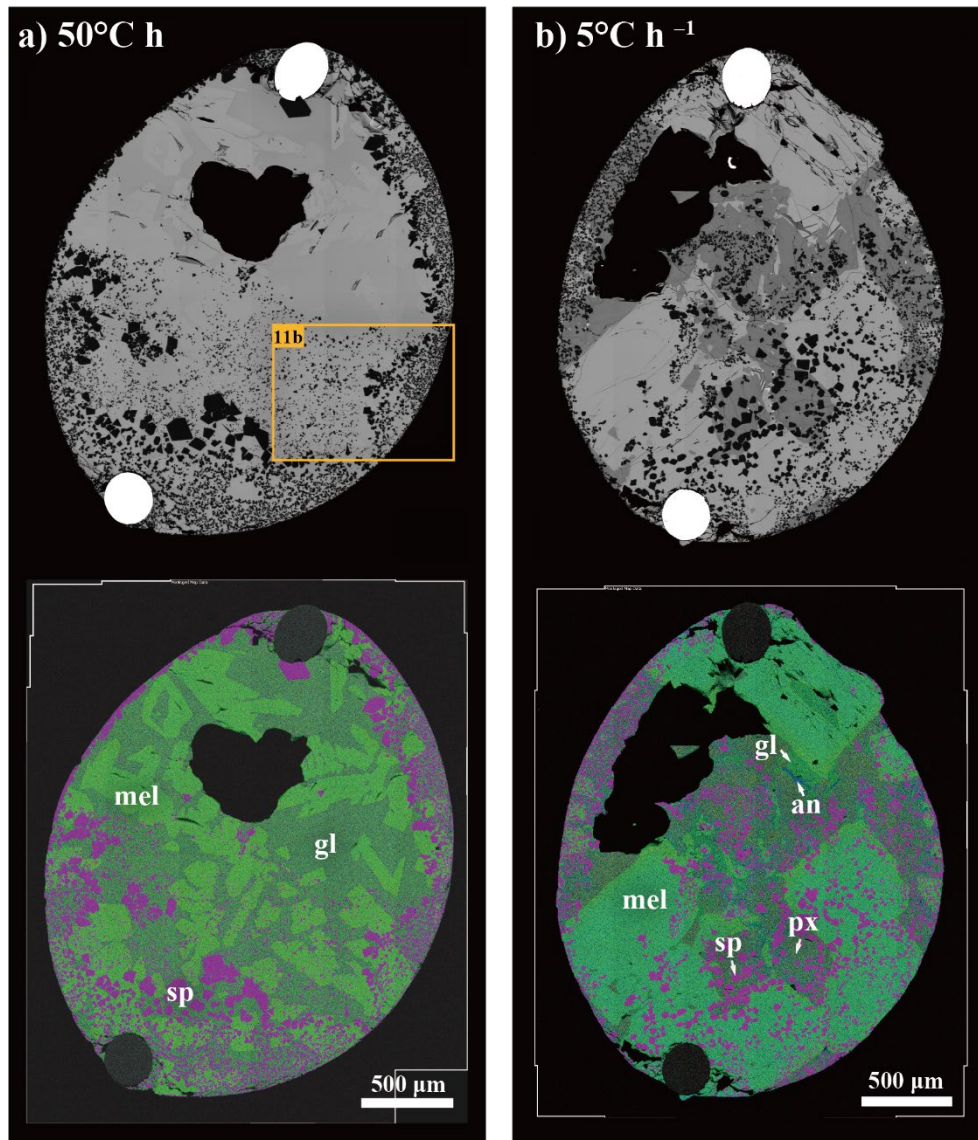
42

initial composition. The samples were cooled at different cooling rates. (a) 50°C h^{-1} (UT-14; Table 2.2). (b) 20°C h^{-1} (329; Table 2.2). (c) 5°C h^{-1} (UT-37; Table 2.2). Triangles in (a) and (b) indicate the regions where no melilite crystals were present at the sample surface. A yellow box numbered 11c corresponds to the area for quantitative mapping of melilite composition as shown in Fig. 3.11.c., and white boxes numbered 1–4 in (a) and 1–5 in (c) are the areas for Mg isotopic analysis shown in Figs. 3.17 and 3.18. gl = glass; sp = spinel; mel = melilite; px = pyroxene; an = anorthite.
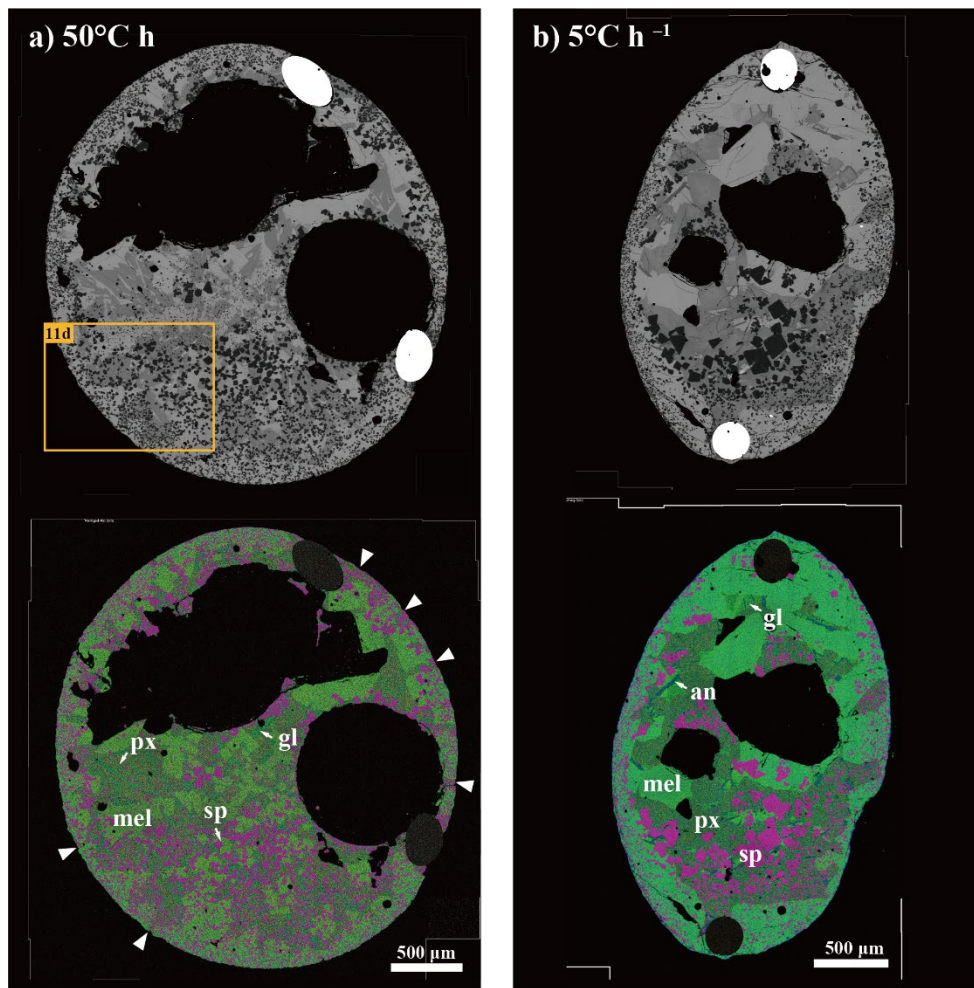
Fig. 3.5 BSE images and combined X-ray elemental maps with Mg (red), Ca (green), and Al (blue) of samples heated at $P_{H2} = 10^{-4}$ bar with CAIχ initial composition. The samples were cooled at different cooling rates. (a) 50°C h^{-1} (353; Table 2.2). (b) 20°C h^{-1} (UT-30; Table 2.2). (c) 5°C h^{-1} (UT-23; Table 2.2). A yellow box numbered 11e corresponds to the area for quantitative mapping of melilite composition as shown in Fig. 3.11.e., and white boxes numbered 1–3 in (a) and 1–3 in (c) are the areas for Mg isotopic analysis shown in Figs. 3.19 and 3.20. gl = glass; sp = spinel; mel = melilite; px = pyroxene; an = anorthite.
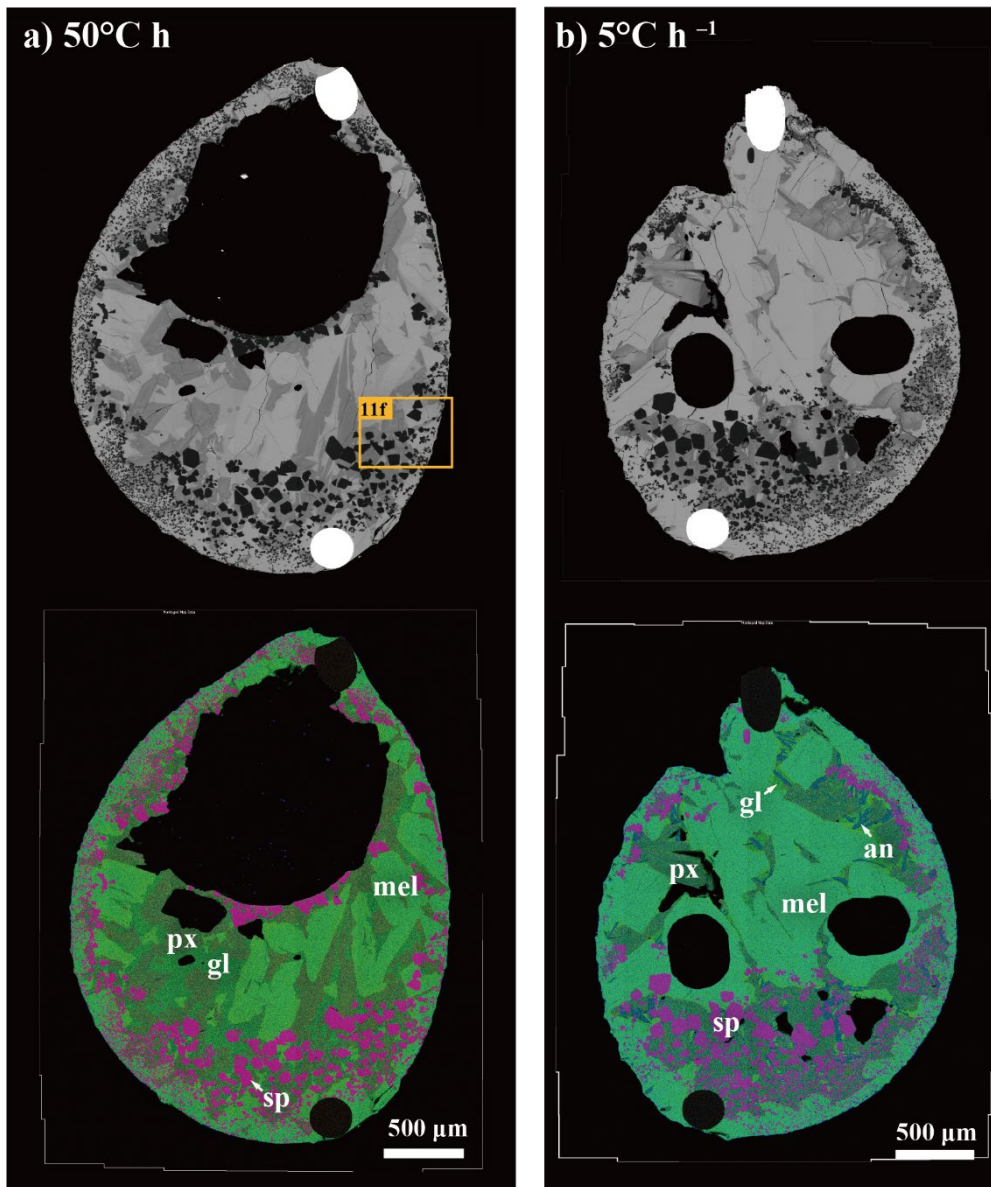
Fig. 3.6 BSE images and combined X-ray elemental maps with Mg (red), Ca (green), and Al (blue) of samples heated at $P_{H2} = 10^{-6}$ bar with CAIδ initial composition. The samples were cooled at different cooling rates. (a) 50°C h^{-1} (UT-80; Table 2.3). (b) 5°C h^{-1} (UT-82; Table 2.3). A yellow box numbered 11b corresponds to the area for quantitative mapping of melilite composition as shown in Fig. 3.11.b. gl = glass; sp = spinel; mel = melilite; px = pyroxene; an = anorthite.

Fig. 3.7 BSE images and combined X-ray elemental maps with Mg (red), Ca (green), and Al (blue) of samples heated at $P_{H2} = 10^{-5}$ bar with CAIδ initial composition. The samples were cooled at different cooling rates. (a) 50°C h^{-1} (UT-87; Table 2.3). (b) 5°C h^{-1} (UT-84; Table 2.3). A yellow box numbered 11d corresponds to the area for quantitative mapping of melilite composition as shown in Fig. 3.11.d. gl = glass; sp = spinel; mel = melilite; px = pyroxene; an = anorthite.

Fig. 3.8 BSE images and combined X-ray elemental maps with Mg (red), Ca (green), and Al (blue) of samples heated at $P_{H2} = 10^{-4}$ bar with CAIδ initial composition. The samples were cooled at different cooling rates. (a) 50°C h^{-1} (UT-96; Table 2.3). (b) 5°C h^{-1} (UT-98; Table 2.3). A yellow box numbered 11f corresponds to the area for quantitative mapping of melilite composition as shown in Fig. 3.11.f. gl = glass; sp = spinel; mel = melilite; px = pyroxene; an = anorthite.
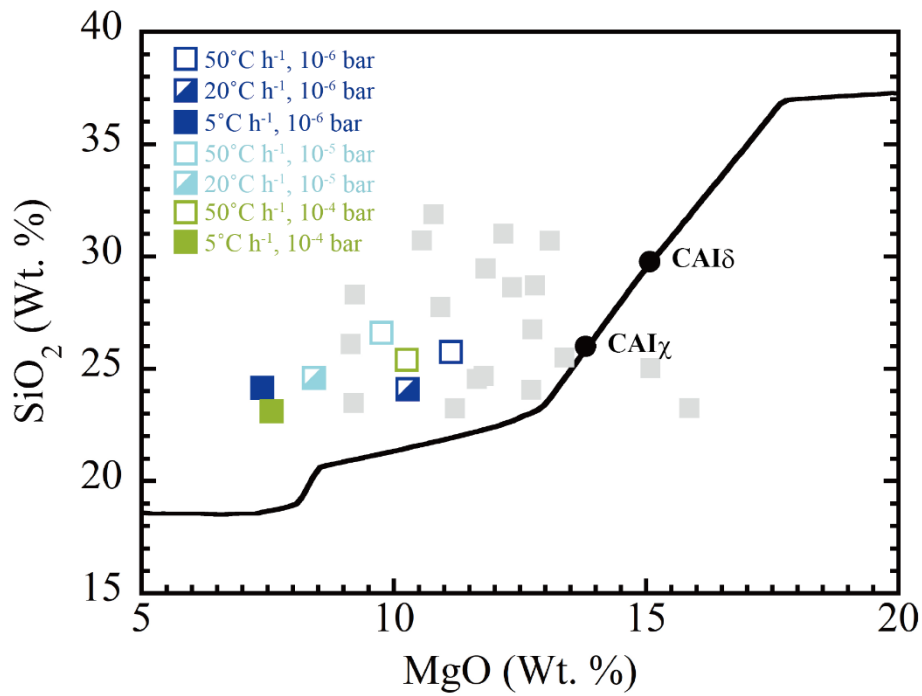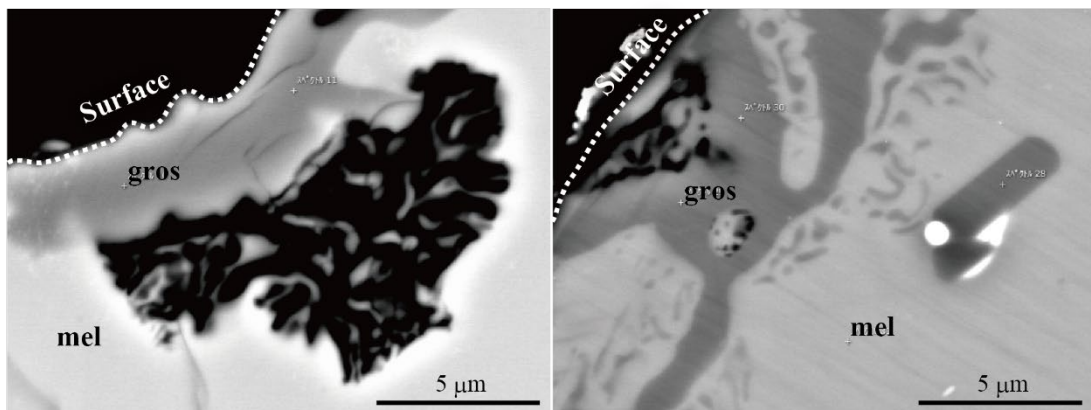
Fig. 3.9. Bulk compositions of the run products in cooling experiments with the CAIχ composition at different P_{H2} and cooling rates (#191, #198, #274, #329, #332, #353, and #356). The gray squares are the bulk compositions of natural type B CAIs shown for comparison (Grossman et al., 2002).


Fig. 3.10. BSE images of grossite ($CaAl_4O_7$) layer observed at the outermost part of the samples cooled at 5°C h^{-1} in $P_{H2} = 10^{-5}$ bar (UT-37; left) and 10^{-6} bar (UT-23; right). Mel = melilite; gros = grossite.

The textural characteristics of melilite crystallized under low-pressure hydrogen condition vary with P_{H2} and cooling rate, but are similar within the same experimental condition with different starting compositions (Figs. 3.3–3.8). Experimental products in $P_{H2} = 10^{-6}$ bar at all cooling rate conditions studied in this experiment show randomly distributed coarse-grained melilite crystals irrespective of the starting composition (Figs. 3.3., 3.6). On the other hand, in samples heated at $P_{H2} = 10^{-5}$ bar at a slower cooling rate (5°C h^{-1}) and $P_{H2} = 10^{-4}$ bar at all cooling rates, the sample surface is continuously surrounded by melilite crystals and resemble the melilite mantle characterized in type B1 CAIs (Figs. 3.4.c, 3.5, 3.7.b, 3.8). The samples cooled at 5°C h^{-1} and $P_{H2} = 10^{-4}$ bar and quenched at different temperatures (UT-131, UT-27, and 356 in Table 2.2) showed that the melilite at the sample rim crystallized preferentially. Incomplete melilite mantle was observed in a sample heated at an intermediate P_{H2} of 10^{-5} bar and cooling rate of 50 and 20°C h^{-1} for CAIχ and P_{H2} of 10^{-5} bar and cooling rate of 50°C h^{-1} for CAIδ (Figs. 3.4.a, 3.4.b, 3.7.a).

Figure 3.11 shows quantitative elemental maps of åkermanite contents of melilite in the areas indicated by boxes in Figs. 3.3–3.8. In the samples cooled at 50°C h^{-1} in $P_{H2} = 10^{-6}$ bar for both compositions (Figs. 3.11.a, b), the åkermanite contents decrease from the core to the rim of the individual melilite grains. On the other hand, in the samples heated at $P_{H2} = 10^{-5}$ and 10^{-4} bar for both compositions, melilite at the outer margin of the sample has low åkermanite contents at the surface and become Åk-rich toward the interior (Figs. 3.11.c–f). Melilite in the inner part of these samples shows the similar chemical zoning as melilite in the samples heated at $P_{H2} =10^{-6}$ bar. Especially, in the sample heated at $P_{H2} = 10^{-4}$ bar for both compositions presented Al-rich melilite at the surface (~Åk$_{10–15}$) (Figs. 3.11.e, f), and such Åk-poor melilite was not observed in samples crystallized from initial composition melt in air (Tables 2.2, 2.3). In experiments at $P_{H2} = 10^{-4}$ bar for CAIχ composition and $P_{H2} = 10^{-5}$ bar and 10^{-4} bar for CAIδ, the lowest åkermanite content was found at the sample surface.
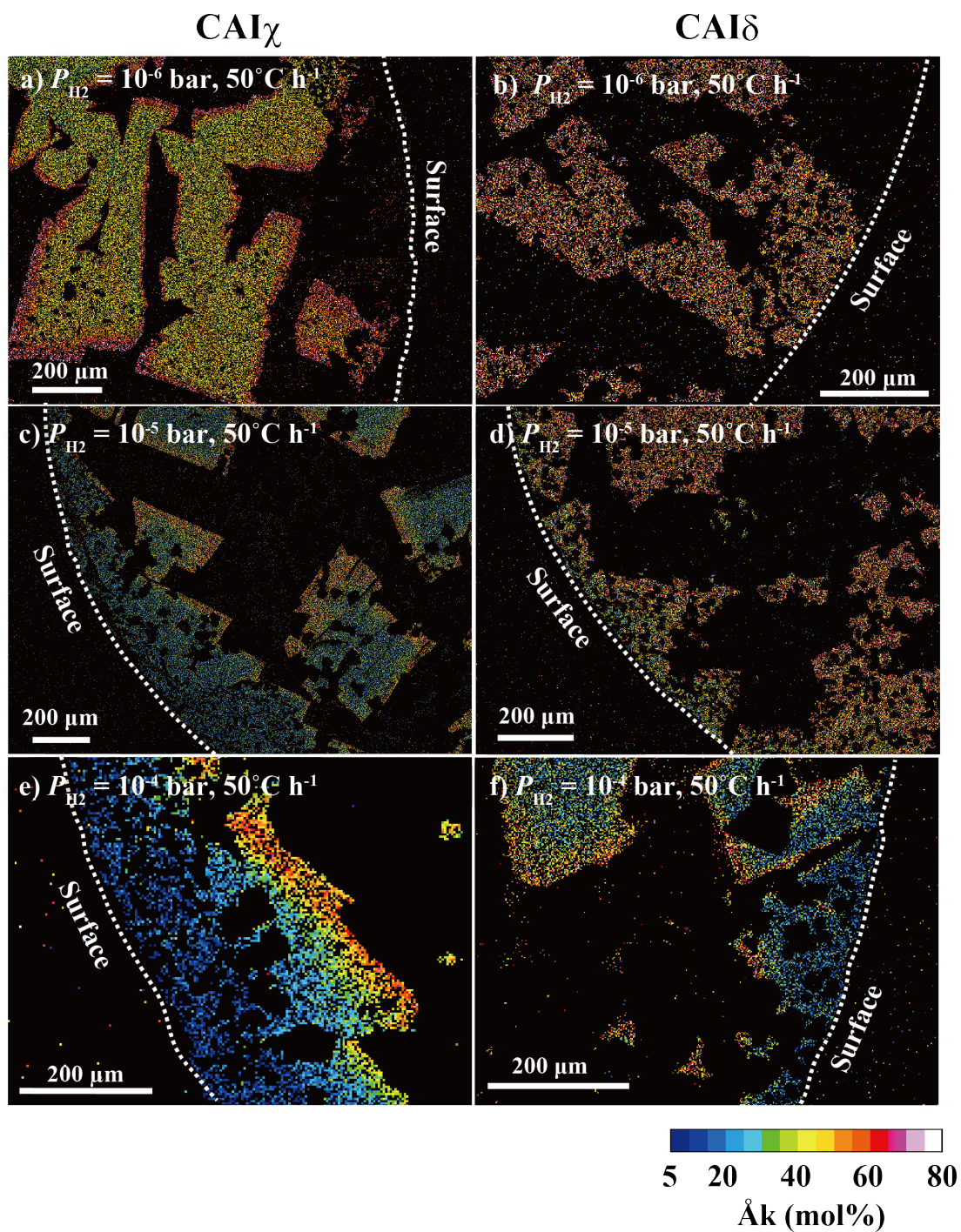
Fig.3.11. Quantitative maps of melilite in the areas shown in Fig. 3.3–3.8. The compositional map shows the differences in åkermanite content (Åk). (a) Melilite in area 2a shown in Fig. 3.3a. (b) Melilite in area 2b shown in Fig. 3.6.a. (c) Melilite locates at the rim in area 3c shown in 3.4.a. (d) Melilite locates at the rim in area 3d shown in Fig. 3.7.a. (e) Melilite locates at the rim in area 3e shown in Fig. 3.5.a. (f) Melilite locates at the rim in area 3f shown in Fig. 3.8.a.

The melilite in the samples cooled at 5 and 50°C h^{-1} at different hydrogen pressures also shows the difference in its compositions (Figs. 3.12, 3.13). For CAIχ composition (Fig. 3.12), more Åk-poor melilite crystallized at the cooling rate of 5°C h^{-1} (Åk$_{16-34}$; Fig. 3.12.a) than that at the cooling rate of 50°C h^{-1} (Åk$_{31-72}$; Fig. 3.12.b) at $P_{H2} = 10^{-6}$ bar. Such decrease in the åkermanite content with slower cooling rate was also observed at $P_{H2} = 10^{-5}$ bar (Figs. 3.12.c, d). In contrast, $P_{H2} = 10^{-4}$ bar, the samples exhibited a similar wide compositional range independent of the cooling rates (Figs. 3.12.e, f). Samples cooled with rates of 5 and 50°C h^{-1} at $P_{H2} = 10^{-4}$ bar, and 5°C h^{-1} at $P_{H2} = 10^{-5}$ bar had melilite with åkermanite contents considerably lower than Åk$_{\sim21}$ (Åk$_{\sim10}$), as seen in Fig. 3.11. In contrast, concerning CAIδ composition, melilite with lower åkermanite content crystallized at higher P_{H2} and slower cooling rate conditions (Fig. 3.13). The samples cooled at 50°C h^{-1} at $P_{H2} = 10^{-6}$ and 10^{-5} bar, whose weight losses are smaller than that in other samples as described below in Fig. 3.14, had melilite with the åkermanite contents comparable with or higher than Åk$_{\sim44}$ (Figs. 3.13.a, c). Melilite in all other samples exhibited åkermanite contents considerably lower than Åk$_{\sim44}$ (Fig. 3.13 b, d, e, f).
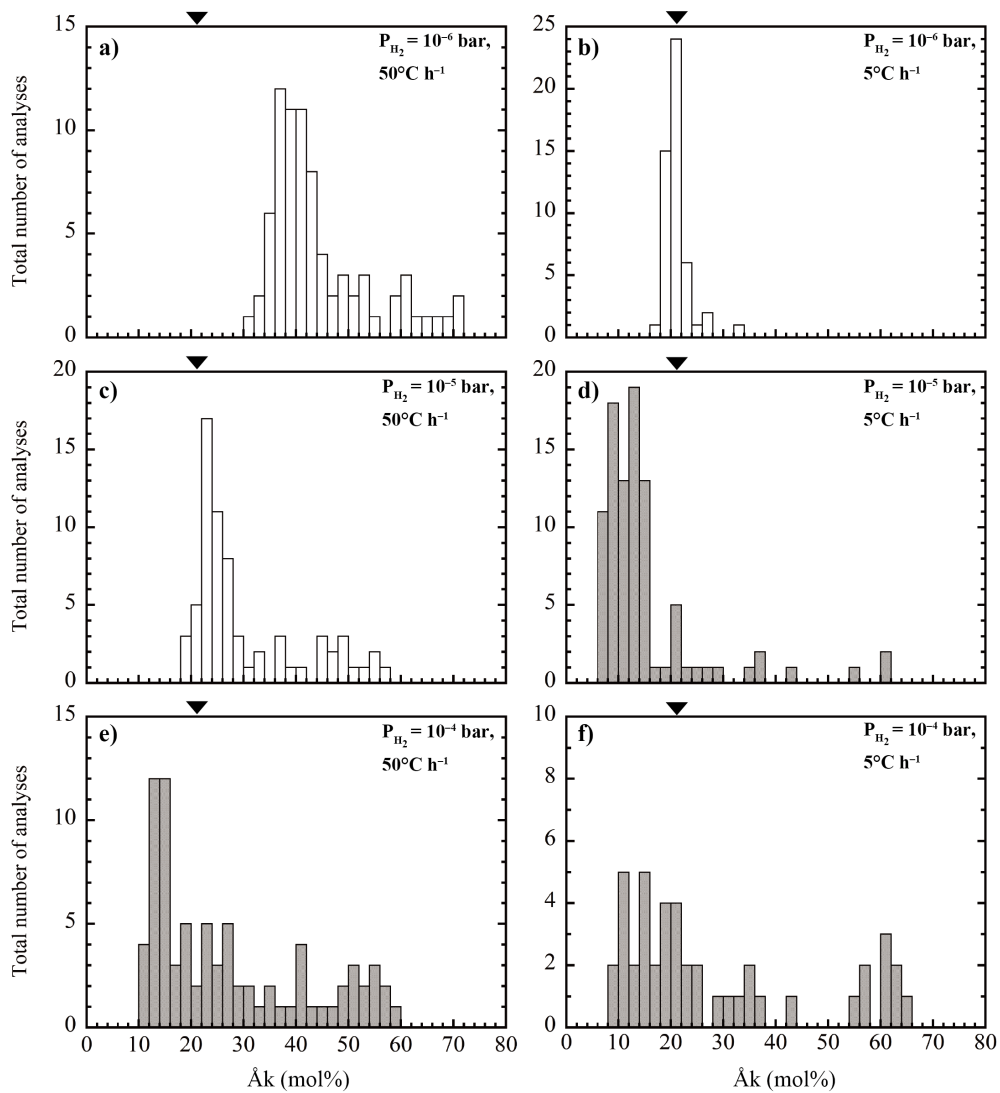
Fig. 3.12. Histograms of the compositions of melilite crystallized under different conditions in experiments with CAIχ composition. $P_{H2} = 10^{-6}$ bar at the cooling rates of (a) 50°C h^{-1} and (b) 5°C h^{-1}. $P_{H2} = 10^{-5}$ bar at the cooling rates of (c) 50°C h^{-1} and (d) 5°C h^{-1}. $P_{H2} = 10^{-4}$ bar at the cooling rates of (e) 50°C h^{-1} and (f) 5°C h^{-1}. White (gray) bars are the melilite compositions of samples without (with) complete melilite mantle. Triangles indicate the composition of first-crystallizing melilite in air from melt with CAIχ composition (Åk~21) (Table 2.2).
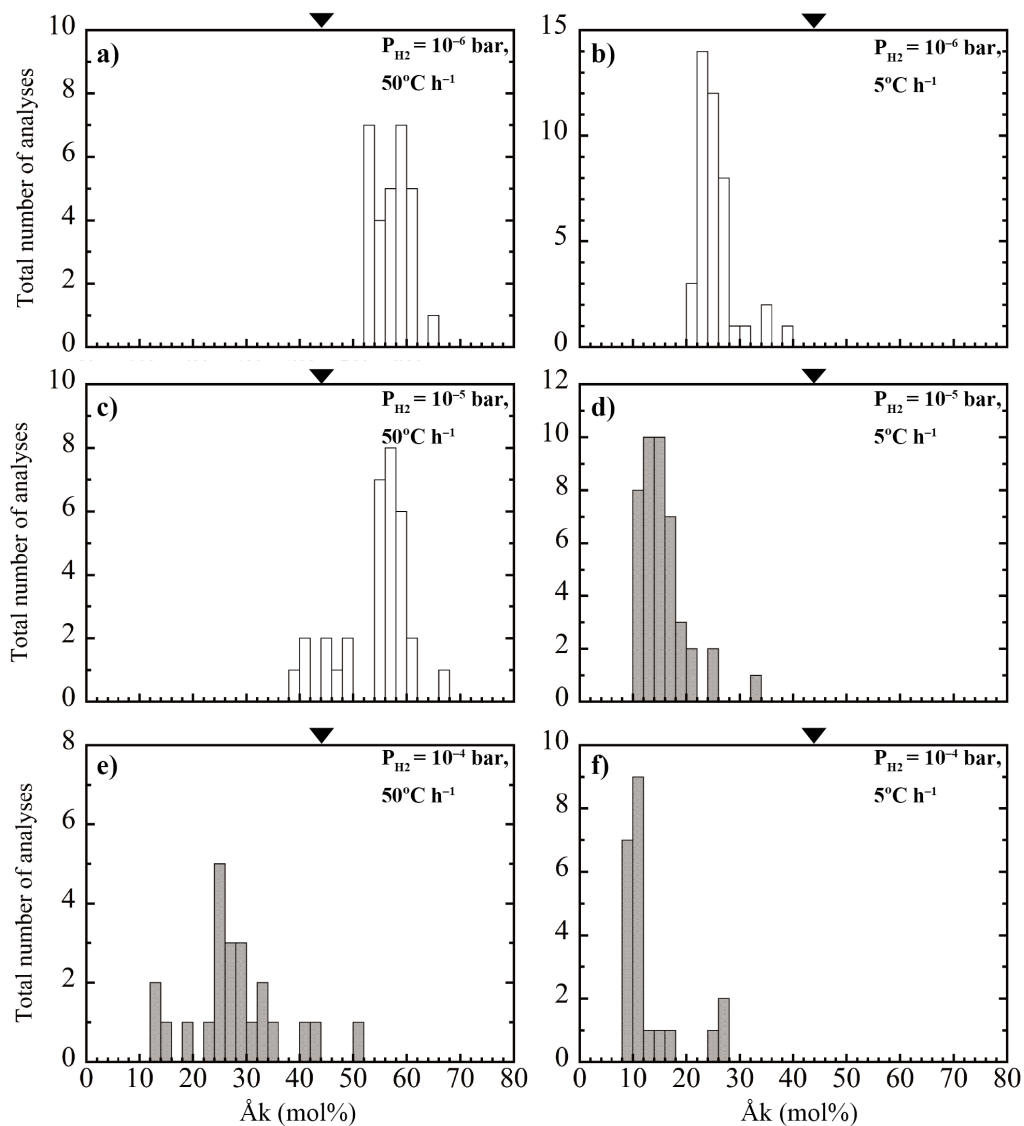
Fig. 3.13. Histograms of the compositions of melilite crystallized under different conditions in experiments with CAIδ composition. $P_{H2} = 10^{-6}$ bar at the cooling rates of (a) 50°C h^{-1} and (b) 5°C h^{-1}. $P_{H2} = 10^{-5}$ bar at the cooling rates of (c) 50°C h^{-1} and (d) 5°C h^{-1}. $P_{H2} = 10^{-4}$ bar at the cooling rate of (e) 50°C h^{-1} and (f) 5°C h^{-1}. White (gray) bars are the melilite compositions of samples without (with) complete melilite mantle. Triangles indicate the composition of first-crystallizing melilite in air from melt with CAIδ composition (Åk~44).

The degree of weight loss of the samples, normalized to the sample surface area, is shown in Fig. 3.14. The surface area was calculated from the initial mass of each sample and the melt density at 1420°C (2.80 and 2.77 g cm^{-3} for CAIχ and CAIδ, respectively) calculated based on Lange and Carmichael (1987) assuming the sample shape to be spherical because the starting materials were more spherical in shape compared with the run products and evaporation takes place at higher temperatures. These weight losses can be attributed to the evaporation of Mg and Si from the melt because the partial pressures of Ca and Al bearing species are sufficiently small compared to those of Mg and Si bearing species (Grossman et al., 2000; Grossman et al., 2002) as discussed in chapter 1.3. In experiments at $P_{H2} = 10^{-6}$ bar with CAIχ composition, where no melilite mantle was formed at the sample surface irrespective of the cooling rate, weight losses increased with decreasing cooling rate. For instance, the weight loss of the sample cooled at 5°C h^{-1} is approximately one order of magnitude larger than that of the samples cooled at 50°C h^{-1}, which can be explained by the difference in the cooling timescale. At $P_{H2} = 10^{-4}$ bar, where melilite rim was always recognized in all the samples, less difference in the weight losses associated with the cooling timescale was observed. Weight losses of the samples also differed with P_{H2}. At a cooling rate of 50°C h^{-1}, the amount of evaporation was roughly proportional to the square root of P_{H2} (i.e., the weight losses of the samples increase roughly by a factor of three with an increase in P_{H2} by one order of magnitude), which is consistent with thermodynamically predicted P_{H2} dependence of evaporation rates (Richter et al. 2002; Mendybaev et al. 2006). In contrast, at the slowest cooling rates of 5°C h^{-1}, the variation in weight losses of the samples was less than that expected from the P_{H2} dependence of evaporation rates (Fig. 3.14).

On the other hand, the weight loss of the experiments with CAIδ composition increased with higher P_{H2} and slower cooling rates irrespective of the

presence or absence of melilite mantle (Fig. 3.14). In experiments at $P_{H2} = 10^{-6}$ bar, the difference in weight losses of the sample cooled at 5°C h^{-1} and 50°C h^{-1} can be explained by the difference in the cooling timescale as in the case of the samples with CAIχ composition at $P_{H2} = 10^{-6}$ bar. At $P_{H2} = 10^{-5}$ and 10^{-4} bar, less difference in the weight losses associated with the cooling timescale was observed. At the cooling rate of 50°C h^{-1}, the amount of evaporation was roughly proportional to the square root of P_{H2} as observed in CAIχ composition. At the slower cooling rates of 5°C h^{-1}, the increase of weight loss was observed with increasing P_{H2}, but the amount of evaporation was less than expected from the difference in P_{H2}.
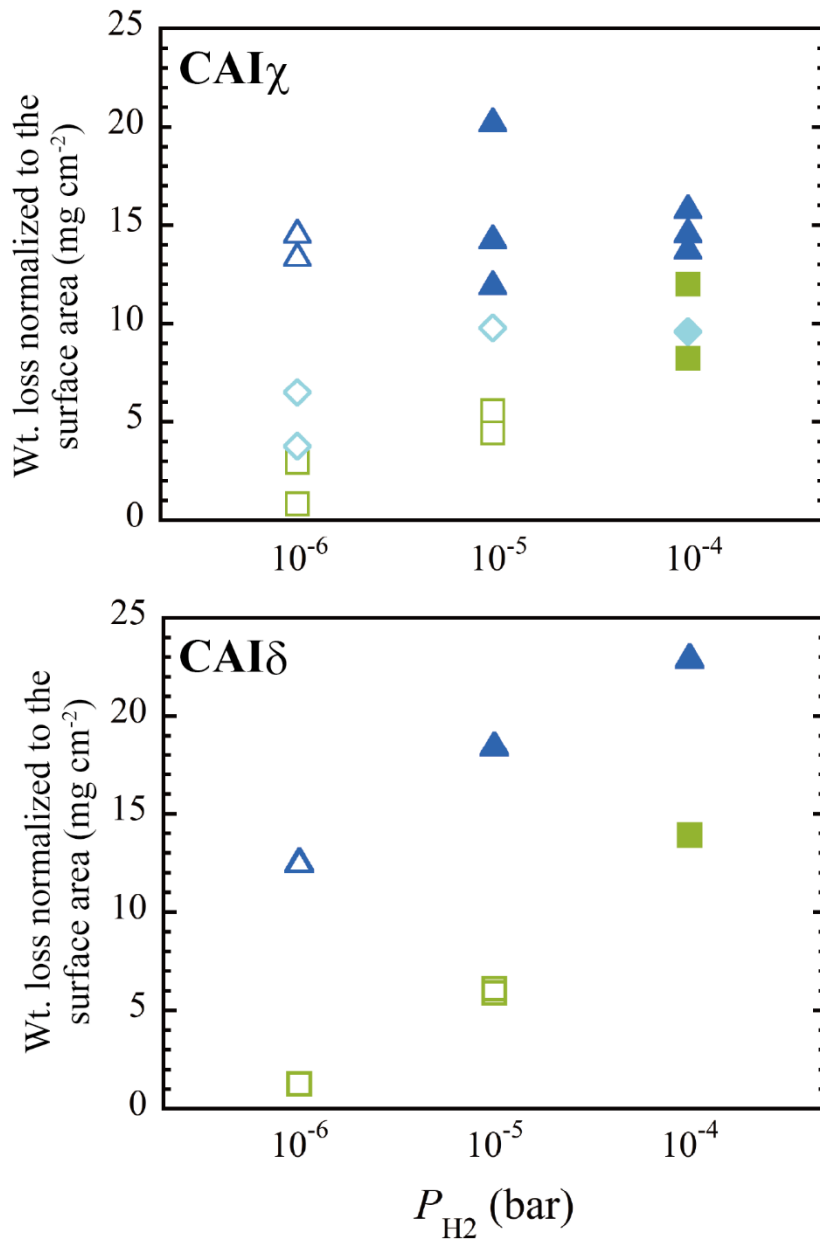
Fig. 3.14. Weight losses of the samples heated at P_{H2} = 10^{-6}, 10^{-5}, and 10^{-4} bar with initial melt composition of CAIχ (top) and CAIδ (bottom). The samples cooled at 50, 20, 5°C h^{-1} are represented by light green square, light blue diamond, dark blue triangles, respectively. Open (filled) symbols represent the samples without (with) complete melilite mantle.

The degree of evaporation and the associated crystallization behavior of melilite can also be seen through the Mg isotopic compositions of melilite because kinetic isotopic fractionation owing to evaporation and diffusion of isotopes within a melt are expected to be recorded in isotopic profiles (e.g., Tsuchiyama et al., 1999; Richter et al., 2005; Yamada et al., 2006). Mg isotopic compositions (expressed as

$$\delta^{25}\mathrm{Mg} = \left[\left(\left({}^{25}\mathrm{Mg} / {}^{24}\mathrm{Mg} \right)_{\mathrm{sample}} \middle/ \left({}^{25}\mathrm{Mg} / {}^{24}\mathrm{Mg} \right)_{\mathrm{ref.}} \right) - 1 \right] \times 1000 \quad (\text{‰})$$

of melilite in samples cooled at 5 and 50°C h^{-1} for CAIχ composition are shown in Figs. 3.15–3.20 and Table 3.1. The range of δ^{25}Mg values of fassaite are shown as gray bands for comparison. At $P_{\mathrm{H2}} = 10^{-5}$ bar with the cooling rate of 50°C h^{-1} and 10^{-4} bar with the cooling rates of 5 and 50°C h^{-1}, the δ^{25}Mg values of melilite increased by 2–6 ‰ toward the surface of the samples from their interior, and remained almost constant inside the sample from 100–200 μm of the surface. (Figs. 3.17, 3.19, 3.20). For the experiment with $P_{\mathrm{H2}} = 10^{-5}$ bar and the cooling rate of 5°C h^{-1}, the elevated δ^{25}Mg values near the sample surface (within ~200 μm from the sample surface) were also observed (Fig. 3.18), and there is a further increase in δ^{25}Mg values toward the center of the sample. On the other hand, at $P_{\mathrm{H2}} = 10^{-6}$ bar, there is no clear correlation between the δ^{25}Mg values and the distance from the sample surface (Figs. 3.15, 3.16). Regarding the relationship between the δ^{25}Mg value and åkermanite content, in the samples with continuous/incomplete melilite mantle at P_{H2} of 10^{-5} and 10^{-4} bar, melilite with the elevated Mg isotopic compositions at the surface had the lowest åkermanite content (Table 3.1). The δ^{25}Mg values of fassaite are comparable to the lowest values of åkermanite-rich melilite in the samples with continuous melilite mantle. In contrast, in the samples cooled at 50 and 5°C h^{-1} with P_{H2} of 10^{-6} bar and 5°C h^{-1} at 10^{-5} bar, the isotopic composition of pyroxene is comparable or similar to the higher end of the isotopic composition of melilite.
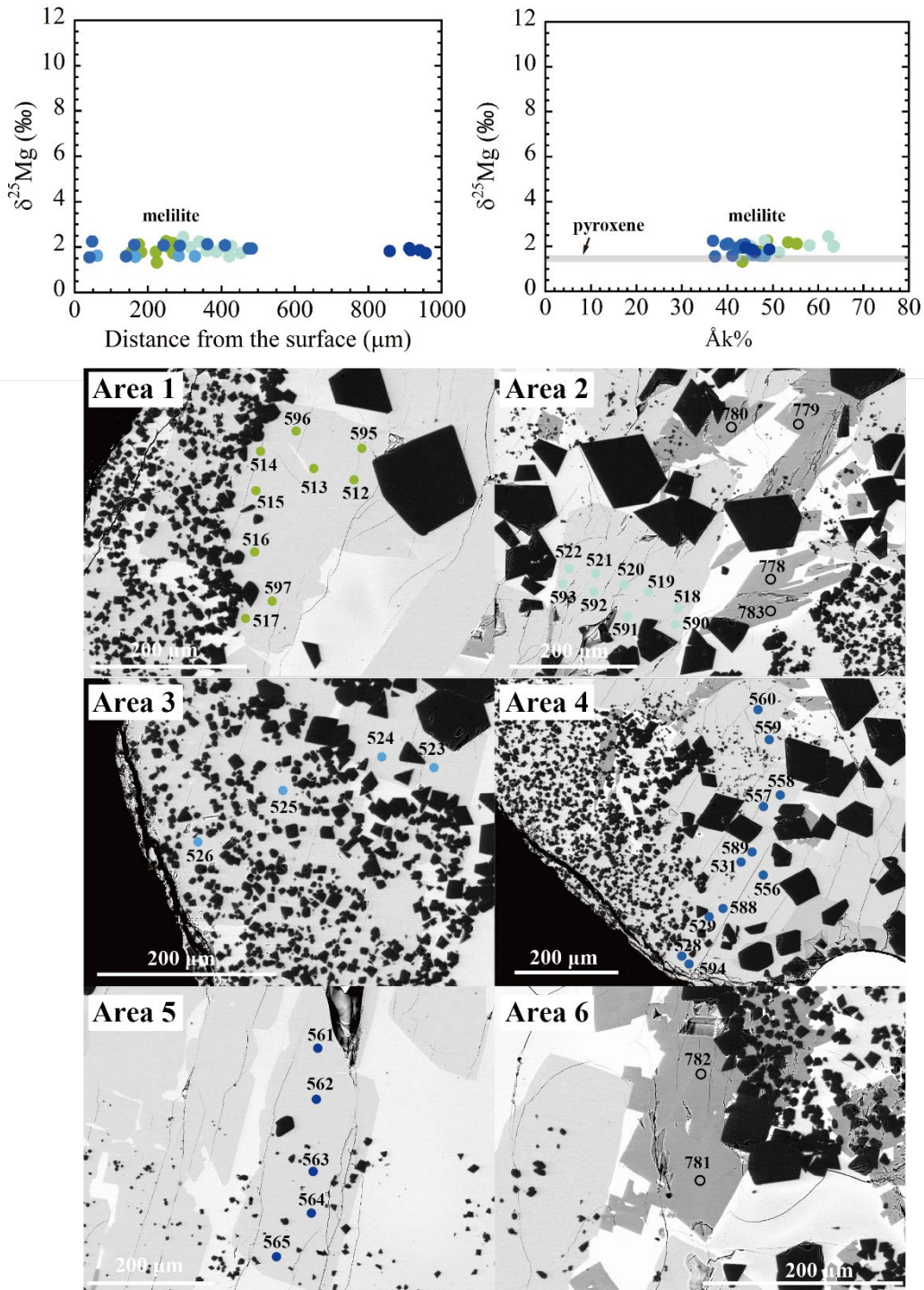
Fig. 3.15 Magnesium isotopic composition of melilite (filled dots) plotted against distance from the sample surface (upper left) and åkermanite content (upper right) in the sample cooled at 50°C h^{-1} and $P_{H2} = 10^{-6}$ bar (UT-16). The isotopic compositional range of pyroxene in the sample displayed in gray band is shown for comparison. Measurement positions for melilite (light gray grain) and pyroxene (dark gray grain) are plotted on BSE images of the areas shown

in Figs. 3.3.a. The color of the filled dots corresponds to the melilite grains in different areas. Open dots are for pyroxene. The spot numbers correspond to the entries listed in Table 1. Error bars on isotopic data are 2SE.
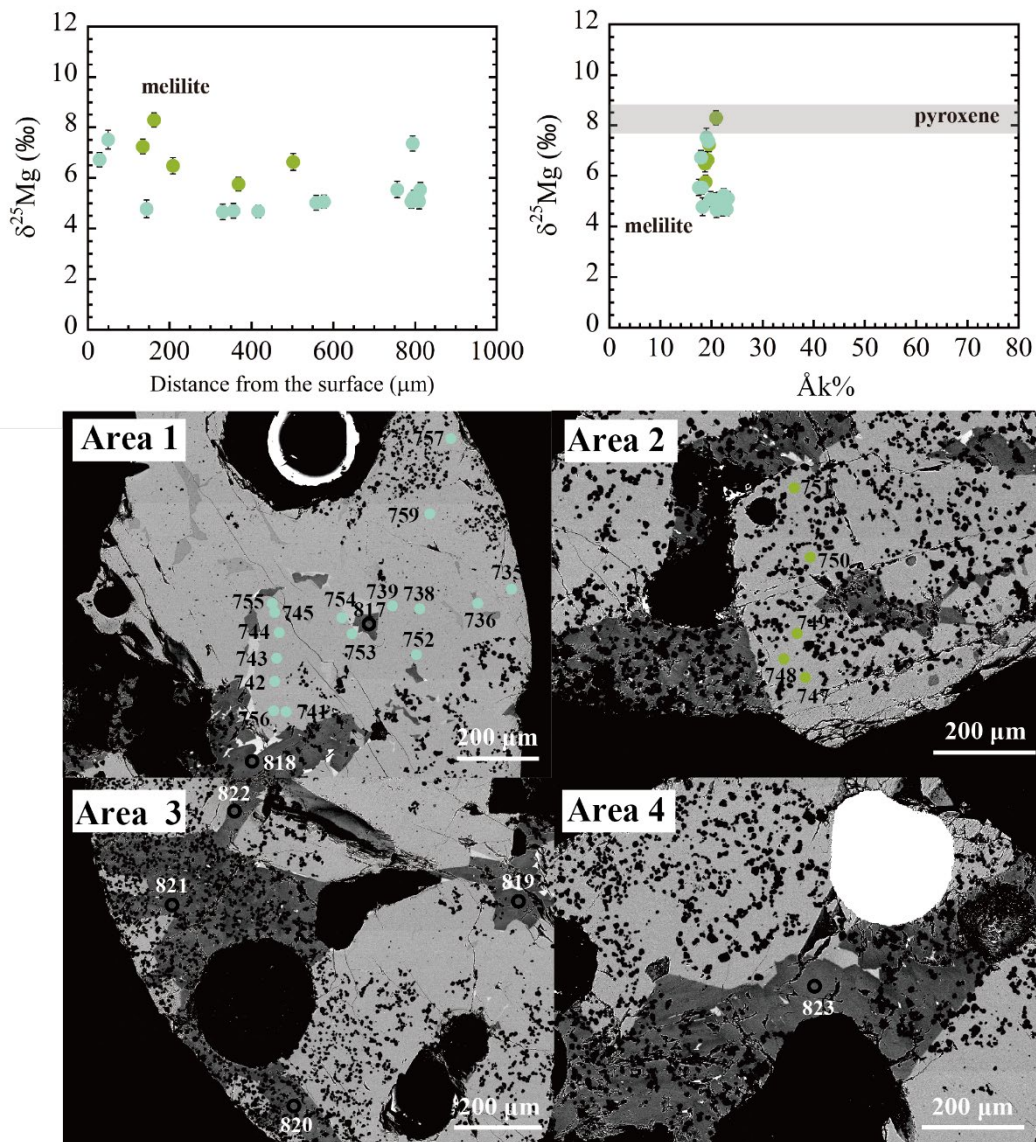
Fig. 3.16. Magnesium isotopic composition of melilite (filled dots) plotted against distance from the sample surface (upper left) and åkermanite content (upper right) in the sample cooled at 5°C h^{-1} and $P_{H2} = 10^{-6}$ bar (Run 274). The isotopic compositional range of pyroxene in the sample displayed in gray band is shown for comparison. Measurement positions for melilite (light gray grain) and pyroxene (dark gray grain) are plotted on BSE images of the areas shown in Figs. 3.3.c.

Fig. 3.17. Magnesium isotopic composition of melilite (filled dots) plotted against distance from the sample surface (upper left) and åkermanite content (upper right) in the sample cooled at 50°C h^{-1} and $P_{H2} = 10^{-5}$ bar (UT-14). The isotopic compositional range of pyroxene in the sample displayed in gray band is shown for comparison. Measurement positions for melilite (light gray grain) and pyroxene (dark gray grain) are plotted on BSE images of the areas shown in Figs. 3.4.a.

Fig. 3.18. Magnesium isotopic composition of melilite (filled dots) plotted against distance from the sample surface (upper left) and åkermanite content (upper right) in the sample cooled at 5°C h^{-1} and P_{H2} = 10^{-5} bar (UT-37).

The isotopic compositional range of pyroxene in the sample displayed in gray band is shown for comparison. Measurement positions for melilite (light gray grain) and pyroxene (dark gray grain) are plotted on BSE images of the areas shown in Figs. 3.4.c.

Fig. 3.19. Magnesium isotopic composition of melilite (filled dots) plotted against distance from the sample surface (upper left) and åkermanite content (upper right) in the sample cooled at 50°C h^{-1} and P_{H2} = 10^{-4} bar (Run 353). The isotopic compositional range of pyroxene in the sample displayed in gray band is shown for comparison. Measurement positions for melilite (light gray grain) and pyroxene (dark gray grain) are plotted on BSE images of the areas shown in Figs. 3.5.a.
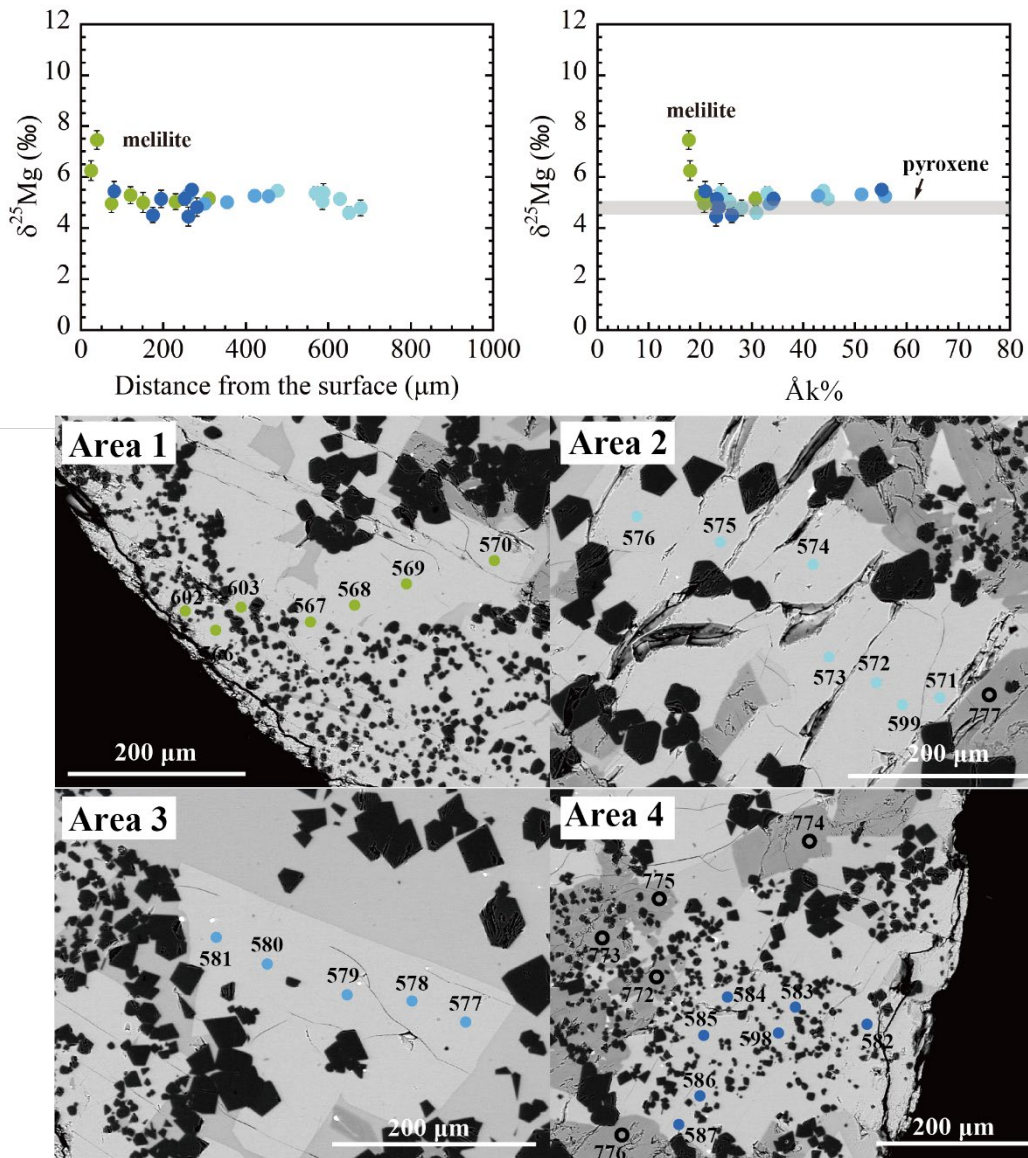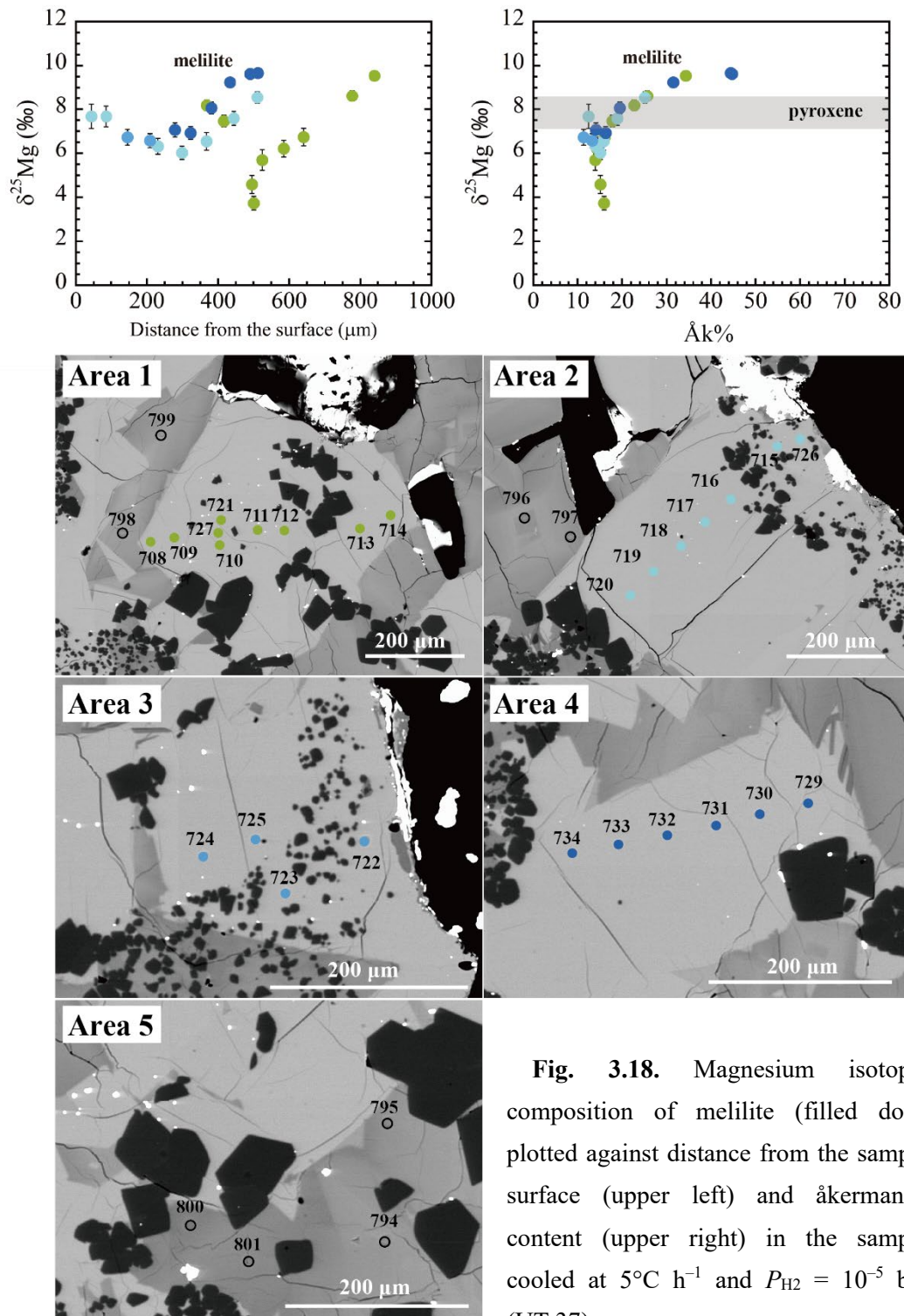
Fig. 3.20 Magnesium isotopic composition of melilite (filled dots) plotted against distance from the sample surface (upper left) and åkermanite content (upper right) in the sample cooled at 5°C h^{-1} and $P_{H2} = 10^{-4}$ bar (UT-23). The isotopic compositional range of pyroxene in the sample displayed in gray band is shown for comparison. Measurement positions for melilite (light gray grain) and pyroxene (dark gray grain) are plotted on BSE images of the areas shown in Figs. 3.5.c.
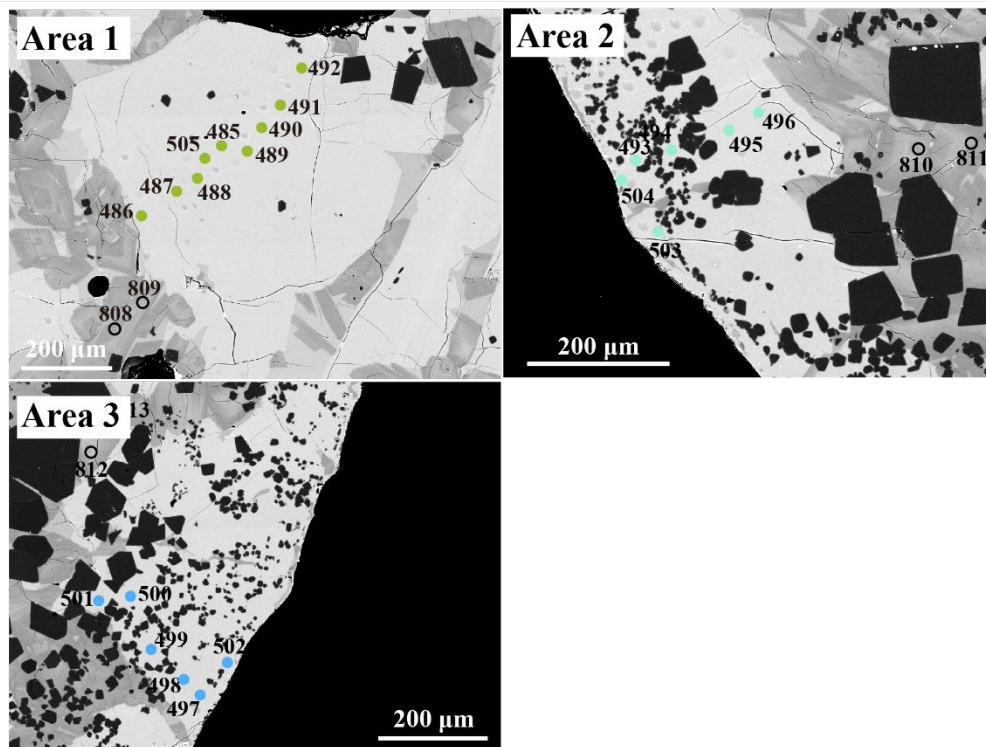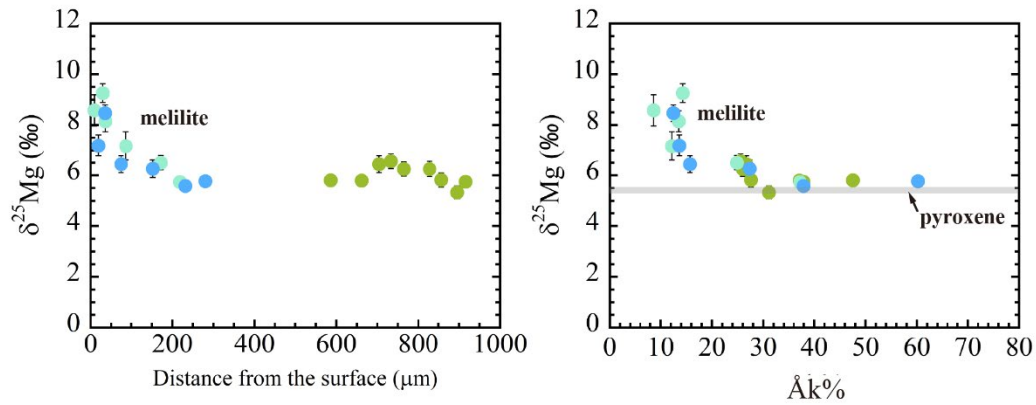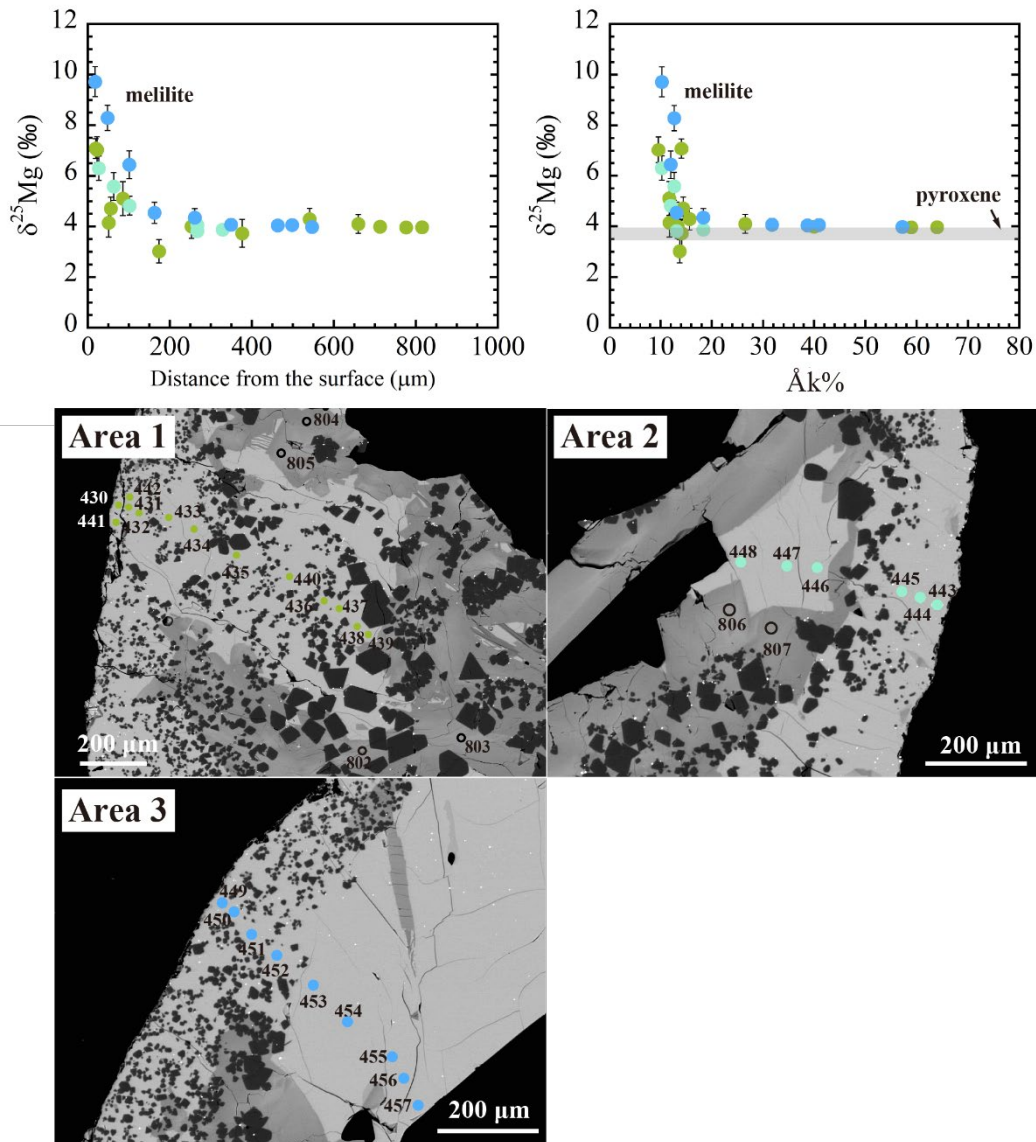
Table3.1 Magnesium isotopic compositions of melilite and pyroxene in dynamic crystallization experiments in low-pressure hydrogen. Errors are 2 SE.

Phases	Spot#	Distance from the surface (μm)	δ^{25}Mg (‰)	Phases	Spot#	Distance from the surface (μm)	δ^{25}Mg (‰)
UT-16					563	940.7	1.87± 0.21
Melilite					564	956.3	1.74± 0.23
Area 1	512	268.9	1.73 ± 0.20		565	915.7	1.87± 0.21
	513	224.3	1.33± 0.22	Pyroxene			
	514	156.2	1.80± 0.19		778	/	1.56± 0.1
	515	181.6	1.78± 0.19		779	/	1.38± 0.13
	516	222.2	1.79± 0.18		780	/	1.44± 0.13
	517	257.3	2.00± 0.17		781	/	1.50± 0.13
	595	249.8	2.26± 0.21		782	/	1.44± 0.13
	596	175.8	2.12± 0.16		783	/	1.52± 0.13
	597	267.0	2.18± 0.15	**Run274**			
Area 2	518	315.8	1.99± 0.20	Melilite			
	519	359.4	1.84± 0.18	Area 1	735	28.3	6.72± 0.28
	520	385.8	1.79± 0.18		736	144.3	4.78± 0.35
	521	420.8	1.59± 0.19		738	329.6	4.66± 0.31
	522	452.9	1.74± 0.20		739	416.1	4.68± 0.25
	590	295.5	2.44± 0.15		741	756.2	5.54± 0.32
	591	339.2	2.25± 0.22		742	812.6	5.54± 0.28
	592	404.2	2.02± 0.22		743	810.1	5.08± 0.30
	593	426.5	2.05± 0.17		744	790.7	5.07± 0.28
Area 3	523	327.9	1.60± 0.20		745	792.4	5.11± 0.26
	524	283.8	1.62± 0.19		752	356.2	4.70± 0.29
	525	166.0	1.58± 0.18		753	558.7	5.02± 0.29
	526	61.9	1.63± 0.20		754	577.4	5.06± 0.26
Area 4	528	40.5	1.55± 0.20		755	796.4	5.24± 0.26
	529	141.0	1.60± 0.19		756	793.9	7.36± 0.30
	556	242.9	2.08± 0.23		757	49.1	7.51± 0.37
	557	361.4	2.13± 0.21		759	45.9	5.80± 0.29
	558	409.5	2.08± 0.22	Area2	747	134.8	7.24± 0.29
	559	474.8	1.94± 0.24		748	162.3	8.29± 0.28
	560	482.9	1.94± 0.22		749	208.4	6.48± 0.32
	588	163.3	2.10± 0.23		750	368.2	5.76± 0.27
	589	286.7	2.06± 0.22		751	502.4	6.63± 0.33
	594	47.6	2.25± 0.24	Pyroxene			
Area 5	561	858.9	1.83± 0.22	Area 2	817	/	7.74± 0.13
	562	912.3	1.95± 0.22		818	/	7.90± 0.13

Phases	Spot#	Distance from the surface (µm)	δ^{25}Mg (‰)	Phases	Spot#	Distance from the surface (µm)	δ^{25}Mg (‰)
Area 3	819	/	7.87± 0.13		775	/	4.76± 0.13
	820	/	8.69± 0.13		776	/	4.67± 0.13
	821	/	8.45± 0.13	Area 2	777	/	4.62± 0.13
	822	/	8.07± 0.13	**UT-37**			
Area 4	823	/	8.68± 0.13	melilite			
UT-14				Area 1	708	368.0	8.17± 0.24
Melilite					709	416.0	7.46± 0.26
Area 1	566	38.5	7.45± 0.37		710	501.2	3.73± 0.31
	567	120.7	5.29± 0.33		711	585.2	6.21± 0.38
	568	151.6	5.00± 0.39		712	640.7	6.73± 0.40
	569	230.0	5.03± 0.31		713	777.0	8.61± 0.25
	570	310.4	5.15± 0.25		714	840.5	9.54± 0.18
	602	24.4	6.25± 0.19		721	524.9	5.69± 0.47
	603	74.3	4.96± 0.35		727	496.0	4.58± 0.41
Area 2	571	477.3	5.46± 0.21	Area 2	715	85.9	7.67± 0.47
	572	588.3	5.39± 0.34		716	231.5	6.31± 0.36
	573	586.2	5.04± 0.31		717	298.9	6.02± 0.30
	574	678.7	4.79± 0.31		718	367.6	6.54± 0.40
	575	650.3	4.60± 0.25		719	444.6	7.58± 0.32
	576	628.5	5.14± 0.21		720	511.1	8.54± 0.27
	599	569.5	5.37± 0.25		726	43.5	7.67± 0.55
Area 3	577	455.1	5.25± 0.16	Area 3	723	146.1	6.72± 0.36
	578	420.9	5.27± 0.22		724	209.1	6.57± 0.32
	579	354.3	5.01± 0.23		728	157.3	6.62± 0.37
	580	299.9	4.95± 0.23	Area 4	729	512.6	9.66± 0.17
	581	261.5	5.32± 0.16		730	491.0	9.62± 0.17
Area 4	582	81.3	5.44± 0.39		731	433.6	9.24± 0.16
	583	175.1	4.51± 0.30		732	381.1	8.05± 0.27
	584	260.9	4.45± 0.37		733	322.6	6.92± 0.29
	585	281.6	4.82± 0.36		734	279.0	7.06± 0.32
	586	251.9	5.15± 0.25	Pyroxene			
	587	269.0	5.50± 0.16	Area 5	794	/	7.80± 0.13
	598	195.2	5.14± 0.34		795	/	7.91± 0.13
	601	26.8	6.15± 0.32		800	/	7.01± 0.14
Pyroxene					801	/	7.79± 0.13
Area 4	772	/	4.53± 0.14	Area 6	796	/	8.28± 0.14
	773	/	4.70± 0.13		797	/	8.23± 0.13
	774	/	5.07± 0.14	Area 1	798	/	8.52± 0.13

| Phases	Spot#	Distance from the surface (µm)	δ²⁵Mg (‰)	Phases	Spot#	Distance from the surface (µm)	δ²⁵Mg (‰)
	799	/	8.42± 0.13		431	51.0	4.15± 0.57
Run353					432	85.5	5.10± 0.67
Melilite					433	173.9	3.02± 0.46
Area 1	485	764.9	6.25± 0.28		434	252.9	4.00± 0.47
	486	586.6	5.81± 0.18		435	376.6	3.73± 0.55
	487	662.0	5.79± 0.20		436	660.1	4.10± 0.37
	488	704.5	6.44± 0.33		437	713.0	3.99± 0.22
	489	827.9	6.25± 0.30		438	776.4	3.96± 0.18
	490	856.7	5.82± 0.28		439	815.6	3.97± 0.17
	491	895.5	5.33± 0.25		440	541.0	4.29± 0.43
	492	916.1	5.75± 0.20		441	19.4	7.08± 0.39
	505	733.1	6.56± 0.30		442	55.8	4.71± 0.45
Area 2	493	36.1	8.15± 0.41	Area 2	443	26.9	6.30± 0.48
	494	86.7	7.17± 0.57		444	63.1	5.58± 0.55
	495	171.8	6.50± 0.28		445	102.0	4.82± 0.37
	496	218.5	5.74± 0.21		446	267.2	3.82± 0.17
	503	29.7	9.26± 0.37		447	328.9	3.87± 0.18
	504	9.2	8.58± 0.62		448	267.2	4.06± 0.16
Area 3	497	35.2	8.47± 0.33	Area 3	449	17.7	9.72± 0.59
	498	74.8	6.44± 0.33		450	48.0	8.29± 0.50
	499	152.7	6.26± 0.34		451	101.0	6.44± 0.55
	500	231.8	5.58± 0.18		452	162.5	4.54± 0.42
	501	280.2	5.77± 0.18		453	260.8	4.35± 0.36
	502	18.8	7.19± 0.42		454	349.3	4.07± 0.24
Pyroxene					455	463.3	4.04± 0.21
Area 1	808	/	5.32± 0.13		456	498.4	4.06± 0.19
	809	/	5.51± 0.14		457	546.7	3.98± 0.17
Area 2	810	/	5.47± 0.13	Pyroxene			
	811	/	5.54± 0.13	Area 1	802	/	3.69± 0.13
Area 3	812	/	5.31± 0.13		803	/	3.62± 0.14
	813	/	5.30± 0.13		804	/	3.69± 0.13
UT-23					805	/	3.79± 0.13
Melilite				Area 2	806	/	3.62± 0.13
Area 1	430	22.4	7.03± 0.52		807	/	3.47± 0.13

3.2.2 Isothermal experiments in low-pressure hydrogen

Isothermal heating experiments at P_{H2} of 10^{-5}, 10^{-4} bar were conducted at 1420°C, which is above the melilite crystallization temperature for both composition melt (1402.5 ± 2.5°C for CAIχ composition and 1312.5 ± 2.5°C for CAIδ). For CAIχ composition, the sample heated at $P_{H2} = 10^{-5}$ bar for 1 h exhibited only dendritic melilite, which is expected to form during the quenching based on its textural feature and Mg-rich compositions (~$Åk_{33-39}$) (Fig, 3.21.a, Table 2.2). On the other hand, the samples heated for 5–45 h exhibited preferential crystallization of coarse-grained Mg-poor melilite (~$Åk_7$) at the surface (Figs. 3.21.b–d, Table 2.2). The coarse-grained melilite at the sample surface was also observed in the sample heated at $P_{H2} = 10^{-4}$ bar for 1 h (Fig. 3.22.a). I therefore conclude that melilite mantle observed in the cooling experiments at $P_{H2} = 10^{-5}$ and 10^{-4} bar crystallized during the cooling and 1-h heating at the maximum temperature (1420°C), respectively. Crystallization of Ca, Al-rich phases such as krotite ($CaAl_2O_4$), grossite ($CaAl_4O_7$), and hibonite ($CaAl_{12}O_{19}$) were observed at the outermost part of samples with coarse-grained melilite at the surface (Table 2.2). Those phases correspond to the products of incongruent evaporation of pre-existing coarse-grained melilite at the surface as observed in the dynamic crystallization experiments in low-pressure hydrogen (Fig. 3.10; Table 2.2). Mg-depleted spinel is also observed as in the case of the samples in dynamic crystallization experiments in low-pressure hydrogen (Table 2.2). For CAIδ composition, only dendritic melilite is observed in the sample heated at $P_{H2} = 10^{-4}$ bar for a duration shorter than 1 h (Fig. 3.22.b; Table 2.3). Therefore, the melilite at the surface crystallized in dynamic crystallization experiments at $P_{H2} = 10^{-5}$ and 10^{-4} bar is considered to have crystallized during the cooling with CAIδ composition.
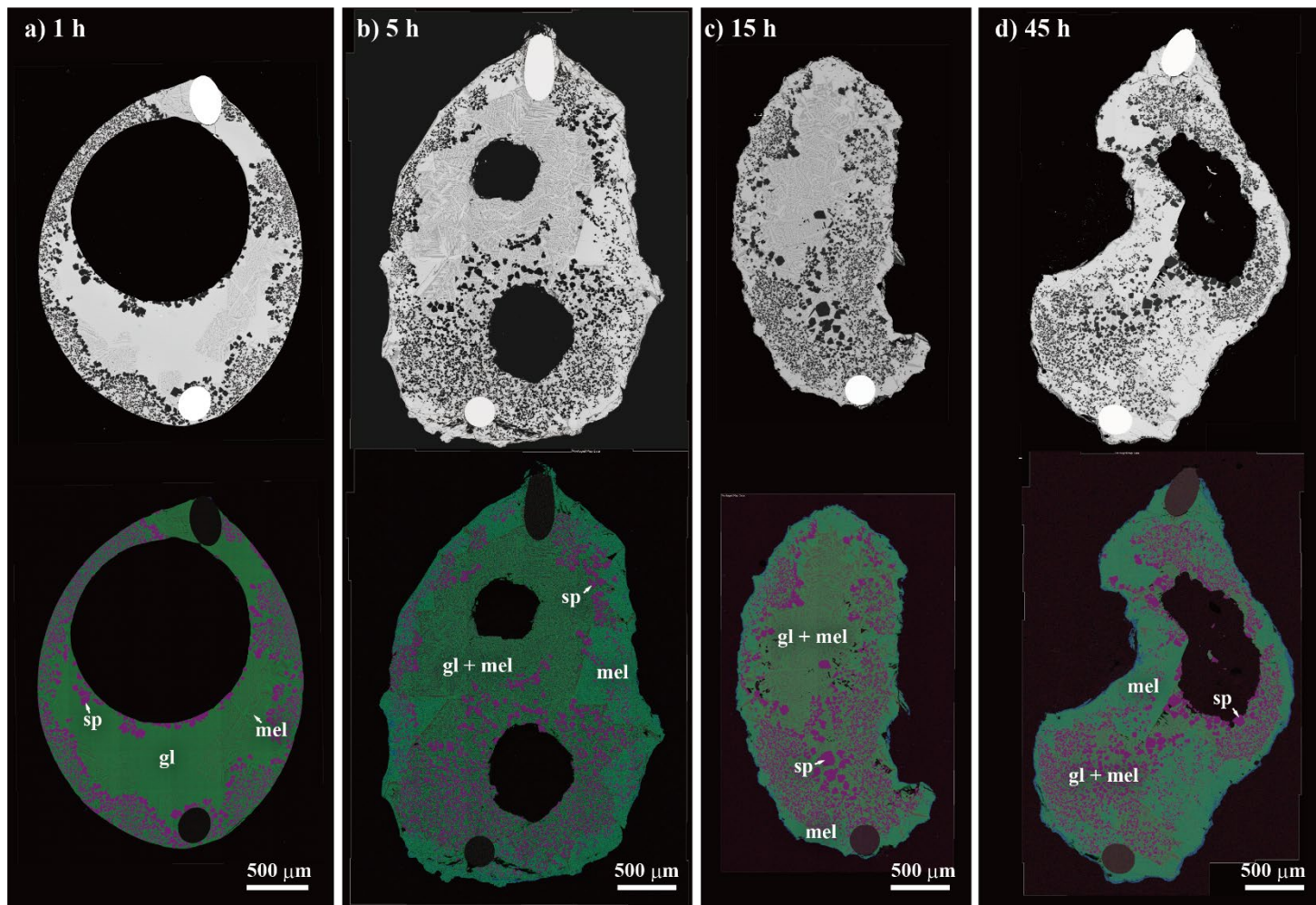
Fig. 3.21. BSE images and combined X-ray elemental maps with Mg (red), Ca (green), and Al (blue) of samples isothermally heated at 1420°C and $P_{H2} = 10^{-5}$ bar for 1–45 h with CAIχ initial composition. (a) 1 h (UT-12). (b) 5 h (UT-43). (c) 15 h (UT-35). (d) 45 h (UT-41).
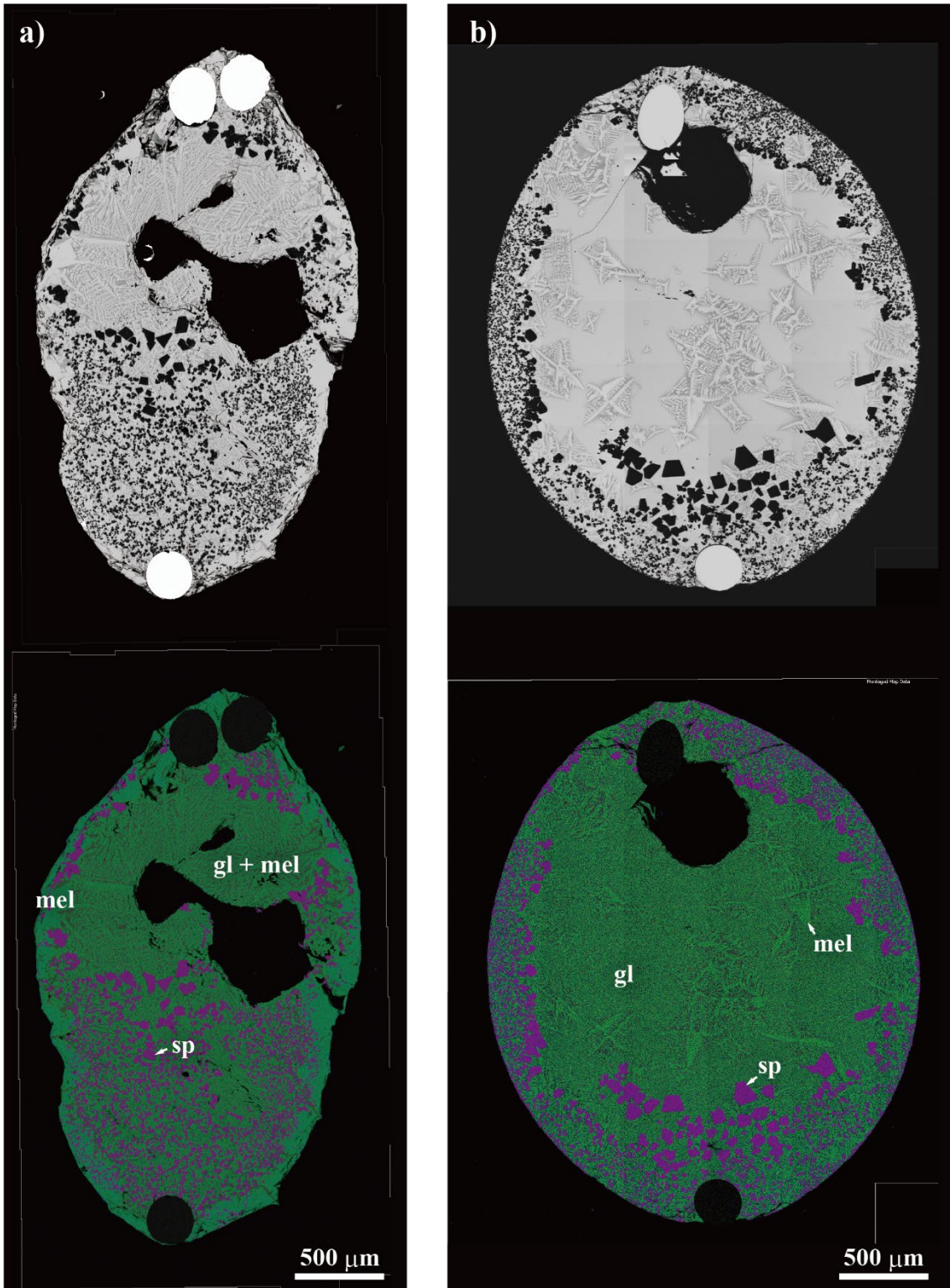
Fig. 3.22. BSE images and combined X-ray elemental maps with Mg (red), Ca (green), and Al (blue) of samples isothermally heated for 1 h at 1420°C and $P_{H2} = 10^{-4}$ bar. (a) CAIχ initial composition (UT-33). (b) CAIδ initial composition (UT-100).

Short-duration isothermal experiments for CAIδ composition were also conducted to investigate chemical compositional distribution within the melt due to the evaporation at the melt surface. All the samples consist of spinel, glass and a small amount of dendritic melilite. As mentioned above, dendritic melilite would have formed during quenching. Figure 3.23 shows the spatial distributions of Mg concentration in the glass plotted against the distance from the surface in the samples heated at 1420°C and $P_{H2} = 10^{-4}$ bar for 30 min. The figure shows that the Mg concentration of the glass gradually decreases from ~10.5 to ~8 wt. % within ~0.6 mm of the sample margin toward the sample surface, and remains almost constant inside that distance. The constant values of Mg concentration at the inner part of the samples (~10.5 wt. %) is close to the Mg concentration of glass in the homogenous starting material (~ 10.9 $\pm$ 0.25 wt. %), suggesting that such depletion of Mg attributed to the evaporation from the melt is limited to the outer part of the samples.
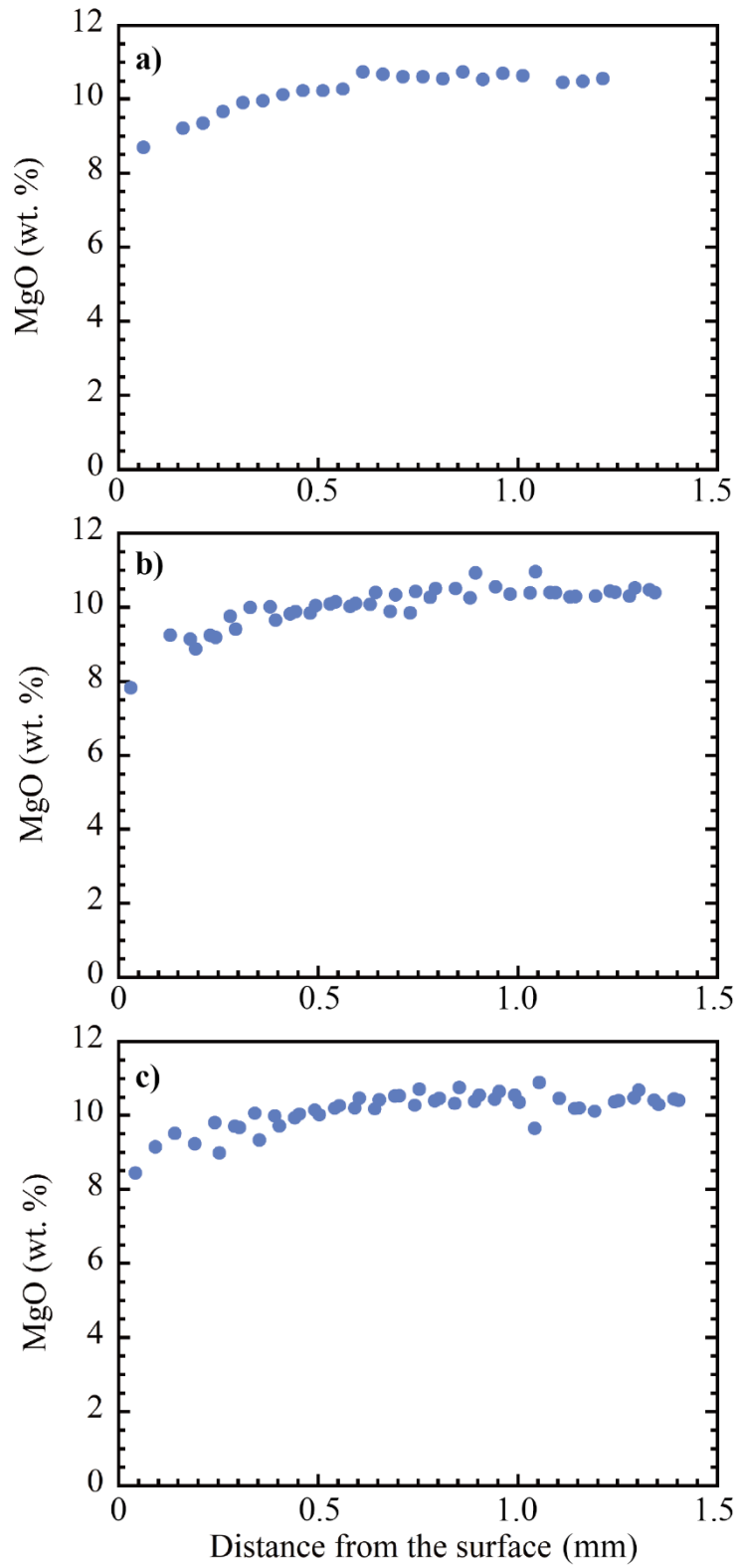
Fig. 3.23. Mg concentration profiles of glass in samples heated at 1420°C and $P_{H2} = 10^{-4}$ bar for 30 min as a function of distance from the surface of the sphere. (a) UT-104. (b),(c)UT-135.

4. Discussion

*4.1. Mechanism of melilite rim formation*

Continuous crystallization of Al-rich melilite at the surface of the samples was observed at $P_{H2} = 10^{-4}$ bar at all cooling rates studied in this work and $P_{H2} = 10^{-5}$ bar at the slowest cooling rate (5°C h^{-1}) for both starting compositions (Figs. 4.1, 4.2). These melilite grains were found to start crystallizing during 1 h-heating at the maximum temperature ($P_{H2} = 10^{-4}$ bar with CAIχ composition) or during the cooling followed by 1 h-heating at the maximum temperature ($P_{H2} = 10^{-5}$ bar with CAIχ and $P_{H2} = 10^{-4}$, 10^{-5} bar with CAIδ) (Figs. 3.21, 3.22; Tables 2.2, 2.3). The elemental map of åkermanite contents in melilite located at the outer margin of the samples heated at $P_{H2} = 10^{-4}$ bar (Figs. 3.11.e, f) clearly indicates that melilite crystallization proceeds from the sample surface toward the inside. Figure 4.3 shows crystallization temperature of melilite as a function of bulk chemical composition of CAI melt as suggested by Mendybaev et al. (2006). Melilite crystallization temperature and its chemical composition largely depend on the melt composition, and Al-rich melilite would crystallize from Mg and Si-poor melt at higher temperatures compared to Al-poor melilite. Melilite with åkermanite contents less than 21 mol% and 44 mol%, which are not expected to crystallize from the melt with CAIχ and CAIδ compositions, respectively, without chemical compositional change of melt (Fig. 4.3), indeed crystallized at the outer part of the samples with melilite mantle. Therefore, the onset of crystallization of Al-rich melilite at the melt surface is attributed to the local depletion of Mg and Si near the surface due to melt evaporation. This can explain the fact that crystallization of melilite took place, with more Al-rich composition that is not expected to crystallize from CAIχ and CAIδ melt compositions. Figure 4.3 also shows that the peak heating temperature should be ~1400°C to form Al-rich melilite mantle as a result of evaporation of Mg and Si from the melts.
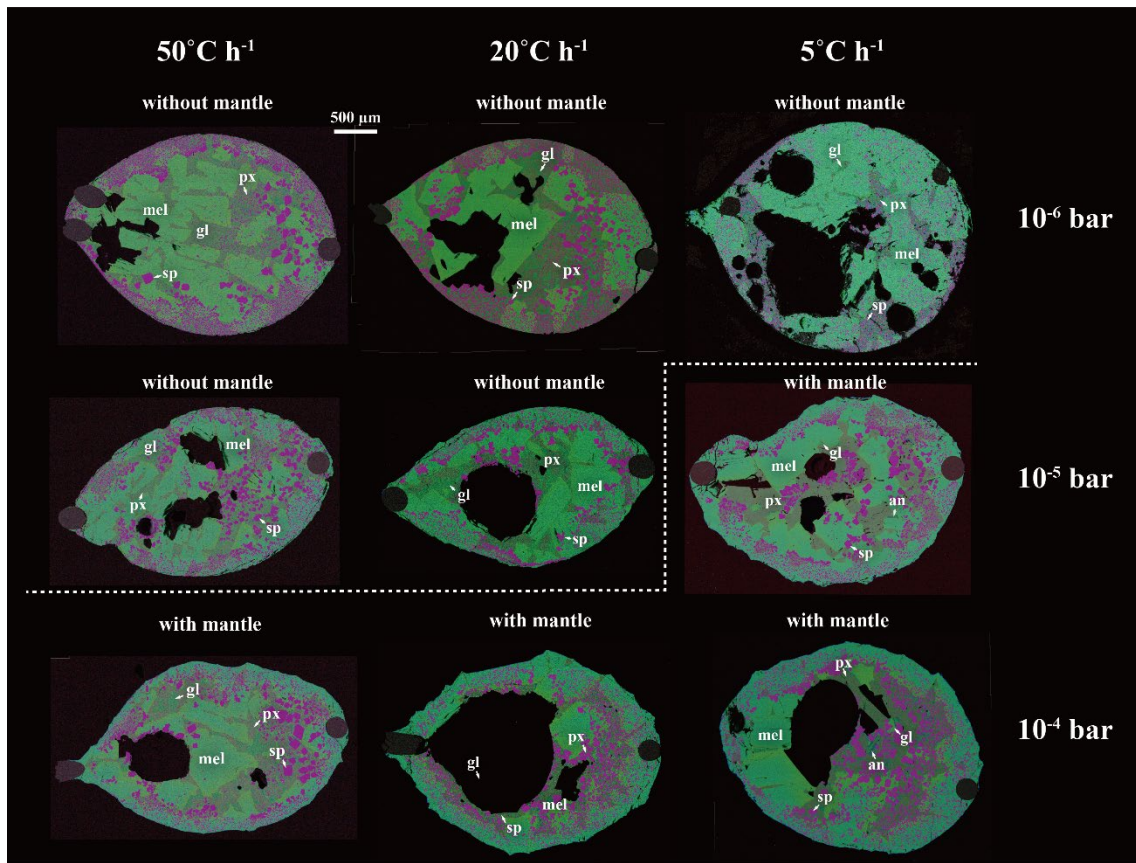
Fig. 4.1. Summary of combination of hydrogen pressure and cooling rates to form type B1 CAI-like texture with melilite mantle and type B2 CAI-like texture without melilite mantle for the CAIχ initial composition.
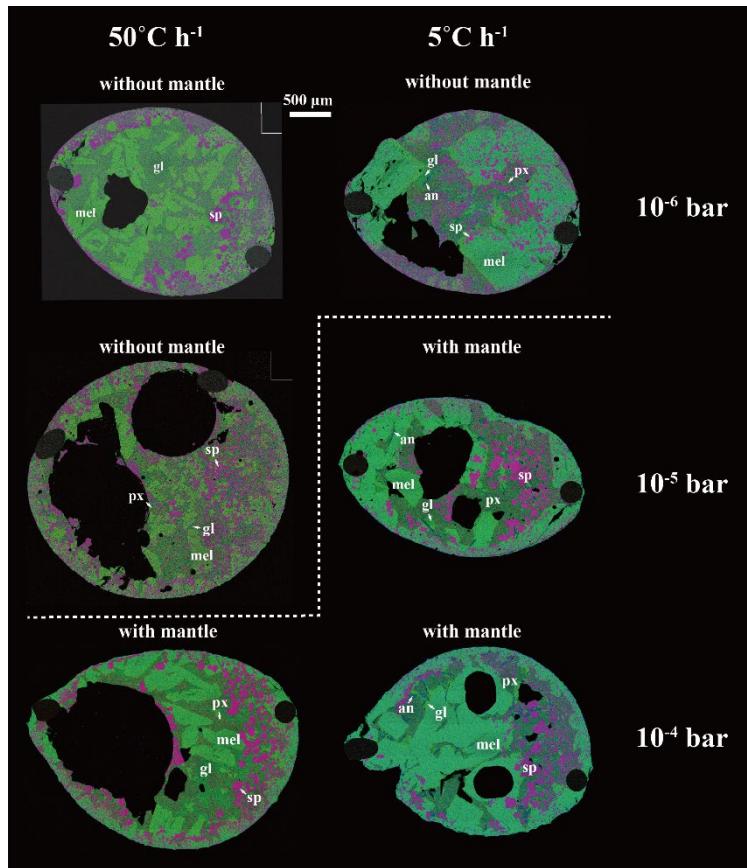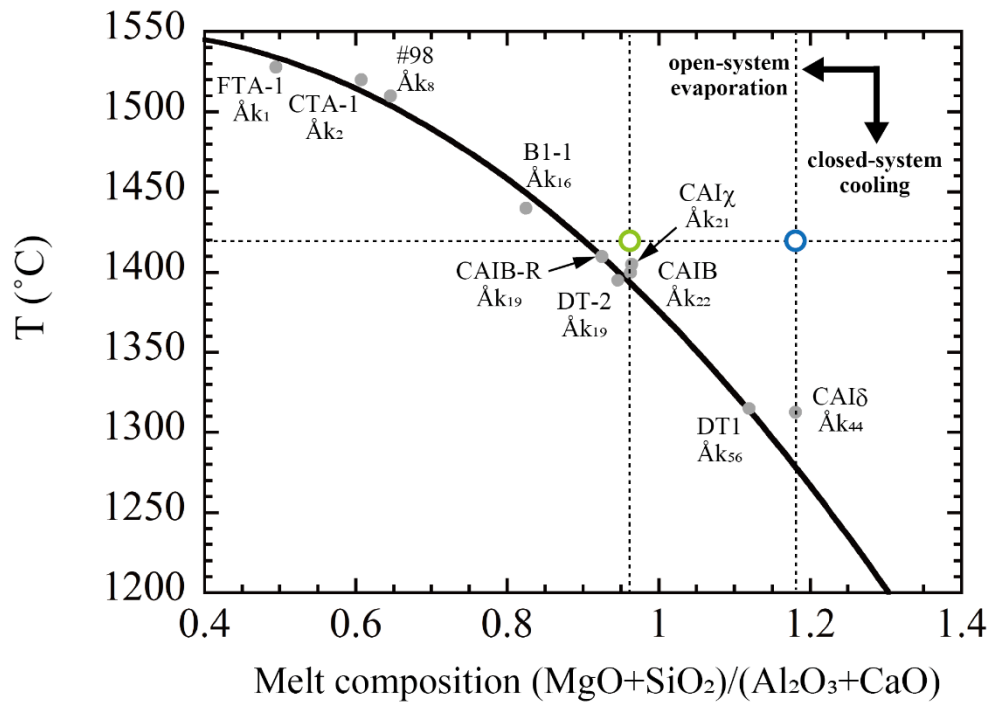
Fig. 4.2. Summary of combination of hydrogen pressure and cooling rates to form type B1 CAI-like texture with melilite mantle and type B2 CAI-like texture without melilite mantle for the CAIδ initial composition.

Fig. 4.3. Crystallization temperature of melilite as a function of melt composition. The experimental data obtained in this study and those from previous studies are plotted as gray dots with corresponding åkermanite contents of first-crystallizing melilite from the melt. Data sources: CAIB-R, DT1, and DT2, Mendybaev et al. (2006); CAIB, Stolper (1982); #98, Paque and Stolper (1984); FTA-1, CTA-1, and B1-1, Beckett (1986). The solid curve is a best fit through the experimental data ($y = 1527.6 + 174.15x – 326.21x^2$). Open circles show the initial composition of CAIχ (light green) and CAIδ (blue) melt at 1420°C. Arrows parallel and perpendicular to the x axis are possible trajectories of melt chemical composition during isothermal heating with melt evaporation (i.e., at low-pressure hydrogen) and cooling without melt evaporation (i.e., in air), respectively. Crystallization of melilite takes place when the chemical composition of the melt crosses the solid curve from right to left. Modified after Mendybaev et al. (2006).

Compositional distribution of elements in the spherical melt is controlled by the relative rates of evaporation process of Mg and Si from the surface and of elemental diffusion process (Richter et al., 2002; Mendybaev et al., 2006). Diffusion equation in a sphere is written by:

$$\frac{\partial C}{\partial t} = D\left(\frac{\partial^2 C}{\partial r^2} + \frac{2}{r}\frac{\partial C}{\partial r}\right)$$ (Eq. 4.1)

where C is the concentration of a component in the melt as a function of time t, r is the distance from the center of the sphere, and D is the diffusion coefficient of a component. The solution for diffusion equation with surface evaporation is expressed as (Crank, 1975; Hashimoto, 1986; Yamamoto et al., 2021):

$$\frac{C}{C_i} = \frac{2La}{r}\sum_{n=1}^{\infty}\frac{\exp\left(D\beta_n^2 t / a^2\right)}{\left\{\beta_n^2 + L(L-1)\right\}}\frac{\sin\beta_n^2 r / a}{\sin\beta_n}$$ (Eq. 4.2)

where the β_ns are the roots of

$$\beta_n\cot\beta_n + L - 1 = 0$$ (Eq. 4.3)

and

$$L = a\alpha / D$$ (Eq. 4.4)

C_i is the initial concentration of a specific component, a is the radius of the sphere, and α is the evaporation rate. L is a non-dimensional parameter representing the relative importance of evaporation and diffusion (Eq. 4.4). $L \ll 1$ corresponds to an evaporation dominated regime where the diffusion is significantly faster than the evaporation from the surface, which results in homogenous composition melt. On the other hand, $L \gg 1$ corresponds to a diffusion dominated regime where the evaporation from the surface is

77

significantly faster than the diffusion (e.g., Tsuchiyama et al., 1999; Richter, 2005). Such transition condition can be translated into the hydrogen pressure, because evaporation rates of Mg and Si from the melt under hydrogen-dominant environment are proportional to the square root of P_{H2} (Richter et al., 2002; Mendybaev et al., 2006), while diffusion rate has no P_{H2} dependence. Therefore, at lower P_{H2}, elemental diffusion is faster than evaporation, and no chemical zoning in the melt is expected. As a consequence, melilite crystallization occurs randomly throughout the chemically-homogeneous melt during cooling (Fig.4.4). On the other hand, at higher P_{H2}, evaporation rate could occur sufficiently faster than diffusive homogenization in the melt, resulting in compositional gradient inside the melt and the preferential crystallization of Al-rich melilite near the surface of the melt that is enriched in Ca and Al (Fig. 4.4). Such preferential crystallization of melilite at the surface relative to the interior was clearly observed in isothermal experiments lasting over 1 h at P_{H2} of 10^{-4} and 10^{-5} bar for CAIχ melt (Figs. 3.20, 3.21; Table 2.2).

$P_{H2} \leqq 10^{-5}$ bar
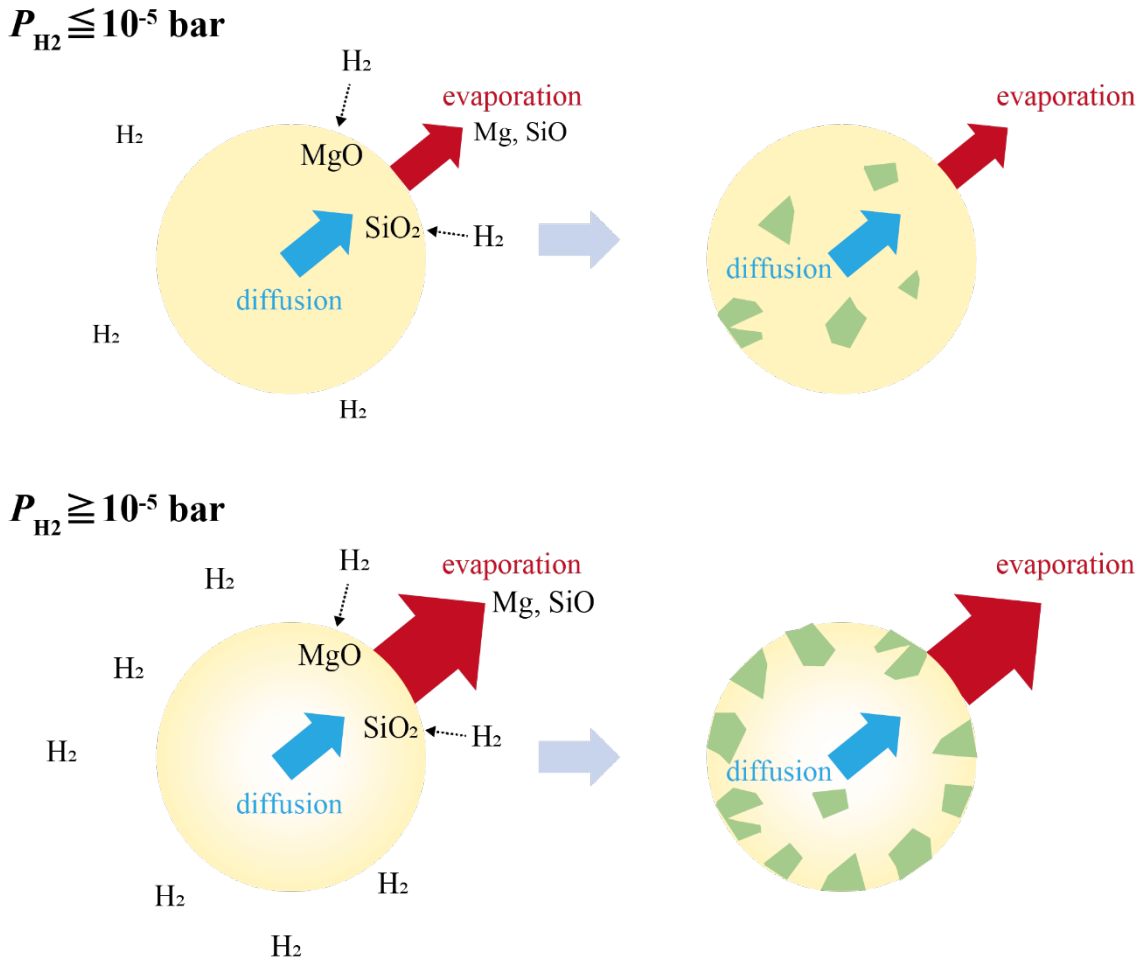
$P_{H2} \geqq 10^{-5}$ bar

Fig. 4.4. Schematic scenario of the formation of the melilite mantle. At lower P_{H2} ($\leq 10^{-5}$ bar), elemental diffusion is faster than evaporation and melilite crystallization takes place randomly throughout the chemically-homogeneous melt. On the other hand, at higher P_{H2} ($\geq 10^{-5}$ bar), evaporation could occur sufficiently faster than diffusive homogenization in the melt, resulting in the preferential crystallization of melilite near the surface of the melt that is enriched in Ca and Al.

The compositional gradient present in the short-duration isothermal experiments (Fig. 3.23) is the direct evidence of the sufficiently faster evaporation process from the surface compared to the diffusion process. The Mg concentration profiles in the short-duration isothermal experiments (Fig. 3.23) were well fitted with Eq. 4.2, from where D and α were obtained. Note that the value of C_i in each profile

was also obtained by the fitting because the constant Mg concentration in the inner part of the samples is slightly different in each experiment and this difference would reflect the glass composition in the starting material used in the experiments. The weighted averages of D and α are $(3.38 \pm 0.32) \times 10^{-7}$ cm^2 s^{-1} and $(2.73 \pm 0.11) \times 10^{-6}$ cm s^{-1}, respectively. The obtained D is within the range of values in previous studies (2.0–18×10^{-7} cm^2 s^{-1} at 1420°C; Sheng et al., 1994; Mendybaev et al., 2006) for CAI analog melts. The evaporation rate α can be converted to the evaporation flux J (mol cm^{-2} s^{-1}) of Mg by dividing α by a molar volume of MgO in the melt calculated using the melt density (Lange and Carmichael, 1987) and the initial composition of melt. The obtained J was 2.10×10^{-8} mol cm^{-2} s^{-1} and is roughly consistent with the values estimated from the weight losses of the samples (2.82×10^{-8} and 2.78×10^{-8} mol cm^{-2} s^{-1} for UT-104 and UT-135, respectively). The obtained L (Eq. 4.4) is ~1, which does not satisfy either diffusion- and evaporation-dominated regimes, and evaporation from the surface and elemental diffusion in melt are competing against each other. The value of the L might be to some extent sensible to the temperature, because the activation energy of evaporation from CAI analog melt has not been empirically determined. Nevertheless, the main determinant of the parameter L can be considered as the hydrogen pressure because the thermodynamically inferred activation energy for evaporation (~300 kJ mol^{-1}) is not significantly different from that for diffusion in the melt (~225 kJ mol^{-1}) (Liang and Davis, 2002). Evaporation rates from the CAIχ and CAIδ composition melts are expected to be comparable considering the comparable amount of evaporative weight loss of the samples without melilite mantle heated under the same heating condition (Fig. 3.14). Moreover, crystallization of melilite from the surface occurred at $P_{H2} \geq 10^{-5}$ bar for both compositions, suggesting that L would not change significantly. Although CAIχ and CAIδ have different liquidus temperatures of melilite and are predicted to condense at different temperatures (Grossman et al., 2002), similar values of L for both compositions suggest that open-system crystallization of CAI melts occurred under the

condition of $L \sim 1$ in the early Solar System and that igneous textures of type B CAIs formed through competition of evaporation of Mg and Si and elemental diffusion within the melts.
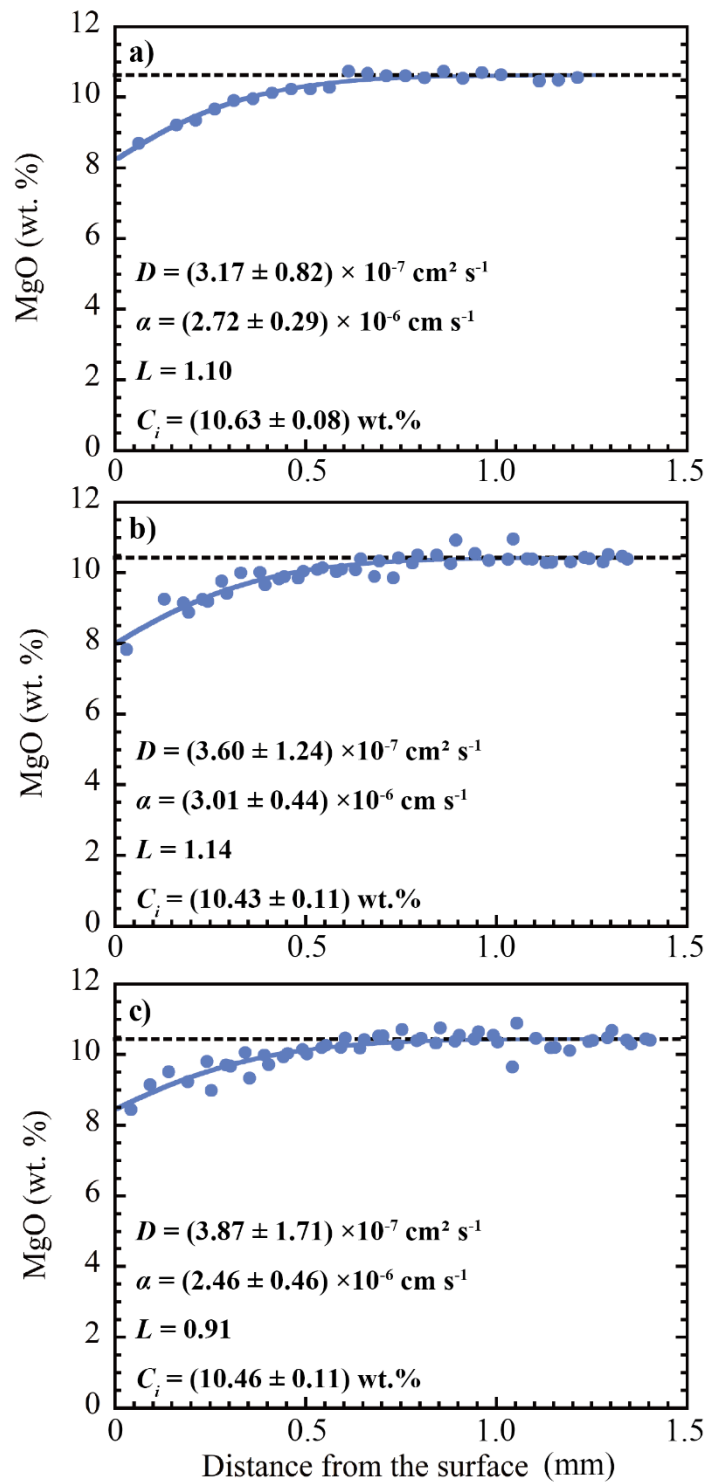
Fig.4.5. Best-fitted curves of observed Mg concentration profiles of glass shown in Fig. 3.22 by Eq. 4.2. Dotted lines represent estimated values of C_i. Errors are 2SE.

The distribution of chemical composition of melilite and weight losses of the samples reflect the presence or absence of melilite mantle at the sample surface. Once continuous melilite mantle on the spherical melt surface takes place, interior melt was sealed off from contacting with the surrounding gas. Therefore, the formation of continuous melilite mantle at the sample surface prevents further evaporation of the melt. In experiments with CAIχ composition at $P_{H2} = 10^{-4}$ bar, the evaporative weight losses of the samples increased by only a factor of two with an increase in the cooling timescale by one order of magnitude. (Fig. 3.14). In addition, melilite crystallized at this hydrogen pressure has a similar wide range of chemical composition, independent of the cooling rate (Fig. 3.12). These observations are consistent with the closed system crystallization of most melilite crystals in the melt interior after the formation of the melilite mantle (Fig. 4.4). On the other hand, in the case of samples without melilite mantle, evaporation of Mg and Si from the melt is not prevented, and evaporative weight losses and chemical composition of melilite simply reflects the difference in evaporation rates and cooling timescale. The larger weight loss at $P_{H2} = 10^{-5}$ bar and a cooling rate of 50°C h^{-1} than that at $P_{H2} = 10^{-6}$ bar (Fig. 3.14) are attributed to the difference in evaporation rates at different P_{H2}. At $P_{H2} = 10^{-6}$ bar, melilite crystallized at the cooling rate of 5°C h^{-1} is more gehlenite-rich compared with that at the cooling rate of 50°C h^{-1} (Fig. 3.12).

In experiments with CAIδ composition, the increase of evaporative weight loss of the samples associated with increasing P_{H2} and decreasing cooling timescale was observed regardless of the presence or absence of melilite mantle. This is because the crystallization temperature of CAIδ melt (1312.5 ± 2.5°C) is much lower than that of CAIχ melt (1402.5 ± 2.5°C) (Tables 2.2, 2.3), and the effect of evaporation at high temperatures before the formation of melilite mantle is significantly reflected in the amount of weight losses of the samples (Fig. 3.14). This can explain the observations that melilite exhibited more Åk-poor compositions at higher P_{H2} and slower cooling rate

(Fig. 3.13) under all P_{H2}-cooling rate conditions in the present experiments and melilite with the åkermanite content considerably lower than Åk~44 (Fig. 3.13) crystallized at high P_{H2} and slow cooling rate. It should be noted that the difference in weight losses at $P_{H2} = 10^{-5}$, 10^{-4} bar from that predicted by the difference in P_{H2} and cooling timescale would be due to the effect of melilite crystallization at the melt surface.

4.2. Mg isotopic composition in dynamic crystallization experiments

The isotopic composition profiles observed in samples at $P_{H2} = 10^{-5}$ and 10^{-4} bar show the increase in $\delta^{25}Mg$ toward the surface of the samples (Figs. 3.17–3.20), These $\delta^{25}Mg$ profiles are the results of preferential evaporation of lighter isotope (^{24}Mg) from the melt surface and accompanying isotope diffusion within the melt. This feature is consistent with Mg-depleted surface of glass in samples heated for short durations (Fig. 4.5). A large degree of Mg fractionation is seen in Al-rich melilite located at the surface of the samples, accounting for the preferential crystallization from the melt depleted in Mg and Si due to surface volatilization. Lack of such elevation in Mg composition at the surface at $P_{H2} = 10^{-6}$ bar suggests that isotopic diffusion within the melt is fast relative to evaporation and homogenize the Mg isotopic composition within the melt (Figs. 3.15, 3.16). This is indicative of crystallization from spatially homogenous melt. Progressive increase of Mg isotopic composition in the inner part of the samples was observed in the sample cooled at the rate of 5°C h^{-1} and $P_{H2} = 10^{-6}$ and 10^{-5} bar (Figs. 3.16, 3.18). This is because progressive evaporation of Mg and Si from the melt surface and diffusive isotope homogenization within the melt occurred during crystallization. Lack of such increase during crystallization in 50°C h^{-1} is explained by the lower degree of evaporation due to shorter cooling duration than the experiments cooled at 5°C h^{-1}.

Magnesium isotopic compositions of the experimental samples are somewhat different from the isotopic characteristic of natural CAIs. Although the increase in Mg isotope fractionation at the margin of the inclusion is observed in a natural type B1 CAI (Goswami, 1994) and a type A CAI (Shahar and Young, 2007), which is also considered to be formed as a result of evaporation, many of the CAIs show lighter isotopic compositions at the margin or homogeneous isotopic composition throughout the inclusion (e.g., Bullock et al., 2013). However, enrichment of heavier isotopes of Si and crystallization of anomalously Al-rich melilite at the surface of the CAIs indicate that

surface volatilization took place in the formation process of these CAIs (Bullock et al., 2013; Knight et al., 2009). Such discrepancy was discussed in previous studies, and possibility of modification of Mg isotopic composition near the rim of the inclusions due to subsolidus reheating events of CAI and isotopic exchange with an external isotopically normal reservoir was suggested to reverse the isotopic trend near the CAI margins (Bullock et al., 2013; Kita et al., 2012; Knight et al., 2009; Richter et al, 2007).

4.3. Formation conditions of Type B CAIs indicated from petrological and chemical characteristics

It is demonstrated from a series of experiments that type B1 CAI-like well-developed continuous melilite mantle can be reproduced under protosolar disk-like low hydrogen pressure conditions. The transition P_{H2} between conditions that formed type B1-like or type B2-like textures was found to be on the order of $P_{H2} = 10^{-5}$ bar irrespective of initial composition, although it also slightly depends on the cooling rate (Figs. 4.1, 4.2). This boundary P_{H2} conditions of 10^{-5} bar that formed type B1-like or Type B2-like texture is consistent with that predicted by Mendybaev et al. (2006).

The gradual increase in åkermanite contents from the CAI rim to the interior, which is indicative of inward growth of melilite from the CAI surface, is also observed in natural type B1 CAIs (e.g., MacPherson and Grossman, 1981; Simon and Grossman, 2006; Kawasaki et al., 2018). Simon and Grossman (2006) showed that the most Al-rich melilite ($Åk_{\sim 10}$) was found in the outermost part of the melilite mantle in type B1 CAIs, and such compositional characteristic was also observed in the experiments in this study.

Melilite in natural type B2 CAIs is more åkermanitic than that in natural type B1 CAIs, which is also consistent with the characteristics of melilite in samples without melilite mantle formed at lower P_{H2}. Simon and Grossman (2006) argued that the presence or absence of melilite mantle in type B1 and B2 CAIs would likely be attributed to the difference in their bulk chemical compositions, not the difference in evaporation history of these CAIs. However, our experimental results clearly indicate that textural and compositional difference in type B1 and B2 melilite can also be reproduced by crystallization of the precursor melt with the same bulk chemical composition under different P_{H2} conditions.

It is noted that water vapor, which is the third most abundant gas species in the protosolar disk (e.g., Lodders,2003; Wood and Morfill, 1988; Wood and Hashimoto,

1993), would affect the estimated P_{H2} boundary because water vapor plays a role in suppressing evaporation of Mg and Si from the melt as shown in Eqs. 1.1a and 1.1b. Figure 4.6 shows the comparison of estimated P_{H2O} in the nebula and the equilibrium P_{H2O} calculated from Eq.1.1.a and 1.1.b when $P_{H2} = 10^{-4}$–10^{-6} bar. The redox state of Ti of fassaite in the natural type B CAIs revealed that type B CAIs would form under reducing conditions with the P_{H2}/P_{H2O} ratio close to that estimated from the Solar System abundance of elements ($H_2/H_2O \sim 10^3$) if fassaite crystallized from the melt that is equilibrated with the surrounding disk gas (Beckett, 1986; Beckett et al., 1988; Grossman, 2008), and H_2/H_2O of 10^3 was used to calculate the nebular P_{H2O}.

The water vapor pressure P_{H2O} in the nebula increases with P_{H2}, while the equilibrium P_{H2O} increases linearly with a square root of P_{H2}. Thus, the difference between the disk P_{H2O} and the equilibrium P_{H2O} decreases with P_{H2}. Even in the case of P_{H2} of 10^{-4} bar, the equilibrium P_{H2O} is higher than the P_{H2O} in the solar nebula at temperatures higher than ~1250°C. Especially at ~1400°C, where melt fraction is high and effective evaporation and crystallization occur in the present study, the equilibrium P_{H2O} is 80–8 times higher than the nebular P_{H2O}. Therefore, the recondensation reaction is negligible under these conditions. For this reason, the experimentally predicted boundary of P_{H2} conditions does not significantly change when taking into account the effect of P_{H2O}.
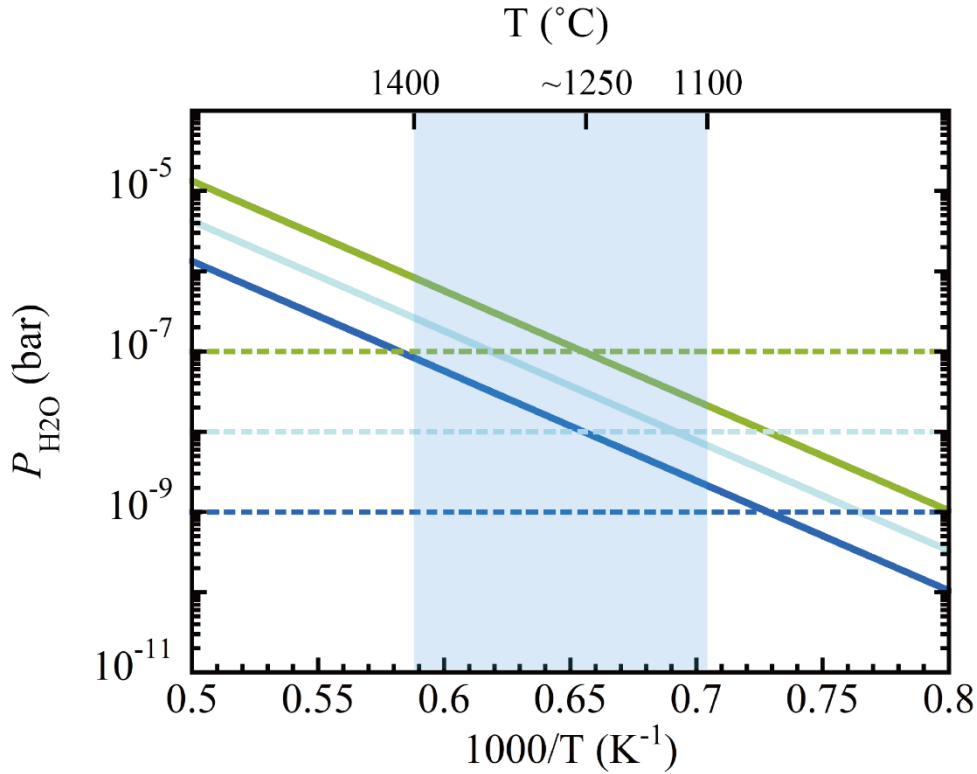
Fig. 4.6. Comparison of equilibrium vapor pressure P_{H2O} calculated from Eqs. 1.1.a and 1.1.b (solid lines) and P_{H2O} in the nebula calculated assuming $H_2/H_2O \sim 10^3$ (dotted lines). Each line corresponds to P_{H2O} when $P_{H2} = 10^{-4}$ (light green), 10^{-5} (light blue), 10^{-6} (dark blue). The hatched area shows the temperature range between the plausible peak temperature of CAI formation (1400°C) and solidus temperature of CAI (1100°C) (Stolper, 1981; Stolper and Paque, 1986). The equilibrium vapor pressure P_{H2O} was calculated assuming that initial composition is CAIχ, but almost identical for CAIδ.

The sample used in this study is ~2.5 mm in diameter, whereas the size of type B CAIs is typically on the orders of millimeter to centimeter in diameter (MacPherson and Grossman, 1981; Podosek et al., 1991; Simon and Grossman, 2006; Bullock et al., 2013; Kawasaki et al., 2018). Figure 4.7 shows the calculated Mg concentration profiles for 2.5 mm- and 1 cm-diameter heated at 1420°C and $P_{H2} = 10^{-4}$ bar for 30 min using D and α values derived in this study. The calculation result

indicates that the Mg-poor regions in the melt with both sizes are restricted to the outermost part of the melt droplet and the surface of the 1 cm-sized spherical melt would be depleted to the same degree as ~2.5 mm-sized smaller inclusion. Therefore, it can be concluded that the size of CAI melt does not significantly affect our experimentally-determined boundary of P_{H2} conditions that would form type B1-like or type B2-like textures when the size of the melt is within the size range of natural type B CAIs. The lack of statistical difference in size between type B1 and B2 CAIs also supports this prediction (MacPherson and Grossman, 1981; Podosek et al., 1991; Simon and Grossman, 2006; Bullock et al., 2013; Kawasaki et al., 2018).
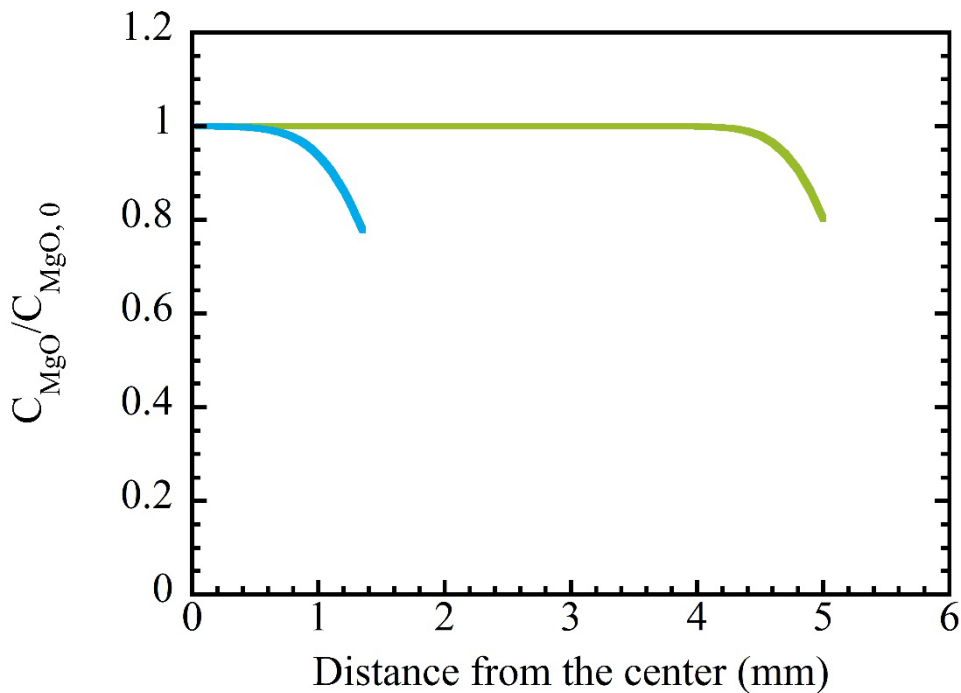
Fig. 4.7. Calculated spatial distribution of MgO concentration normalized to the initial concentration for spheres with ~2.5 mm (light blue) and 1 cm (light green) in diameter as a function of the distance from the spherical center. The surface is depleted in Mg to the same degree in both profiles.

4.4. Implication for the astrophysical setting of type B CAI formation

The result of the present study, combined with previous experimental works for crystallization of CAI melt (Stolper and Paque, 1986), suggests that the type B CAI formation required P_{H2} of 10^{-6}–10^{-4} bar at 1700–1400 K. A variety of CAI formation mechanisms proposed so far include heating in the inner disk region very close to the young sun, heating in a transient event within the Sun's protoplanetary disk such as shock wave heating, lightning, outburst from the young Sun (analogous to FU Orionis outburst) and so on (e.g., Scott and Krot, 2005 and references therein). The CAI constituent minerals condensed at the temperature of 1300–1700 K (Scott and Krot, 2014 and references therein), and such high temperature in protoplanetary disks lacks observational evidence except for disks around massive young stars (D'Alessio et al. 2005), but may have existed early in the Solar System history where viscous heating of the disk was effective.

Viscous evolution of disk is described by the equation:

$$\frac{\partial \Sigma}{\partial t} = \frac{3}{r}\frac{\partial}{\partial r}\left[r^{\frac{1}{2}}\frac{\partial}{\partial r}\left(\Sigma v r^{\frac{1}{2}}\right)\right]$$
(Eq. 4.1)

where v is the viscosity as given by $v = \alpha c_s h$ (α is a dimensionless parameter which expresses the efficiency of angular momentum transport due to turbulence ($0 < \alpha \le 1$), c_s is the local sound speed, and h is the scale height), r is the heliocentric distance, and Σ is the surface density of gas. The steady-state solution of Eq. 4.1 can be found as follows when assuming constant mass accretion rate $\dot{M} = -2\pi r \Sigma \upsilon_r$ (υ_r is the radial velocity of the gas) with time and location in the disk:

$$\Sigma = \frac{\dot{M}}{3\pi v} = \frac{\dot{M}}{3\pi}\frac{\Omega}{\alpha c_s^2}$$
(Eq. 4.2)

where Ω is the angular velocity. The sound speed c_s is the function of the mid-plane temperature T_m, and T_m can be solved analytically when piecewise power-law opacities

(analytic Rosseland mean opacities $\kappa = \kappa_n \rho^{a_n} T^{b_n}$) were assumed (Bell et al., 1997):

$$T_m^{5-b_n+(3a_n/2)} = \frac{3^{1-a_n}}{2^{7+a_n}} \frac{\kappa_n}{\sigma} \left(\frac{\mu}{R}\right)^{1+(3a_n/2)} \left(\frac{\dot{M}}{\pi}\right)^{2+a_n} \times \alpha^{-(1+a_n)} \left(\frac{GM_*}{r^3}\right)^{(3/2)+a_n} \qquad \text{(Eq. 4.3)}$$

where σ is the Stefan-Boltzmann constant, μ is the mean molecular weight, R is the gas constant, G is the gravitational constant, and M_* is stellar mass. The parameters used to calculate appropriate analytical opacities for different temperature ranges reflecting the change of dust properties are listed in Table 4.1. Max temperature in the list refers to sublimation temperature of the materials in different opacity regimes, above which the opacity is not included in the temperature estimate. The opacity regimes for n = 5, 8, and 9 were applied for the calculation of Tm in this study for simplicity because the calculated Tm in those selected opacity laws well reproduces the overall numerical calculation results in the temperature of interest at radial range of ~0.1–10 au (Bell et al., 1997). The opacities for n = 5, 8, and 9 are those of organic dust, silicate dust, and gaseous molecules, respectively (Table 4.1), but the choice of n = 5, 8, and 9 was only for the calculation of disk temperature structure and does not mean that disk materials consist only of organic dust, silicate dust, and gaseous molecules.

Σ is converted into the density at the disk midplane ρ_0 as:

$$\rho_0 = \frac{\Sigma}{\sqrt{2\pi}h}$$

T_m and P_{H2} as a function of heliocentric distance are shown in Fig.4.8.

Table4.1 Parameters for calculating analytical opacities (Bell et al., 1997).

n	κ_n	a_n	b_n	Max temperature (K)	Species
5	1×10^{-1}	0	0.7	580	Refractory organics
6	2×10^{15}	0	−5.2	680	Troilite
7	2×10^{-2}	0	0.8	960	Iron
8	2×10^{81}	1	−24	1570	Silicate
9	1×10^{-8}	2/3	3	3730	Molecule
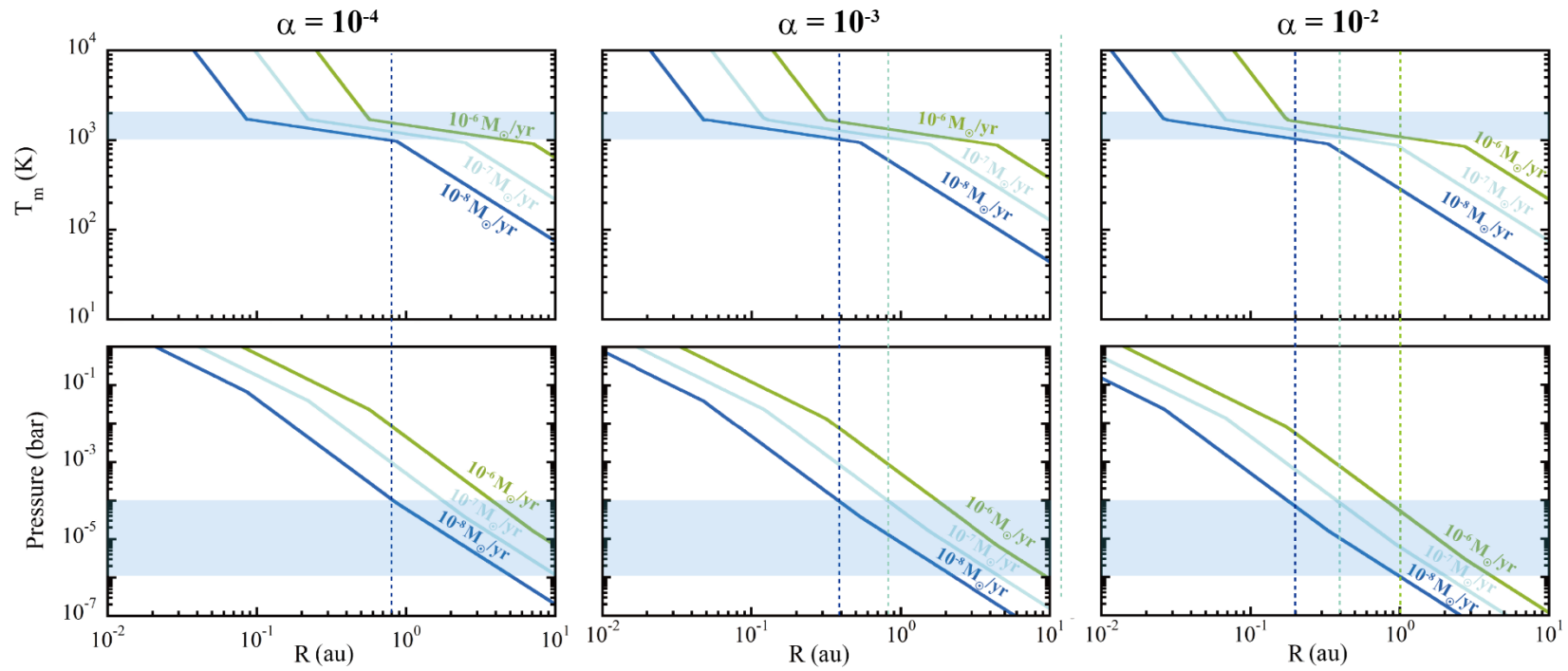
Fig. 4.8. Mid-plane temperatures and the hydrogen pressures according to the simple steady-state disk model for three different accretion rates $\dot{M}$ and angular momentum transport coefficients α (Bell et al., 1997). The hatched areas indicate the temperature-P_{H2} condition at which type B CAI precursor formed (~1000–2000K and $P_{H2} = 10^{-6}$–10^{-4} bar). Dotted lines with light green, light blue, and dark blue indicate possible location where temperature- P_{H2} conditions are both satisfied when $\dot{M}$ are 10^{-6}, 10^{-7}, and 10^{-8} $M_{\odot}$ yr^{-1}, respectively.

CAIs consist of refractory minerals enriched in Ca and Al and contain less magnesian silicates, such as forsterite and enstatite, and Fe-Ni metal. Their precursors may thus have existed in a high temperature region (>1300K) of protoplanetary disk. If type B CAIs were processed in such a high-temperature region (e.g., Yang and Ciesla 2012; Pignatale et al. 2018), along with the constraint of P_{H2} in this study, the locations that may satisfy the required T-P_{H2} condition ($T\sim1000$–2000 K, $P_{H2} = 10^{-6}$–10^{-4} bar) of CAIs exist in steady-state accretion disks within the heliocentric distances of 0.1–1 au (dotted lines in Fig. 4.6) (McKeegan et al., 2000; MacPherson et al., 2003; Bekaert et al., 2021). If type B CAIs were crystallized close to the young sun (~0.1 au), the disk with $\alpha = 0.01$ and the mass accretion rate of 10^{-8} $M_\odot$ yr^{-1} satisfies the CAI forming condition at 0.2 au. If this is the case, CAIs formed at the relatively late stage of disk evolution. On the other hand, if CAIs formed at ~1 au, the mass accretion rates of 10^{-6}–10^{-7} $M_\odot$ yr^{-1} is required at the early stage of disk evolution. A similar conclusion was obtained from the viscous spreading disk model by Birnstiel et al. (2010) and Yang and Ciesla (2012); the CAI forming condition at ~0.1 au could be satisfied in evolved disks (>1 Myr from the core collapse), while that at ~1 au in young disks (<1 Myr). In order to make further constraints on the disk property, the CAI forming location should be strictly constrained from meteoritic evidence such as the abundance of short-lived radionuclides (^{10}Be) and isotopic anomalies of metallic elements caused by irradiation of solar energetic particles.

Calculation results by Desch and Connolly (2002) have shown that required T-P_{H2} condition (peak temperature of ~1400°C, $P_{H2} = 10^{-6}$–10^{-4} bar) and cooling rate (0.1–50 K h^{-1}) for type B CAIs suggested from this work and previous studies (Stolper, 1981; Stolper and Paque, 1986; MacPherson et al., 1986; Kawasaki et al., 2018; Yamamoto et al., 2021) can be reproduced by shock wave heating for chondrule precursor materials in the solar nebula (Richter et al.,2006, Mendybaev et al., 2021). For instance, 0.5 mm-sized material (present at 2.5 au in a viscous disk with $\alpha = 10^{-4}$ and

$\dot{M} = 10^{-8}\,\mathrm{M_\odot\,yr^{-1}}$ where pre-shock temperature and pressure are 300 K and 10^{-5} bar, respectively, as shown in Fig. 4.6) would be heated and cooled from ~1450°C at a rate of ~40°C h^{-1} and pressure of 5×10^{-4} bar by a shock with its velocity of 7 km s^{-1} (Desch and Connolly, 2002). However, the shock wave model had been developed for understanding chondrule formation, and therefore more appropriate calculation for CAI may involve larger object and a preshock temperature closer to the condensation temperature of CAI precursor to further test the possibility that type B CAIs were formed by shock waves in the early Solar System. Other candidate models for CAI formation do not provide specific P-T history of the processes and cannot be tested to determine if these processes account for the formation of type B CAIs.

The difference in the formation condition of type B1 and B2 CAIs may be attributed to the regional variation of disk gas pressure. Regional variation of disk gas pressure associated with radial dependence of disk surface density would be present as shown in Fig. 4.6. Movement of CAI precursors along the vertical density structure of the disk (Aléon 2016) could also be responsible for the pressure variation discussed here. Alternatively, local fluctuation of the disk gas pressure may have been responsible for different P_{H2} conditions for the formation of type B1 and type B2 CAIs. The fluctuation of the inner edge of the protoplanetary disk has been suggested to explain oxygen isotope variation within minerals in type B CAIs (Itoh and Yurimoto 2003; Yurimoto et al. 2008; Kawasaki et al. 2018). In this case, the fluctuation of disk edge would also cause the local fluctuation of disk gas pressure. Different cooling rate at $P_{H2} = 10^{-5}$ bar would also be a possible cause for variation in type B CAIs. If this is the case, a variation of cooling rate at $P_{H2} = 10^{-5}$ bar would also put a constraint on their formation mechanism.

In any case, a hydrogen pressure of 10^{-5} bar with some fluctuation was needed for the formation of type B CAIs. The hydrogen pressure conditions during the formation of type B CAIs ($\geq 10^{-5}$ bar for type B1 and $\leq 10^{-5}$ bar for type B2 CAIs),

estimated from experiments under the protosolar disk-like low-pressure hydrogen in this study, would impose quantitative constraints on the astrophysical settings of the earliest epoch of the Solar System evolution.

5. Conclusions and future prospects

The pressure condition of the protosolar disk is a key parameter for understanding the evolution of the disk and the formation of planets. In this thesis, the hydrogen pressure (P_{H2}) during type B CAI formation from a series of evaporation and crystallization experiments in low-pressure hydrogen condition using material analogous to type B CAIs were constrained.

Experiments under low-pressure hydrogen conditions were conducted at systematically-varied P_{H2} (10^{-6}, 10^{-5}, and 10^{-4} bar) with the maximum temperature of 1420°C using a high-temperature vacuum furnace. Cooling rates of 50, 20, 5°C h^{-1}, which have been proposed to reproduce the igneous texture of CAIs, were adapted for the dynamic crystallization experiment. The present experiments suggest that evaporation during cooling of type B CAI melts played an important role in determining chemical, mineralogical, and petrologic characteristics of igneous CAIs. In particular, characteristic melilite mantle of type B1 CAIs can be formed at P_{H2} of 10^{-4} bar as a consequence of chemical compositional gradient in the melt produced by fast evaporation from the surface relative to elemental diffusion inside the melt. The mantle melilite presented Al-rich composition at the surface and became Mg-rich toward the inside, indicating the inward growth of the grains, which is also characteristic for type B1 CAIs. Chemical compositional gradient in the melt was in fact observed in the samples in short-duration isothermal experiments. The Mg isotopic compositions of samples with a well-developed melilite mantle can also be attributed to diffusion-limited evaporation of Mg and Si from the melt surface. Type B2 CAI-like texture was produced at P_{H2} of 10^{-6} bar, where elemental diffusion within the melt is fast enough to homogenize the melt composition and melilite crystalize randomly within the melt. At P_{H2} of 10^{-5} bar, the cooling rate of the melt

affects the texture, and type B1 (B2)-like texture forms at smaller (larger) cooling rates because of the difference in the amount of evaporation during cooling.

The present study therefore suggests that the transition P_{H2} for formation of type B1-like texture and type B2 texture is 10^{-5} bar irrespective of different starting compositions. Also, it was confirmed that the presence of gas species other than H_2 (especially H_2O) and the size of CAI melt does not significantly affect the experimentally-determined boundary of P_{H2} when the size of the melt is within the size range of natural type B CAIs.

This work puts a constraint on disk gas pressure (P_{H2} of 10^{-4}–10^{-6} bar) for formation of a millimeter- to centimeter-sized type B inclusion. If CAIs formed close to the Sun (~0.1 au), the disk with low mass accretion rate (~10^{-8} $M_{\odot}$ yr^{-1}) or the evolved disk (>1 Myr from the core collapse) would satisfy the CAI forming hydrogen pressure condition. On the other hand, if CAIs formed at ~1 au, the disk with higher mass accretion rate (~10^{-6}–10^{-7} $M_{\odot}$ yr^{-1}) or the young disk (<1 Myr from the core collapse) would satisfy the CAI forming hydrogen pressure condition. If CAIs formed close to the Sun (~0.1 au), the disk with low mass accretion rate (~10^{-8} $M_{\odot}$ yr^{-1}) or the evolved disk (>1 Myr from the core collapse) would satisfy the CAI forming hydrogen pressure condition. On the other hand, if CAIs formed at ~1 au, the disk with higher mass accretion rate (~10^{-6}–10^{-7} $M_{\odot}$ yr^{-1}) or the young disk (<1 Myr from the core collapse) would satisfy the CAI forming hydrogen pressure condition.

Finally, future prospects are described for further constraints on the protosolar disk and the CAI formation in the early Solar System.

The CAI forming location within the disk should surely be constrained from meteoritic evidence such as the abundance of short-lived radionuclides (^{10}Be) and isotopic anomalies of metallic elements caused by irradiation of solar energetic particles (McKeegan et al., 2000; MacPherson et al., 2003; Bekaert et al., 2021). Once the contribution of solar energetic particles for CAIs is quantitatively constrained, the

hydrogen pressure condition obtained in this study will put a strong constraint on the disk condition.

The evaporation and crystallization behavior investigated in this study is for evaporation in a complete open-system environment. The evaporation in (semi-)closed-system environment, where recondensation of evaporated gas is expected, has been proposed for chondrules (e.g., Nagahara and Ozawa, 2000; Alexander and Wang, 2001) because little or no isotopic fractionation of elements has been observed. Because of the presence of isotopic fractionations of Mg and Si within CAIs, the closed-system CAI formation has not been intensively studied. Herein, such experiments in a semi-closed system were not conducted due to experimental difficulty in quantitative control of recondensation; nevertheless, it is worth investigating in future work. Yamamoto et al. (2021) recently suggested that type B CAIs should have been heated for at least a few days above temperatures of the melilite liquidus to achieve the homogeneous oxygen isotopic composition of melilite in type B CAIs. Such elongated heating would result in significant chemical and isotopic fractionations that are inconsistent with natural type B CAIs. This discrepancy may also be relaxed if type B CAIs formed under conditions where significant recondensation occur. If type B CAIs formed under the semi-closed system conditions, the hydrogen pressure conditions in this study would be regarded as the lower limit.

.

Acknowledgements

References

Aléon, J. (2016). Oxygen isotopes in the early protoplanetary disk inferred from pyroxene in a classical type B CAI. Earth and Planetary Science Letters, 440, 62-70.

Alexander, C. O. D., & Wang, J. (2001). Iron isotopes in chondrules: Implications for the role of evaporation during chondrule formation. Meteoritics & Planetary Science, 36, 419-428.

Amelin, Y., Krot, A. N., Hutcheon, I. D., & Ulyanov, A. A. (2002). Lead isotopic ages of chondrules and calcium-aluminum-rich inclusions. Science, 297, 1678-1683.

Andrews, S. M. (2020). Observations of protoplanetary disk structures. Annual Review of Astronomy and Astrophysics, 58, 483-528.

Apai, D., Connolly Jr, H. C., & Lauretta, D. S. (2010). Thermal processing in protoplanetary nebulae. Protoplanetary Dust, 230-262.

Armitage, P. J., & Kley, W. (2019). From Protoplanetary Disks to Planet Formation. Springer-Verlag GmbH Germany.

Birnstiel, T., Dullemond, C. P., & Brauer, F. (2010). Gas-and dust evolution in protoplanetary disks. Astronomy & Astrophysics, 513, A79.

Beckett, J. R. (1986). The origin of calcium-, aluminum-rich inclusions from carbonaceous chondrites: An experimental study (Doctoral dissertation, The University of Chicago).

Bekaert, D. V., Auro, M., Shollenberger, Q. R., Liu, M. C., Marschall, H., Burton, K. W., Jacobsen, B., Brennecka, G. A., MacPherson, G. J., von Mutius, R., Sarafian, A., & Nielsen, S. G. (2021). Fossil records of early solar irradiation and cosmolocation of the CAI factory: A reappraisal. Science advances, 7, eabg8329.

Bell, K. R., Cassen, P. M., Klahr, H. H., & Henning, T. (1997). The structure and appearance of protostellar accretion disks: Limits on disk flaring. The Astrophysical Journal, 486, 372.

Bell, K. R., Cassen, P. M., Wasson, J. T., & Woolum, D. S. (2000). The FU orionis phenomenon and solar nebula material. Protostars and Planets IV. Mannings, AP Boss, SS Russell, 897-926.

Bergin, E. A., Cleeves, L. I., Gorti, U., Zhang, K., Blake, G. A., Green, J. D.,Andrews, S.M., Evans, N. J., Henning, T., Oberg, K., Pontoppidan, K., Qi, C., Salyk, C., & Van Dishoeck, E. F. (2013). An old disk still capable of forming a planetary system. Nature, 493, 644-646.

Berman R. G. (1983) A thermodynamic model for multicomponent melts, with application to the system $CaO-MgO-Al_2O_3-SiO_2$. Ph.D. thesis. University of British Columbia.

Boss, A. P. (1998). Temperatures in protoplanetary disks. Annual Review of Earth and Planetary Sciences, 26, 53-80.

Bullock, E. S., Knight, K. B., Richter, F. M., Kita, N. T., Ushikubo, T., MacPherson, G. J., Davis, A. M., & Mendybaev, R. A. (2013). Mg and Si isotopic fractionation patterns in types B1 and B2 CAI s: Implications for formation under different nebular conditions. Meteoritics & Planetary Science, 48, 1440-1458.

Ciesla, F. J. (2007). Outward transport of high-temperature materials around the midplane of the solar nebula. science, 318, 613-615.

Clayton, R. N., Hinton, R. W., & Davis, A. M. (1988). Isotopic variations in the rock-forming elements in meteorites. Philosophical Transactions of the Royal Society of London. Series A, Mathematical and Physical Sciences, 325, 483-501.

Connelly, J. N., Bizzarro, M., Krot, A. N., Nordlund, Å., Wielandt, D., & Ivanova, M. A. (2012). The absolute chronology and thermal processing of solids in the solar protoplanetary disk. Science, 338, 651-655.

Connolly Jr, H. C., & Burnett, D. S. (2003). On type B CAI formation: experimental constraints on fO2 variations in spinel minor element partitioning and reequilibration effects. Geochimica et Cosmochimica Acta, 67, 4429-4434.

Crank J. 1975. The Mathematics of Diffusion. 2nd edition Oxford: Oxford University Press.

D'Alessio, P., Calvet, N., & Woolum, D. S. (2005). Thermal structure of protoplanetary disks. In Chondrites and the Protoplanetary Disk (Vol. 341, p. 353).

Davis, A. M., Hashimoto, A., Clayton, R. N., & Mayeda, T. K. (1990). Isotope mass fractionation during evaporation of Mg 2 Si0 4. Nature, 347, 655-658.

Davis, A. M., & Richter, F. M. (2014). Condensation and evaporation of solar system materials. Meteorites and cosmochemical processes, 1, 335-360.

Desch, S. J., & Connolly Jr, H. (2002). A model of the thermal processing of particles in solar nebula shocks: Application to the cooling rates of chondrules. Meteoritics & Planetary Science, 37, 183-207.

Desch, S. J., Morris, M. A., Connolly Jr, H. C., & Boss, A. P. (2010). A critical examination of the X-wind model for chondrule and calcium-rich, aluminum-rich inclusion formation and radionuclide production. The Astrophysical Journal, 725, 692.

El Goresy, A., Armstrong, J. T., & Wasserburg, G. J. (1985). Anatomy of an Allende coarse-grained inclusion. Geochimica et Cosmochimica Acta, 49, 2433-2444.

Ebel, D. S., & Grossman, L. (2000). Condensation in dust-enriched systems. Geochimica et Cosmochimica Acta, 64, 339-366.

Grossman, L. (1972). Condensation in the primitive solar nebula. Geochimica et Cosmochimica Acta, 36, 597-619.

Grossman, L., Ebel, D. S., Simon, S. B., Davis, A. M., Richter, F. M., & Parsad, N. M. (2000). Major element chemical and isotopic compositions of refractory inclusions in C3 chondrites: The separate roles of condensation and evaporation. Geochimica et Cosmochimica Acta, 64, 2879-2894.

Grossman, L., Ebel, D. S., & Simon, S. B. (2002). Formation of refractory inclusions by evaporation of condensate precursors. Geochimica et Cosmochimica Acta, 66, 145-161.

Grossman L., Beckett J. R., Fedkin A. V., Simon S. B. and Ciesla F. J. (2008) Redox conditions in the Solar Nebula: observational, experimental, and theoretical constraints. In Reviews in Mineralogy and Geochemistry, vol. 68 (ed. G. J. MacPherson). Mineralogical Society of America, Washington, D.C., pp. 93–140.

Han, J., Keller, L. P., Liu, M. C., Needham, A. W., Hertwig, A. T., Messenger, S., & Simon, J. I. (2020). A coordinated microstructural and isotopic study of a Wark-Lovering rim on a Vigarano CAI. Geochimica et cosmochimica acta, 269, 639-660.

Haisch Jr, K. E., Lada, E. A., & Lada, C. J. (2001). Disk frequencies and lifetimes in young clusters. The Astrophysical Journal Letters, 553, L153.

Hashimoto, A. (1983). Evaporation metamorphism in the early solar nebula—evaporation experiments on the melt FeO-MgO-SiO_2-CaO-Al_2O_3 and chemical fractionations of primitive materials. Geochemical Journal, 17, 111-145.

Hashimoto, A. (1990). Evaporation kinetics of forsterite and implications for the early solar nebula. Nature, 347, 53-55.

Hirth, J. P., & Pound, G. M. (1963). Condensation and Evaporation. In Progr. in Mat. Sci. (Vol. 11, p. 15). Pergamon Press Oxford.

Henning, T., & Semenov, D. (2013). Chemistry in protoplanetary disks. Chemical Reviews, 113, 9016-9042.

Itoh, S., & Yurimoto, H. (2003). Contemporaneous formation of chondrules and refractory inclusions in the early Solar System. Nature, 423, 728-731.

Jones, R., Libourel, G., & Villeneuve, J. (2018). Thermal histories of chondrules: Petrologic observations and experimental constraints. In Chondrules and the protoplanetary disk (pp. 57-90). Cambridge University Press.

Kamibayashi, M., Tachibana, S., Yamamoto, D., Kawasaki, N., & Yurimoto, H. (2021). Effect of Hydrogen Gas Pressure on Calcium–Aluminum-rich Inclusion Formation in the Protosolar Disk: a Laboratory Simulation of Open-system Melt Crystallization. The Astrophysical Journal Letters, 923, L12.

Kawasaki, N., Simon, S. B., Grossman, L., Sakamoto, N., & Yurimoto, H. (2018). Crystal growth and disequilibrium distribution of oxygen isotopes in an igneous Ca-Al-rich inclusion from the Allende carbonaceous chondrite. Geochimica et Cosmochimica Acta, 221, 318-341.

Kawasaki, N., Park, C., Sakamoto, N., Park, S. Y., Kim, H. N., Kuroda, M., & Yurimoto, H. (2019). Variations in initial $^{26}Al/^{27}Al$ ratios among fluffy Type A Ca–Al-rich inclusions from reduced CV chondrites. Earth and Planetary Science Letters, 511, 25-35.

Kawasaki, N., Wada, S., Park, C., Sakamoto, N., & Yurimoto, H. (2020). Variations in initial 26Al/27Al ratios among fine-grained Ca-Al-rich inclusions from reduced CV chondrites. Geochimica et Cosmochimica Acta, 279, 1-15.

Kawasaki, N., Itoh, S., Sakamoto, N., Simon, S. B., Yamamoto, D., & Yurimoto, H. (2021). Oxygen and Al-Mg isotopic constraints on cooling rate and age of partial melting of an Allende Type B CAI, Golfball. Meteoritics & Planetary Science, 56, 1224-1239.

Kita, N. T., Huss, G. R., Tachibana, S., Amelin, Y., Nyquist, L. E., & Hutcheon, I. D. (2005). Constraints on the origin of chondrules and CAIs from short-lived and long-lived radionuclides (No. UCRL-BOOK-216767). Lawrence Livermore National Lab. (LLNL), Livermore, CA (United States).

Kita, N. T., Ushikubo, T., Knight, K. B., Mendybaev, R. A., Davis, A. M., Richter, F. M., & Fournelle, J. H. (2012). Internal $^{26}Al–^{26}Mg$ isotope systematics of a Type B CAI: remelting of refractory precursor solids. Geochimica et Cosmochimica Acta, 86, 37-51.

Knight, K. B., Kita, N. T., Davis, A. M., Richter, F. M., & Mendybaev, R. A. (2009, March). Mg and Si isotope fractionation within three Type b Ca-Al-rich inclusions. In Lunar and Planetary Science Conference (p. 2360).

Kuroda, D., & Hashimoto, A. (2002). The reaction of forsterite with hydrogen-its apparent and real temperature dependences. Antarctic meteorite research, 15, 152.

Lange, R. A., & Carmichael, I. S. (1987). Densities of $Na_2O-K_2O-CaO-MgO-FeO-Fe_2O_3-Al_2O_3-TiO_2-SiO_2$ liquids: new measurements and derived partial molar properties. Geochimica et Cosmochimica Acta, 51, 2931-2946.

Liang, Y., & Davis, A. M. (2002). Energetics of multicomponent diffusion in molten CaO-Al_2O_3-SiO_2. Geochimica et Cosmochimica Acta, 66, 635-646.

Lodders, K. (2003). Solar system abundances and condensation temperatures of the elements. The Astrophysical Journal, 591, 1220.

MacPherson, G. J., & Grossman, L. (1981). A once-molten, coarse-grained, Ca-rich inclusion in Allende. Earth and Planetary Science Letters, 52, 16-24.

MacPherson, G. J., Grossman, L., Allen, J. M., & Beckett, J. R. (1982). Origin of rims on coarse-grained inclusions in the Allende meteorite. In Lunar and Planetary Science Conference Proceedings (Vol. 12, pp. 1079-1091).

MacPherson, G. J., Huss, G. R., & Davis, A. M. (2003). Extinct 10Be in type A calcium-aluminum-rich inclusions from CV chondrites. Geochimica et Cosmochimica Acta, 67, 3165-3179.

MacPherson, G. J. (2014). Calcium-aluminum-rich inclusions in chondritic meteorites. Meteorites and cosmochemical processes, 1, 139-179.

McKeegan, K. D., Chaussidon, M., & Robert, F. (2000). Incorporation of short-lived 10Be in a calcium-aluminum-rich inclusion from the Allende meteorite. Science, 289, 1334-1337.

Mendybaev, R. A., Richter, F. M., & Davis, A. M. (2006). Crystallization of melilite from CMAS-liquids and the formation of the melilite mantle of Type B1 CAIs: Experimental simulations. Geochimica et Cosmochimica Acta, 70, 2622-2642.

Mendybaev, R. A., Kamibayashi, M., Teng, F. Z., Savage, P. S., Georg, R. B., Richter, F. M., & Tachibana, S. (2021). Experiments quantifying elemental and isotopic fractionations during evaporation of CAI-like melts in low-pressure hydrogen and in vacuum: Constraints on thermal processing of CAIs in the protoplanetary disk. Geochimica et Cosmochimica Acta, 292, 557-576.

Nagahara, H., & Ozawa, K. (1996). Evaporation of forsterite in H_2 gas. Geochimica et Cosmochimica Acta, 60, 1445-1459.

Nittler, L. R., & Ciesla, F. (2016). Astrophysics with extraterrestrial materials. Annual Review of Astronomy and Astrophysics, 54, 53-93.

Paque, J. M., Burnett, D. S., & Beckett, J. R. (2007). Zoning patterns of Fe and V in spinel from a type B Ca-Al-rich inclusion: Constraints on subsolidus thermal history. Meteoritics & Planetary Science, 42, 899-912.

Pascucci, I., & Tachibana, S. (2010). The clearing of protoplanetary disks and of the protosolar nebula. Protoplanetary Dust, 263.

Pignatale, F. C., Charnoz, S., Chaussidon, M., & Jacquet, E. (2018). Making the planetary material diversity during the early assembling of the solar system. The Astrophysical journal letters, 867, L23.

Podosek, F. A., Zinner, E. K., Macpherson, G. J., Lundberg, L. L., Brannon, J. C., & Fahey, A. J. (1991). Correlated study of initial $^{87}Sr^{86}Sr$ and Al-Mg isotopic systematics and petrologic properties in a suite of refractory inclusions from the Allende meteorite. Geochimica et Cosmochimica Acta, 55, 1083-1110.

Richter, F. M., Davis, A. M., Ebel, D. S., & Hashimoto, A. (2002). Elemental and isotopic fractionation of Type B calcium-, aluminum-rich inclusions: experiments, theoretical considerations, and constraints on their thermal evolution. Geochimica et Cosmochimica Acta, 66, 521-540.

Richter, F. M., Mendybaev, R. A., & Davis, A. M. (2006). Conditions in the protoplanetary disk as seen by the type B CAIs. Meteoritics & Planetary Science, 41, 83-93.

Richter, F. M., Janney, P. E., Mendybaev, R. A., Davis, A. M., & Wadhwa, M. (2007). Elemental and isotopic fractionation of Type B CAI-like liquids by evaporation. Geochimica et Cosmochimica Acta, 71, 5544-5564.

Richter, F. M., Kita, N. T., Mendybaev, R. A., Davis, A. M., & Valley, J. W. (2007, March). High-precision Mg isotopic composition of Type B1 and B2 CAI melilite. In Lunar and Planetary Science Conference (No. 1338, p. 2303).

Scott, E. R., & Krot, A. N. (2005). Chondritic meteorites and the high-temperature nebular origins of their components. In Chondrites and the protoplanetary disk (Vol. 341, p. 15).

Scott, E. R., & Krot, A. N. (2014). Chondrites and their components. Meteorites and cosmochemical processes, 1, 65-137.

Shahar, A., & Young, E. D. (2007). Astrophysics of CAI formation as revealed by silicon isotope LA-MC-ICPMS of an igneous CAI. Earth and Planetary Science Letters, 257, 497-510.

Shornikov, S. I., & Yakovlev, O. I. (2015). Study of complex molecular species in the gas phase over the $CaO–MgO–Al_2O_3–TiO_2–SiO_2$ system. Geochemistry International, 53, 690-699.

Shu, F. H., Shang, H., & Lee, T. (1996). Toward an astrophysical theory of chondrites. Science, 271, 1545-1552.

Shu, F. H., Shang, H., Gounelle, M., Glassgold, A. E., & Lee, T. (2001). The origin of chondrules and refractory inclusions in chondritic meteorites. The Astrophysical Journal, 548, 1029.

Simon, J. I., Young, E. D., Russell, S. S., Tonui, E. K., Dyl, K. A., & Manning, C. E. (2005). A short timescale for changing oxygen fugacity in the solar nebula revealed by high-resolution 26Al–26Mg dating of CAI rims. Earth and Planetary Science Letters, 238, 272-283.

Simon, S. B., & Grossman, L. (2006). A comparative study of melilite and fassaite in Types B1 and B2 refractory inclusions. Geochimica et Cosmochimica Acta, 70, 780-798.

Stolper, E. (1982). Crystallization sequences of Ca-Al-rich inclusions from Allende: An experimental study. Geochimica et Cosmochimica Acta, 46, 2159-2180.

Stolper, E., & Paque, J. M. (1986). Crystallization sequences of Ca-Al-rich inclusions from Allende: The effects of cooling rate and maximum temperature. Geochimica et Cosmochimica Acta, 50, 1785-1806.

Sugiura, N., Mizuno, T., Ushikubo, T., & Hiyagon, H. (2004). Si and Mg isotope fractionations in melilite in coarse-grained CAIs measured by SIMS. Geochemical Journal, 38, 405-415.

Sylvester, P. J., Grossman, L., & MacPherson, G. J. (1992). Refractory inclusions with unusual chemical compositions from the Vigarano carbonaceous chondrite. Geochimica et cosmochimica acta, 56, 1343-1363.

Sylvester, P. J., Simon, S. B., & Grossman, L. (1993). Refractory inclusions from the Leoville, Efremovka, and Vigarano C3V chondrites: Major element differences between Types A and B, and extraordinary refractory siderophile element compositions. Geochimica et cosmochimica acta, 57, 3763-3784.

Tachibana, S., & Tsuchiyama, A. (1998). Incongruent evaporation of troilite (FeS) in the primordial solar nebula: An experimental study. Geochimica et cosmochimica acta, 62, 2005-2022.

Tachibana, S., Tsuchiyama, A., & Nagahara, H. (2002). Experimental study of incongruent evaporation kinetics of enstatite in vacuum and in hydrogen gas. Geochimica et cosmochimica acta, 66, 713-728.

Tachibana, S., Nagahara, H., Ozawa, K., Ikeda, Y., Nomura, R., Tatsumi, K., & Joh, Y. (2011). Kinetic condensation and evaporation of metallic iron and implications for metallic iron dust formation. The Astrophysical Journal, 736, 16.

Takigawa, A., Tachibana, S., Nagahara, H., Ozawa, K., & Yokoyama, M. (2009). Anisotropic evaporation of forsterite and its implication for dust formation conditions in circumstellar environments. The Astrophysical Journal Letters, 707, L97.

Takigawa, A., Tachibana, S., Nagahara, H., & Ozawa, K. (2015). Evaporation and condensation kinetics of corundum: the origin of the 13 μm feature of oxygen-rich AGB stars. The Astrophysical Journal Supplement Series, 218, 2.

Tsuchiyama, A., Takahashi, T., & Tachibana, S. (1998). Evaporation rates of forsterite in the system Mg_2SiO_4–H_2. Mineralogical Journal, 20, 113-126.

Tsuchiyama, A., Tachibana, S., & Takahashi, T. (1999). Evaporation of forsterite in the primordial solar nebula; rates and accompanied isotopic fractionation. Geochimica et cosmochimica acta, 63, 2451-2466.

Wada, S., Kawasaki, N., Park, C., & Yurimoto, H. (2020). Melilite condensed from an 16O-poor gaseous reservoir: Evidence from a fine-grained Ca-Al-rich inclusion of Northwest Africa 8613. Geochimica et Cosmochimica Acta, 288, 161-175.

Wang, J., Davis, A. M., Clayton, R. N., Mayeda, T. K., & Hashimoto, A. (2001). Chemical and isotopic fractionation during the evaporation of the $FeO-MgO-SiO_2-CaO-Al_2O_3-TiO_2$ rare earth element melt system. Geochimica et Cosmochimica Acta, 65, 479-494.

Wark, D. A., & Lovering, J. F. (1982). The nature and origin of type B1 and B2 Ca- Al-rich inclusions in the Allende meteorite. Geochimica et Cosmochimica Acta, 46, 2581-2594.

Wood, J. A., & Hashimoto, A. (1993). Mineral equilibrium in fractionated nebular systems. Geochimica et Cosmochimica Acta, 57, 2377-2388.

Wood, J. A., & Morfill, G. E. (1988). A review of solar nebula models. Meteorites and the early solar system, 329-347.

Wyatt, M. C. (2008). Evolution of debris disks. Annu. Rev. Astron. Astrophys., 46, 339-383.

Yamada, M., Tachibana, S., Nagahara, H., & Ozawa, K. (2006). Anisotropy of Mg isotopic fractionation during evaporation and Mg self-diffusion of forsterite in vacuum. Planetary and Space Science, 54, 1096-1106.

Yamamoto, D., Kawasaki, N., Tachibana, S., Kamibayashi, M., & Yurimoto, H. (2021). An experimental study on oxygen isotope exchange reaction between CAI melt and low-pressure water vapor under simulated Solar nebular conditions. Geochimica et Cosmochimica Acta, 314, 108-120.

Yang, L., & Ciesla, F. J. (2012). The effects of disk building on the distributions of refractory materials in the solar nebula. Meteoritics & Planetary Science, 47, 99-119.

Yurimoto H., Krot A. N., Choi B., et al. 2008 in Oxygen in the Solar System, ed. G. J. MacPherson (Mineralogical Society of America, Washington DC), 141.